

Final report to the  
Office of Naval Research

on the

**Experimental Characterization of Nonlinear  
Viscoelastic and Adhesive Properties of Elastomers**

under the

**ONR Research Grant,**

**N00014-05-1-0400**

to

**The University of Texas at Austin**

**PI: K. Ravi-Chandar**  
**Program Officer: Dr. R.S. Barsoum, ONR 334**

**Center for Mechanics of Solids, Structures and Materials**  
**The University of Texas at Austin**  
**1 University Station, C0600**  
**Austin, TX 78712-0235**

**DISTRIBUTION STATEMENT A**  
**Approved for Public Release**  
**Distribution Unlimited**

**20060808095**

REPORT DOCUMENTATION PAGE				Form Approved OMB No. 0704-0188	
<p>The public reporting burden for this collection of information is estimated to average 1 hour per response, including the time for reviewing instructions, searching existing data sources, gathering and maintaining the data needed, and completing and reviewing the collection of information. Send comments regarding this burden estimate or any other aspect of this collection of information, including suggestions for reducing the burden, to Department of Defense, Washington Headquarters Services, Directorate for Information Operations and Reports (0704-0188), 1215 Jefferson Davis Highway, Suite 1204, Arlington, VA 22202-4302. Respondents should be aware that notwithstanding any other provision of law, no person shall be subject to any penalty for failing to comply with a collection of information if it does not display a currently valid OMB control number.</p> <p><b>PLEASE DO NOT RETURN YOUR FORM TO THE ABOVE ADDRESS.</b></p>					
1. REPORT DATE (DD-MM-YYYY) 27-07-2006		2. REPORT TYPE Final Report		3. DATES COVERED (From - To) 1-Mar-2005 to 31-Mar-2006	
4. TITLE AND SUBTITLE Experimental Characterization of Nonlinear Viscoelastic and Adhesive Properties of Elastomers				5a. CONTRACT NUMBER	
				5b. GRANT NUMBER N00014-1-0400	
				5c. PROGRAM ELEMENT NUMBER	
6. AUTHOR(S) K. Ravi-Chandar				5d. PROJECT NUMBER	
				5e. TASK NUMBER	
				5f. WORK UNIT NUMBER	
7. PERFORMING ORGANIZATION NAME(S) AND ADDRESS(ES) The University of Texas at Austin Office of Sponsored Projects, P.O.Box. 7726 Austin, TX 78713-7726				8. PERFORMING ORGANIZATION REPORT NUMBER	
9. SPONSORING/MONITORING AGENCY NAME(S) AND ADDRESS(ES) Office of Naval Research Program Officer: Dr. Roshdy G. Barsoum 875 North Randolph Street Arlington, VA 22203-3521				10. SPONSOR/MONITOR'S ACRONYM(S) ONR	
				11. SPONSOR/MONITOR'S REPORT NUMBER(S)	
12. DISTRIBUTION/AVAILABILITY STATEMENT Approved for Public Release; distribution is unlimited.					
13. SUPPLEMENTARY NOTES					
14. ABSTRACT  This report describes the characterization of the viscoelastic properties of polyurea and the failure of ductile materials at high strain rates. The mechanical properties of polyurea were determined under monotonic loading conditions, both in the unconfined and confined compression configurations. Direct measurements of the volumetric and shear response has been used to show that the shear resistance is nearly negligible, while the bulk modulus increases significantly with pressure. Expanding ring experiments were performed on Al 6061-O in order to determine the onset and growth of necking localization and eventual failure. Real-time images of the failure process were obtained and analyzed to determine the criterion for dynamic strain localization in uniaxial tension. Further work on expanding ring with polyurea coating will be performed through a continuing research program at the University of Texas at Austin.					
15. SUBJECT TERMS					
16. SECURITY CLASSIFICATION OF:			17. LIMITATION OF ABSTRACT	18. NUMBER OF PAGES 77	19a. NAME OF RESPONSIBLE PERSON
a. REPORT	b. ABSTRACT	c. THIS PAGE			19b. TELEPHONE NUMBER (Include area code)

## 1. Contract Information

Contract Number	N00014-05-1-0400
Title of Research	Experimental Characterization of Nonlinear Viscoelastic and Adhesive Properties of Elastomers
Principal Investigator	K. Ravi-Chandar
Organization	The University of Texas at Austin

## 2. Technical Section

### 2.1. Technical Objectives

Recent discussions surrounding the high rate behavior of polymers and their influence on the behavior of metallic structures when used as coatings have dealt with the issue of constitutive description largely along quasi-elastic lines of thinking (*e.g.* role of Poisson's ratio). Inasmuch as it is well known by now that volumetric deformations play a crucial role in time-dependent polymer response, it is definitely more appropriate to formulate constitutive behavior in terms of bulk and shear response. This is the classical way of formulating small deformation problems (Poisson's ratio enters as a convenient alternate characterization derivable from the latter properties).

To proceed to the formulation of a constitutive description it would seem best to start from a small deformation description, which is undisputedly accepted today and then proceed from there to examine the variations arising from larger strains. Thus, the first technical objective deals with the determination of the time-dependent (relaxation) response in bulk (volume) and shear. This is the data that is needed as a first input to evaluating constitutive models that are based on free volume or enthalpy for their nonlinear contribution. The confined compression experiment provides an appropriate method for characterizing the viscoelastic response of the polymer.

A direct consequence of the constitutive formulation and its practical evaluation is the need to test the evolving constitutive model on physically well described and experimentally well documented situations that are not overshadowed by complex geometry or history effects. This situation is provided by the dynamically expanding ring geometry.

Finally, polymer-steel adhesion under quasi-static as well as dynamic loading conditions must be determined through direct experiment. In this study, time-dependent interfacial fracture is addressed, including the effects of temperature and aggressive environments. Thus, the three main technical objectives of the program are listed below.

1. To determine the nonlinear, pressure dependent relaxation characteristics of polyurea
2. To determine the efficacy of polyurea coating on metallic specimens in the inhibition or delay of necking and associated fragmentation using the expanding ring experiment
3. To determine the adhesive characteristics of polyurea coatings on metallic substrates.

This report documents the work accomplished over the period from March 1, 2005 to March 31, 2006. The work continues under a different grant number.

## 2.2. Technical Approach

### 2.2.1. Viscoelastic Characterization of Polyurea:

The pressure dependent relaxation behavior of polyurea is determined with the confined compression loading configuration. If the specimen is confined in a cylinder of different wall-thicknesses, and axially compressed, the specimen experiences a multiaxial compressive stress state, consisting of a pressure and superposed shear. This arrangement, shown in Figure 1, has been used to determine the influence of pressure on the relaxation behavior. Ravi-Chandar and Ma (2000) showed that this configuration can be used for the simultaneous measurement of shear and bulk elastic, inelastic and viscoelastic properties of materials. Qvale and Ravi-Chandar, (2004) used the same configuration to evaluate the influence of pressure on the relaxation behavior polymethylmethacrylate and polycarbonate. Park, Liechti and Roy (2004) recently used the confined cylinder experiment to determine the shear and bulk linear viscoelastic behavior of an epoxy. This data formed the basis for the development, with additional ramp tension and shear experiments of a model of nonlinear viscoelasticity that accounted for hygrothermal effects in addition to large tensile and shear strains. In the confined compression test, one can obtain all components of the stress and strain state in the specimen from measurements of the axial stress,  $\sigma_a$ , axial strain,  $\epsilon_a$ , and hoop strain of the confining cylinder,  $\epsilon_h$ .

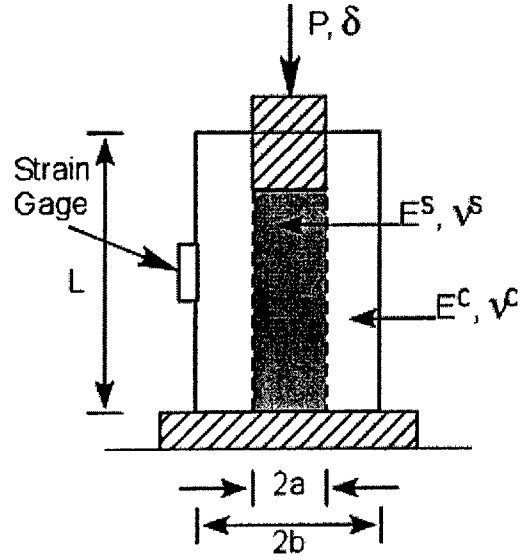


Figure 1. Confined compression configuration for multiaxial constitutive characterization.

$$\begin{aligned}
 \sigma_{rr}(t) = \sigma_{\theta\theta} &= -\frac{(b/a)^2 - 1}{2} E^c \epsilon_h(t) \\
 \sigma_{zz}(t) = \sigma_a(t) &\cdots \text{measured using the load cell} \\
 \epsilon_{rr}(t) = \epsilon_{\theta\theta} &= \frac{\epsilon_h(t)}{2} \left[ (1 - \nu^c) + (1 + \nu^c) \frac{b^2}{a^2} \right] \equiv \beta \epsilon_h(t) \\
 \epsilon_{zz} = \epsilon_a &\cdots \text{imposed by the loading frame and measured}
 \end{aligned} \tag{1}$$

where  $E^c$ ,  $\nu^c$  is the modulus of elasticity and Poisson's ratio of the confining cylinder and  $a$ ,  $b$  are the inner and outer radii of the confining cylinder. Results of our investigations on polyurea in the confined compression configuration are discussed in Section 2.3.1.

It is quite difficult to produce pure shear loading in actual laboratory experimentation. However, the Arcan test arrangement has been shown to produce reasonably uniform pure shear loading within the gage section of the specimens (Liang and Liechti, 1996). Thus, the Arcan test was used in the direct characterization of the nonlinear behavior of the polyurea; these results will be compared with the shear behavior interpreted from the confined compression tests described above.

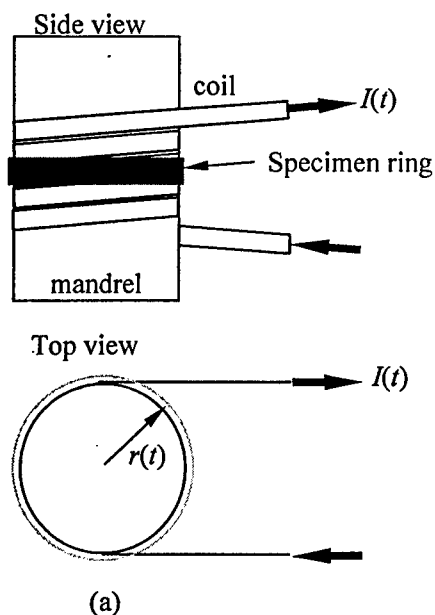


Figure 2. (a) Arrangement of the expanding ring experiment. A coil is wrapped around a mandrel and fixed in position. The specimen ring is just outside the coil and experiences an induced current that results in the radial expansion. The specimen expansion will be photographed using a high speed camera in the top view, allowing measurement of  $r(t)$ . (b) Free-body-diagram of a segment of the expanding ring.

The Arcan test consists of a butterfly-shaped specimen attached to two semicircular grips. Specimens are clamped and bonded to the grip using a high strength adhesive. The relative displacement of the right (lower) grip results in a shearing of the specimen. A uniaxial test machine was used to apply a constant displacement rate and the resulting load was measured with a load cell. The load, machine displacement and LVDT signal were recorded with a personal computer and a 16-bit A/D and used for determination of the shear response.

#### 2.2.2. Expanding Ring Experiment for Fragmentation Studies:

Expanding ring tests have been used frequently in the characterization of high strain rate material behavior. We believe this to be the hallmark experiment verifying the basic theory of why elastomers delay local instabilities according to observations at Carderock and in the analyses of Freund and Hutchinson studies. Following on Mott's explanation of fragmentation in pipe bombs (Mott, 1947), the earliest attempt at the expanding ring test seems to be that of Niordson (1965) who used the Lorentz interaction between a coil carrying current and a conducting ring; others have adopted the idea of the expanding ring with explosive and well as electromagnetic loading schemes (see for example, Hoggatt and Recht, 1969, and Walling and Forrestal, 1973). Grady and Benson (1983) and Gourdin (1989) have performed expanding ring experiments with speeds in the range of 200 m/s on rings of cross-section 1 mm x 1 mm and 3 cm diameter. While these tests are instrumented typically with a VISAR, Niordson used a still camera to obtain pictures of arc discharges at the onset of fragmentation; Grady and Benson (1983) used a streak camera to determine expansion speed. The experimental arrangement is shown in Figure 2a. A free-body-diagram of a segment of the expanding ring is shown in Figure 2b. During the expansion, and prior to the onset of necking, the stress and strain in the ring can be obtained if the radius  $r(t)$  is obtained from experiments. The stress,  $\sigma$ , resolved in the radial direction must equal mass per unit cross sectional area,  $\gamma$ , times the acceleration; thus,  $\sigma = \gamma \ddot{r}$ . The true strain  $e = \ln(r/r_0)$  can be obtained from a measurement of  $r(t)$ . Typically, in the ring expansion test, there appears a region of constant deceleration and measurements are the most reliable in this range.

It is important to note two key points about the expanding ring experiment: first, the specimen may be heated by electrical losses, but this can be calculated from the current measurements. Second, kinematic quantities as well as the driving forces are obtained in the experiment. Since the radial expansion is driven

by the Lorentz interaction between the coil and the ring, and since the current in the coil is measured directly in the experiment the radial pressure on the ring that drives the radial expansion is obtained. Guduru and Freund (2002) have examined analytically multiple neck formation in high strain rate extension of ductile materials under uniaxial loading. This analysis is intended as a model of the expanding ring experiment and we will use it as the guide for interpreting our experimental results. By performing such experiments with bare metal rings and polymer-coated rings, we are able to provide quantitative experimental results on the efficacy of the coating in inhibiting neck formation as well as a definitive geometry and load history against which computational models can be evaluated. We perform such expanding experiments and obtain high-resolution photographs at about 11  $\mu\text{s}$  time intervals. These high speed photographs provide not only the strain as a function of time, but also the time sequence of the necking and fragmentation events and are discussed in Section 2.3.2.

### 2.2.3. Adhesion of Polyurea to Steel Substrates:

The efficacy of the polymer coatings of steel under dynamic loading is bound to depend on the degree of adhesion between the two. This is likely to vary with time, not only due to the polymeric nature of the coating but also because of the diffusion of moisture through the coating and along the interface. The latter can often dominate and cause rapid deterioration of the strength, toughness and durability of the interface.

The adhesion of the coatings to steel is being examined under quasi static and dynamic conditions. The former is used to determine the toughness of the interface as a function of crack growth rate and environmental exposure. This will allow the effect of residual toughness on the impact resistance of a coated component to be determined in the second phase, where coated specimens will be subject to dynamic loadings.

For the quasi-static work, driven wedge tests (Figure 3) are conducted to determine the interfacial toughness of steel/coating interfaces as a function of wedge speed and environmental exposure. The wedge is driven by the actuator of a servo hydraulic testing machine. The flexibility of the wedge is designed to be appropriate for the stiffness of the polymer. A long working distance microscope is used to track the crack front and the crack opening profile. The series of experiments are conducted under wet and dry conditions. The interfacial toughness can be extracted from finite element analyses that account for the rate dependence of the polymeric coatings in their dry and saturated states. This arrangement worked very well (Park et al., 2005) for polymer coatings on concrete and is directly applicable to the work on polyurea.

For the planned experiments under dynamic loading, an electromagnetic loading device (Figure 4) will be used to apply controlled tensile loading pulses to the steel plates, the external surfaces of the coatings and/or the surfaces of pre existing delaminations between the steel and coatings. The angled web allows mixed-mode loading to be applied to the interface. The resulting damage or crack growth will be tracked with

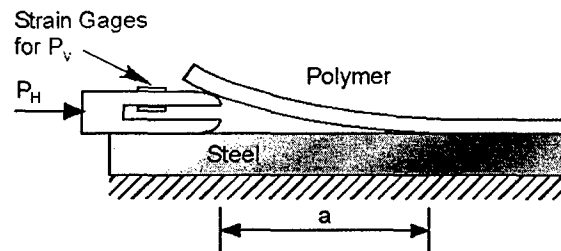


Figure 3. A schematic of the driven wedge test for polymer/steel adhesion at different rates, temperatures and solvent concentrations

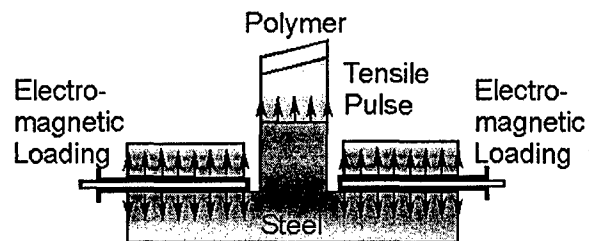


Figure 4. Dynamic loading device for probing interfacial strength at high rates.

a high speed camera. It is expected that these experiments will provide insights into the mechanics and mechanisms that provide the dynamic delamination that has been seen in preliminary work.

## 2.3. Technical Accomplishments

### 2.3.1. Viscoelastic Characterization of Polyurea:

Under uniaxial compression, polyurea exhibits a nonlinear, inelastic stress-strain response as shown in Figure 5. Results from two different types of polyurea<sup>1</sup>, one that was cast and the other one prepared by a proprietary spray process are shown in this figure. Significant differences are seen both in the loading and the unloading responses. For the early linear elastic part, we can determine that the modulus of elasticity for the two materials are 70 MPa and 180 MPa respectively. Typically, this measurement would be augmented with the incompressibility of the material to obtain the constitutive response for the material; in fact it is a very common practice to generalize the one-dimensional characterization to three-dimensional states by considering the complete stress-strain curve from the uniaxial experiment in terms of the effective stress vs effective strain. The multiaxial characterization that we present here indicates that this is not appropriate for the polyurea examined in this work.

The relaxation modulus, measured under uniaxial compression is shown in Figure 6 both for the cast and sprayed materials. Again, significant differences are observed in the two materials, even though the two materials are nominally the same composition and their glass transition temperature is nearly the same. This difference points to the need to characterize the actual material to be used in applications, rather than generate data on generic versions of the polyurea.

The confined compression configuration provides a direct method for evaluation of the multiaxial stress-strain behavior of the material; results from this test are attached in Appendix A. Further tests to evaluate the pressure dependence of the relaxation modulus will be performed under the follow-on program.

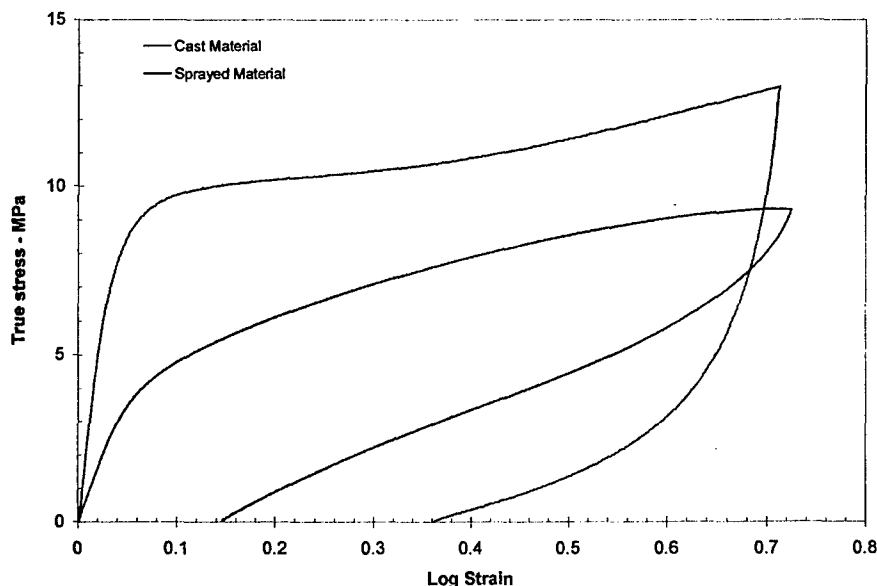


Figure 5. Uniaxial stress-strain response of two types of polyurea.

<sup>1</sup> Cast material was supplied by Jeff Fedderly of Naval Surface Warfare Center, and the sprayed material was supplied by TRI/Ausin Inc.

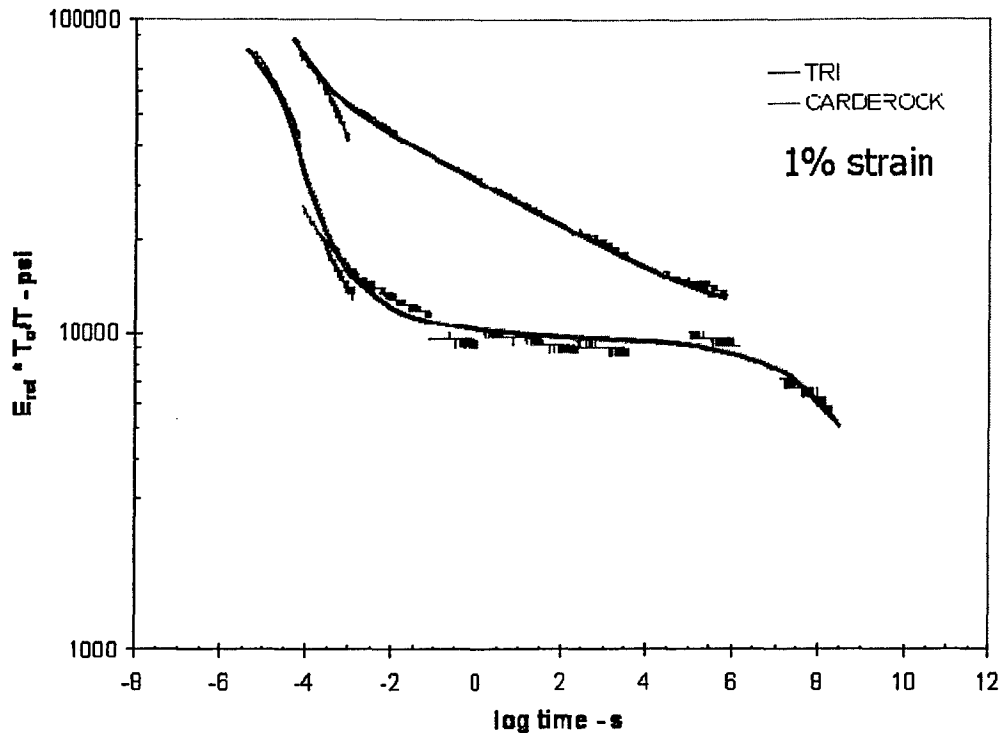


Figure 6. Uniaxial relaxation modulus master curves for polyurea, corresponding to a reference temperature of 10 C.

### 2.3.2. Expanding Ring Test:

Significant accomplishments were made in the expanding ring experiment. A manuscript has been submitted to the International Journal of Fracture. Rather than duplicate the material in this report, this manuscript is attached to this report as an Appendix B. The work performed under this grant has been on bare aluminum rings in order to evaluate the baseline properties of the material. Expanding ring experiments on polyurea coated rings will be performed under a new grant.

### 2.3.3. Adhesion of Polyurea to Steel:

We have designed and tested two types of interfacial fracture specimens under quasi-static loading: the double cantilever beam (DCB) and the end-notched flexure (ENF), in order to assess the interfacial fracture toughness and extract traction-separation laws of the polyurethane/steel interface in mode I and Mode II, respectively.

In order to estimate the fracture toughness for the proper design of the DCB and ENF specimens, a driven wedge experiment, i.e., asymmetric double cantilever, was performed. The specimen consists of a steel adherend coated with a layer of polyurethane, as shown in Figure 15(a). A Teflon-coated insert between the two adherends served as the initial crack. For steady state crack growth, the wedge was driven towards the initial crack front. The crack length ( $a_s$ ) was measured in real time by a digital video camera. The fracture toughness is given as



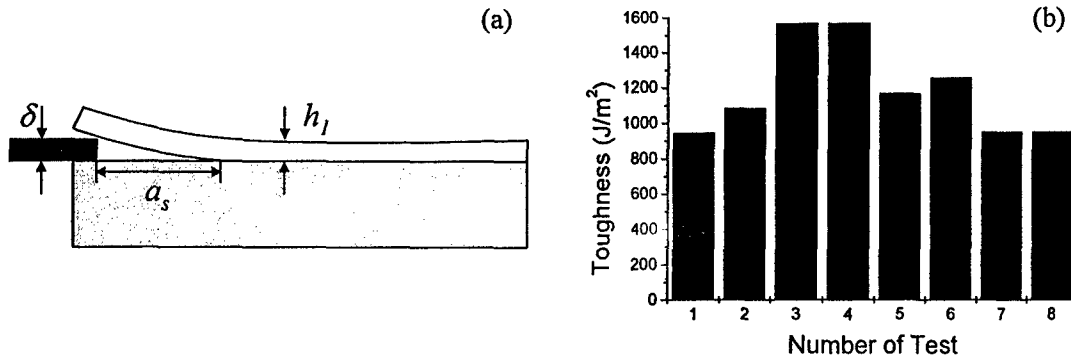


Figure 15. (a) Schematic of the driven wedge experiment showing a layer of adhesive coating a steel substrate. (b) Fracture toughness distribution obtained from the driven wedge experiment.

$$G = \frac{P^2}{2b} \frac{\partial C}{\partial a} = \frac{3\delta^2 E h_1^3}{8(a_s)^4} \quad (2)$$

where  $\delta$  is the wedge height,  $E$  is the Young's modulus of the adhesive, and  $h_1$  is the thickness of the adhesive. Figure 15(b) depicts the calculated fracture toughness for each measured crack length. The average value is  $1182 \text{ J/m}^2$ . Based on the above estimated fracture toughness and other considerations, e.g., no yielding in the steel adherends, measurable crack opening and measurable load level, we designed the DCB and ENF specimens (Fig. 16a) with the following dimensions:  $L = 100 \text{ mm}$ ,  $h = 4 \text{ mm}$ ,  $t = 0.25 \text{ mm}$  and  $b = 12.7 \text{ mm}$ .

Two Teflon-coated inserts of a well-defined thickness were placed at the ends of the zone to be bonded. The inserts ensured a uniform bonding thickness. The adhesive was applied between the inserts and then the adherends were joined. The specimens were cured at room temperature for 2 days. They were then tested at room temperature using a servohydraulic universal testing machine under a constant cross head speed of  $1.27 \text{ mm/min}$ . We first tested DCB specimens (Fig. 16a) using a  $500 \text{ lb}$  load cell and measured the crack length using a digital video camera. The energy release rate for this configuration is

$$G = \frac{12(Pa)^2}{h^3 E_L} (1 + 0.677h/a)^2 \quad (3)$$

where  $a$  is the crack length,  $P$  is the applied load,  $E_L$  is the Young's modulus of the adherend, and  $h$  is the thickness of the adherend.

Figure 16(b) shows the fracture toughness as a function of the crack length. It is seen that the fracture toughness is much lower than the expected value. Observation of the fracture surface revealed that the separation occurred by adhesive failure, i.e. along the interface rather than by cohesive failure inside the adhesive layer. This is probably the main reason for the low fracture toughness value. Proper surface processing of the steel adherend is required to ensure better quality for the adhesion.

In addition, we tested ENF specimens. However, the crack was difficult to track due to the intimate contact between the two adherends under load. We are developing a new method to observe the crack growth. An array of dots with a spacing of  $0.127 \text{ mm}$  will be sprayed on the edge of the specimen that is

intersected by the crack faces. This is expected to reveal crack growth with a resolution at a fraction of the dot spacing. The work on characterization of adhesion continues under a follow-on program.

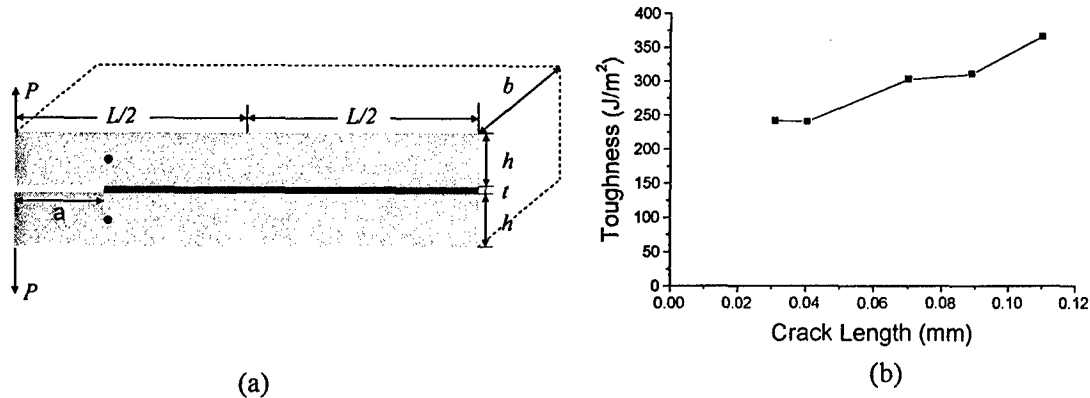


Figure 16. (a) Schematic of the DCB specimen showing a polyurethane layer sandwiched between two steel adherends. (b) Fracture toughness as a function of the crack length.

## References

- D.E. Grady and D.A. Benson, 1983, Fragmentation of metal rings by electromagnetic loading, *Experimental Mechanics*, **12**, 393-400.
- W.H. Gourdin, 1989, Analysis and assessment of electromagnetic ring expansion as a high-strain-rate test, *Journal of Applied Physics*, **65**, 411-422.
- P.R. Gududru and L.B. Freund, 2002, The dynamics of multiple neck formation and fragmentation in high rate extension of ductile materials, *International Journal of Solids and Structures*, **39**, 5615-5632.
- C.R. Hoggatt and R.F. Recht, 1969, Stress-strain data obtained at high rates using an expanding ring, *Experimental Mechanics*, **9**, 441-448.
- Y.-M. Liang and K.M. Liechti, 1996, On the Large Deformation and Localization Behavior of an Epoxy Resin Under Multiaxial Stress States, *International Journal of Solids and Structures*, **33**, 1479-1500.
- N.F. Mott, 1947, Fragmentation of shell cases, *Proceedings of the Royal Society London, Series A, Mathematical and Physical Sciences*, **189**, 300-308.
- F.I. Niordson, 1965, A unit for testing materials at high strain rates, *Experimental Mechanics*, **5**, 23-32.
- S. Park, K. M. Liechti and S. Roy, 2004, Simplified bulk experiments and hygrothermal nonlinear viscoelasticity, *Mechanics of Time Dependent Materials*, **8**, 303-344.

S. Park, K. M. Liechti and S. Roy, 2005, Durability of adhesive joints between concrete and FRP reinforcement in aggressive environments using a hygrothermal nonlinear viscoelastic fracture approach, *International Journal of Fracture*, submitted.

D. Qvale and K. Ravi-Chandar, 2004, Viscoelastic characterization of polymers under multiaxial compression, *Mechanics of Time Dependent Materials*, 2004, **8**, 193-214.

K. Ravi-Chandar and Z. Ma, 2000, Inelastic deformation in polymers under multiaxial loading, *Mechanics of Time-Dependent Materials*, **4**, 333-357.

H.C. Walling and M.J. Forrestal, 1973, Elastic-plastic expansion of 6061-T6 aluminum rings, *J. AIAA*, **11**, 1196

## APPENDIX A: Manuscript on Constitutive Characterization of Polyurea under Pressure

### Characterization of Multiaxial Constitutive Properties of Rubbery Polymers

V. Chakkarapani , K. Ravi-Chandar, and K.M. Liechti  
Center for Mechanics of Solids, Structures, and Materials  
Department of Aerospace Engineering and Engineering Mechanics  
The University of Texas at Austin  
Austin, TX 78712-0235

*(to appear in the Journal of Engineering Materials and Technology, October 2006)*

**Abstract.** Rubbery response of polyurea is examined under monotonic loading in the confined compression, composite compression and Arcan shear configurations. For polyurea prepared by a casting process, it is shown that while the bulk response is significantly nonlinear, and well fitted by the Tait equation, the shear resistance is extremely small. In contrast, polyurea formed by a spray process shows significant compressibility, inelastic volumetric deformation, and significantly enhanced shear resistance.

**Key words:** polyurea, compressibility, shear response, confined compression, Arcan test

#### 1. Introduction

Elastomers and other similar rubbery materials are used as load bearing members in many engineering applications. It is essential to determine their constitutive properties in order to provide efficient designs and appropriate determination of their reliability. Characterization of constitutive properties of these materials is typically restricted to the determination of uniaxial stress-strain curves in a tension or compression test, or the characterization of complex moduli for evaluation of viscoelastic or dissipative characteristics. It is implicitly assumed that generalization to multiaxial conditions can be effected by imposing incompressibility of the material or effectively setting the Poisson's ratio to 0.5. Relaxation modulus and creep compliance are also typically determined under uniaxial loading conditions and time-temperature equivalence is used to obtain a master relaxation or creep characterization. For some high performance applications, such characterization turns out to be inadequate and it is necessary to determine the constitutive behavior under multiaxial loading conditions directly.

In this paper, we address the characterization of the constitutive response of polyurea under conditions of monotonic loading. Some issues related to the characterization of the viscoelastic response are also discussed. The paper is organized as follows: the experimental methods used to determine the constitutive response of the elastomer are described in Section 2. This includes the confined compression apparatus, the composite cylinder configuration, (both of which are geared for the simultaneous measurement of the bulk and shear properties) and the Arcan configuration for direct evaluation of the shear response. Specific results corresponding to polyurea are described in Section 3; in particular, the ability to measure shear properties at different pressure

levels is highlighted. These results, which indicate a liquid-like response for the polyurea, are discussed in Section 4 in light of some recent experiments on impact response of polyurea.

## 2. Experimental Setup

We have used three different experimental arrangements to examine the behavior of polyurea – the confined compression test [1], the composite compression test developed in this study and the Arcan test for shear [2,3]. These experimental configurations are described in this section.

### 2.1. Confined Compression Test

In order to apply a uniform multiaxial compressive deformation and to inhibit buckling and or barreling during the experiment, the confined compression configuration shown in Figure 1 was developed by Ma and Ravi-Chandar [1]; they showed that this configuration can be used for the simultaneous measurement of shear and bulk elastic, inelastic and viscoelastic properties of materials. The specimen to be tested is a cylindrical rod of diameter  $2a$  and length  $L$ . The confining cylinder used has an inner diameter of  $2a$  and outer diameter of  $2b$ . The material for the confining cylinder must be chosen such that it will provide adequate restraint to the specimen, and remain compliant enough to allow for measurement of its deformation during the test. In addition, the confining cylinder should deform elastically during the test or else a new cylinder will be required for each test. The specimen is uniformly strained by displacing the steel loading pins in a loading frame; thus,  $\epsilon_{zz}$  is equal to some known, fixed value,  $\epsilon_a$ ; in the confined compression experiment, this is measured as the movement of the loading crosshead divided by the gage length of the specimen. The axial stress,  $\sigma_{zz}$  that results from this straining is uniform throughout the specimen and can be measured using a load cell mounted in the loading frame; let us denote this by  $\sigma_a$ . Upon application of the axial strain, the confining cylinder provides restraint to the transverse expansion of the specimen. The radial pressure that results on the inner surface of the confining cylinder and outer surface of the specimen are of equal magnitude, and continuity of the stresses at this interface may be written as:  $\sigma_{rr}(a) = \sigma_{rr}^{cyl}(a) = -\sigma$  assuming that complete contact is always maintained:  $u_r(a) = u_r^{cyl}(a)$ . Stresses, strains, and displacements in the confining cylinder can be found from the Lamé solution [4], and are found to be functions of the unknown stress  $\sigma$ . The value of  $\sigma$  can be related to the hoop strain measured at the outer surface of the confining cylinder,  $\epsilon_h$ . This hoop strain can also be used to calculate the displacement at the inner surface of the confining cylinder.

It can now be shown that a complete description of the state of stress and strain in the specimen may be obtained from measurements of the axial stress,  $\sigma_a$ , axial strain,  $\epsilon_a$ , and hoop strain of the confining cylinder,  $\epsilon_h$  (see [1]). The state of stress and strain in the specimen is displayed below:

$$\begin{aligned}
\sigma_{rr} = \sigma_{\theta\theta} &= -\frac{(b/a)^2 - 1}{2} E_c \varepsilon_h \\
\sigma_{zz} &= \sigma_a \\
\varepsilon_{rr} = \varepsilon_{\theta\theta} &= \frac{\varepsilon_h}{2} \left[ (1 - \nu_c) + (1 + \nu_c) \frac{b^2}{a^2} \right] \equiv \beta \varepsilon_h \\
\varepsilon_{zz} &= \varepsilon_a
\end{aligned} \tag{1}$$

$E_c$ , and  $\nu_c$ , are the elastic modulus and Poisson's ratio of the confining cylinder. It should be noted that the above analysis assumes the deformation of the confining cylinder to be elastic, a condition which may be ensured by appropriate choice of the confining cylinder's material and dimensions. Because the now known values of stress and strain are the principal values, a straightforward characterization of the constitutive response of the specimen may be obtained. It is useful to separate the experimental data into dilatational and deviatoric parts. For the confined compression configuration, the mean stress and volumetric dilatation are

$$\sigma_m = \frac{\sigma_{zz} + 2\sigma_{rr}}{3} \text{ and } \mathcal{J} = \varepsilon_{zz} + 2\varepsilon_{rr}. \tag{2}$$

and the deviatoric components of stress and strain are

$$s_{zz} = \frac{2}{3} [\sigma_{zz} - \sigma_{rr}] \text{ and } s_{rr} = s_{\theta\theta} = -\frac{1}{3} [\sigma_{zz} - \sigma_{rr}], \tag{3}$$

$$e_{zz} = \frac{2}{3} [\varepsilon_{zz} - \varepsilon_{rr}] \text{ and } e_{rr} = e_{\theta\theta} = -\frac{1}{3} [\varepsilon_{zz} - \varepsilon_{rr}], \tag{4}$$

with all other components being zero. Hence, the experimental measurements in the confined compression apparatus enable the simultaneous measurement of bulk and shear properties, without *a priori* imposition of any constitutive models. Qvale and Ravi-Chandar [5] used the same configuration to evaluate the influence of pressure on the relaxation behavior; one must impose a step axial strain and simply monitor the time variation of the axial load and the hoop strain in the confining cylinder to determine the bulk and shear relaxation behavior. Park et al., [6] recently used the confined cylinder experiment to determine the shear and bulk linear viscoelastic behavior of an epoxy. This data formed the basis for the development, with additional ramp tension and shear experiments, of a model of nonlinear viscoelasticity that accounted for hygrothermal effects in addition to large tensile and shear strains.

## 2.2. Composite Compression Test

One major hurdle in using the confined compression test configuration for the characterization of polyurea is the large difference in the stiffness of the specimen and the confining cylinder; this results a rapid increase in the mean stress while the corresponding increase in the shear stress is very small. Hence only a small part of the mean stress vs. shear stress space can be probed. In an attempt to circumvent this problem, we designed an alternate configuration, called the composite

compression specimen, where the specimen is surrounded by a cladding cylinder of the same length and this composite specimen is subjected to a uniaxial strain in a loading machine; this loading scheme is shown in Figure 2. In this case, the cladding cylinder and the specimen are subjected to the same axial strain  $\epsilon_a = \delta/L$ ; this strain is measured with a strain gage on the cladding cylinder. In addition, the axial load  $P$  and hoop strain  $\epsilon_h$  on the cladding cylinder are measured in this experiment. If the cladding is a thin-walled cylinder (we anticipate the diameter to wall thickness to be greater than at least 25), it is readily seen that the strains measured on the cladding are also the strains to which the specimen is subjected. We can write explicit expressions for the stress components in the specimen as follows:

$$\begin{aligned}\sigma_{rr} = \sigma_{\theta\theta} &= \frac{E_c t / R}{1 - \nu_c^2} [\epsilon_h + \nu_c \epsilon_a] \\ \sigma_{zz} &= \frac{P}{A_s} - \frac{A_c E_c}{A_s (1 - \nu_c^2)} [\epsilon_a + \nu_c \epsilon_h]\end{aligned}\quad (5)$$

where  $R$  and  $t$  are the cladding cylinder radius and wall thickness and  $A_s$  and  $A_c$  are the cross-sectional areas of the specimen and cladding respectively. The mean and deviatoric quantities can again be determined from Eqs. (2-4). A quick estimate of the radial pressure generated in the specimen can be obtained by considering the specimen to be elastic with modulus  $E_s$ , and Poisson's ratio  $\nu_s$ ; this results in

$$p = \frac{(\nu_c - \nu_s) \epsilon_z}{\left[ \frac{(1 - \nu_c^2)(R/t)}{E_c} + \frac{(1 + \nu_s)(1 - 2\nu_s)}{E_s} \right]}\quad (6)$$

Thus, the confining pressure is simply a result of the Poisson's ratio difference between the specimen and the cladding cylinder. Since this difference is small, we anticipate that the mean pressure developed will also be small, thereby enabling a different range of pressure-shear to be explored in this configuration in comparison to the confined compression arrangement.

### 2.3. Arcan Shear Test

It is quite difficult to produce pure shear loadings in actual laboratory experimentation. However, the Arcan test arrangement has been shown to produce reasonably uniform pure shear loading within the gage section of the specimens [2,3]. The Arcan test consists of a butterfly-shaped specimen attached to two semicircular grips, as shown in Figure 3. Specimens were clamped and bonded to the grip using a high strength adhesive. As shown, the relative displacement of the right (lower) grip results in a shearing of the specimen. A uniaxial test machine was used to apply a constant displacement rate and the resulting load was measured with a load cell. An LVDT with a 5 mm range was used to measure the relative grip displacement across the specimen. The load, machine displacement and LVDT signals were recorded with a personal computer and a 16-bit A/D and used for determination of the shear response. Thus, the Arcan test was used in the direct characterization of the nonlinear behavior

of the polyurea; these results will be compared with the shear behavior inferred from the confined compression and composite cylinder tests described above.

### 3. Response of Polyurea

#### 3.1. Uniaxial Response

Under uniaxial compression, polyurea exhibits a nonlinear, inelastic stress-strain response as shown in Figure 4. Results from two different types of polyurea, one that was cast and the other one prepared by a proprietary<sup>2</sup> spray process are shown in this figure. Significant differences are seen both in the loading and the unloading responses. For the early linear elastic part, we can determine that the modulus of elasticity for the cast and sprayed materials is 70 MPa and 180 MPa, respectively. Beyond about 6 MPa for the cast material and 10 MPa for the sprayed material, the material flows with very little resistance to large strain levels. Stiffening at large strain levels was observed for the sprayed material, but not the cast material. Typically, this measurement would be augmented with the incompressibility of the material to obtain the constitutive response for the material; in fact it is a very common practice to generalize the one-dimensional characterization to three-dimensional states by considering the complete stress-strain curve from the uniaxial experiment in terms of the effective stress vs. effective strain. The multi-axial characterization that we present here indicates that this is not appropriate for the polyurea examined in this work.

#### 3.2. Confined Compression Response

The confined compression configuration provides a direct method for evaluation of the multi-axial stress-strain behavior of the material; we discuss the cast material first. The variation of the axial stress with axial strain is shown in Figure 5. This test was performed on cast polyurea specimens, 9.56 mm in diameter and 20 mm long; the confining cylinder was made of steel with a modulus 200 GPa and Poisson's ratio of 0.3; the inner radius of the cylinder was equal to the radius of the specimen:  $a = 4.78$  mm and outer radius was fixed at two different values  $b = 7.17$  mm and  $b = 14.34$  mm, corresponding to  $b/a$  ratios 1.5 and 3. Significant nonlinearity as well as hysteresis upon unloading is observed in these experiments. Furthermore, stresses as high as 300 MPa, have been applied; this is of the order of the uniaxial modulus of the material! Such large stresses are possible as a result of the confinement provided by the steel cylinder. The radial stress on the specimen was calculated from the measured value of the hoop strain on the confining cylinder (see Eq. 1); the variation of the radial stress with the applied axial stress also shown in Figure 5 indicates that  $\sigma_{rr} \sim \sigma_{zz}$ , suggesting a nearly hydrostatic state of stress. From these measurements, we can determine the variation of the mean stress with the volume dilatation and the effective shear stress with the shear strain, as defined in Eqs. (2-4); these are shown in Figures 6 and 7. It is clear that the confined compression test has been able to separate out the bulk and shear response of the material; in particular, it is evident that the bulk response exhibits a significantly nonlinear behavior. Furthermore, the bulk response can be fitted well with the Tait equation that represents the compressibility of sea water,

$$\sigma_{kk} = B \left[ \exp\left(\frac{p}{C}\right) - 1 \right], \text{ where } B/C \text{ represents the bulk modulus and } C \text{ is a constant. The curve fit}$$

<sup>2</sup> TRI/Austin Inc.



shown in Figure 6 yielded  $B=210$  MPa and  $C = 0.1$ . There is a small hysteresis upon unloading, which is believed to be due to viscoelastic effects that have not been considered in this work. In contrast, the shear stress (Fig. 7) is well below 1 MPa during the entire loading history; a small linear region can be identified at strains below about 2%. This behavior is quite different from what one could have guessed from the uniaxial response, together with the assumption of incompressibility. The observed nearly constant shear flow stress, in conjunction with the nonlinear bulk behavior reminiscent of the compressibility of water, suggests that the cast polyurea exhibits fluid-like behavior under monotonic loading at room temperature! It is important to note that similar experiments in glassy polymers did not exhibit such response; the shear stress continued to evolve according to what one might estimate from uniaxial stress strain data through the effective stress calculations (see [7]). This liquid-like response must be material specific and applies to the cast polyurea used in the present study.

Differences between the cast material and the sprayed material are quite significant; while the cast material exhibits a nearly reversible (elastic) bulk response, the sprayed material exhibits significant compressibility as well as permanent deformation upon unloading. We believe that the spray process induces fine-scale porosity that underlies the compressibility and inelasticity. The Tait model is not suitable for such porous materials and hence a fit of this model was not attempted. In terms of the shear response, there is qualitatively very little difference between the two materials as seen in Figure 7, even though the sprayed material exhibits a greater resistance to shear flow, with a flow stress of about 6 MPa.

This response in shear is so startling that we must confirm this in other experimental configurations. We will examine this liquid-like response further, first with the composite cylinder configuration in Section 3.3 and then through direct measurements of the shear response in the Arcan test in Section 3.4.

### 3.3. Composite Cylinder Response

The composite cylinder test was prepared by casting a large block of polyurea (100 mm diameter cylinder, 100 mm long) and cladding it with a steel cylinder (100 mm diameter, 100 mm long and 1 mm wall thickness). The spray process was not used in generating such specimens, so the results described in this section correspond only to the cast material. The cladding cylinder was instrumented with two pairs of diametrically opposed gages aligned in the axial direction and two gages along the hoop direction. Average values from the axial and hoop gages were used to determine the applied strains:  $\epsilon_a$  and  $\epsilon_h$ . Load was applied to the composite specimen by placing it in a uniaxial test machine and displacing the cross-head at a constant rate; the applied load as well as the strains on the cladding cylinder were monitored and interpreted in terms of the stresses and strains in the polyurea specimen through Eqs. (2-5) as discussed above.

The requirements on machining tolerances in the composite cylinder configuration are quite stringent. The fit between the specimen and the cladding cylinder must be such that the hoop strain measurement in the cladding is representative of the hoop strain in the specimen; the length of the cylinder must match the length of the specimen closely in order that both experience the same axial strain. In spite of this, the composite cylinder must, for practical purposes, go through phases where the specimen alone is loaded first, then hoop constraint appears and finally the cladding and specimen are compressed together. Machining tolerances of about 12  $\mu\text{m}$  in radius and length were maintained in order to minimize such variations. An additional restriction arises from the fact that the cladding cylinder is extremely stiff and hence

only a small fraction of the applied load is taken by the polyurea specimen. The uniaxial strain at yield for the cladding cylinder is 0.0025, and hence the axial strain was limited in our composite cylinder tests to less than 0.0005, to avoid yielding of the cladding cylinder.

The variation of the axial and radial stress in the specimen with the axial strain in the cladding is shown in Figure 8. During the early stages of the axial loading, there appears to be incomplete contact between the specimen and cylinders, but by the time the cladding cylinder has experienced a strain of 0.000015, the specimen and cylinder are in perfect contact and one can use the analysis discussed in Section 2.2 to interpret the measurements. Since the steel cladding cylinder behaves in a linearly elastic manner in the range of strain used, the nonlinearity observed in the measurements must arise from the nonlinearity of the polyurea specimen. The mean and deviatoric components were calculated from these measurements and their variation with the axial strain measured in the cladding cylinder is shown in Figure 9. Focusing attention to strains larger than 0.000015, it is clear that, while the mean stress continues to increase with loading, the effective shear stress is very nearly constant at about 0.3 MPa, confirming the measurements in the confined cylinder configuration. The lower magnitude of the shear stress in this configuration could perhaps be attributed to the lower mean stress acting in this specimen.

We note that this configuration can also be used for simultaneous characterization of the viscoelastic response, simply by holding the applied strain and monitoring the load relaxation. However, performing tests at different temperatures, would pose significant problems in making the cladding and specimen fit appropriately over a large temperature range and hence has not been attempted.

### 3.4. Pure Shear Response

The low shear stresses measured in the confined compression and composite cylinder configurations suggest a liquid-like behavior for the cast polyurea. In order to confirm this response, we performed a direct shear measurement in the Arcan configuration. The variation of the shear stress with shear strain measured in this test on the cast and sprayed materials is shown in Figure 7. Clearly, the direct measurement falls nearly on the shear response inferred from the confined compression test; it also indicates that the shear stress reaches a constant plateau level at about 1 MPa for the cast material and about 6 MPa for the sprayed material. These experimental results suggest that, for the cast material, the shear stress remains constant and very low, and hence, one might be justified in considering the material to be liquid-like.

## 4. Conclusions

The multiaxial compressive behavior of a polyurea has been examined by performing experiments in confined compression, composite cylinder and Arcan configurations. It was found that the bulk deformation of the cast material was nonlinear, but nearly reversible; furthermore it could be modeled by Tait's equation representing the compressibility of sea water:

$$\sigma_{kk} = B \left[ \exp\left(\frac{g}{C}\right) - 1 \right] \quad (7)$$

Furthermore, the shear stress was found to be limited to very low levels for the cast material that, for all practical purposes, one might ignore the shear resistance. Alternatively, the shear response

can be represented in terms of a fluid:  $s_{ij} = s_{ij}(\dot{\epsilon}_{ij}, \sigma_m)$  with some dependence on the mean stress. There is some evidence that the fluid-like model will work well for high strain rate problems; recent experiments have shown that when a cylindrical block of polyurea is impacted onto a rigid steel surface at high speeds, the deformation of the cylindrical block resembles that of a fluid jet impinging on a flat plate [8]. Significant differences were found between polyurea processed by casting into molds versus polyurea generated by spray process. Further work on modeling the observed response is underway.

### Acknowledgement

This work was performed under a program entitled "Experimental Characterization of Nonlinear Viscoelastic and Adhesive Properties of Elastomer" sponsored by the Office of Naval Research (ONR Grant Number N00014-05-1-0400, Program Manager: Dr. Roshdy Barsoum); this support is gratefully acknowledged. We are also grateful to Dr. Jeff Fedderly of the Naval Surface Warfare Center, Carderock, who provided the cast samples of polyurea used in the present work.

### References

- [1] Z. Ma, and K. Ravi-Chandar, 2000, Confined compression – A stable homogeneous deformation for multiaxial constitutive characterization, *Experimental Mechanics*, **40**, 38-45.
- [2] M. Arcan, Z. Hashin, and A. Voloshin, 1978, A method to produce uniform plane -stress states with applications to fiber-reinforced materials, *Experimental Mechanics*, **18**, 141-146.
- [3] Y.-M. Liang and K.M. Liechti, 1996, On the large deformation and localization behavior of an epoxy resin under multiaxial stress states, *International Journal of Solids and Structures*, **33**, 1479-1500.
- [4] S.P. Timoshenko, and J.N. Goodier, 1934, *Theory of Elasticity*, McGraw-Hill, New York.
- [5] D. Qvale and K. Ravi-Chandar, 2004, Viscoelastic characterization of polymers under multiaxial compression, *Mechanics of Time Dependent Materials*, **8**, 193-214.
- [6] S.J. Park, K.M. Liechti, and S. Roy, 2004, Simplified bulk experiments and hygrothermal nonlinear viscoelasticity, *Journal of Time-Dependent Materials*, **8**, 303-344.
- [7] K. Ravi-Chandar, and Z. Ma, 2000, Inelastic deformation in polymers under multiaxial compression, *Mechanics of Time-Dependent Materials*, **4**, 333-357.
- [8] S. Nemat-Nasser, 2005, personal communication.

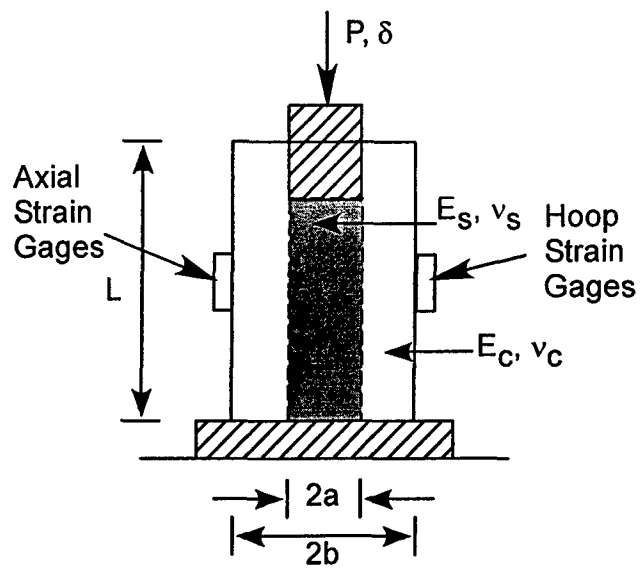


Figure 1. Confined compression configuration for multiaxial constitutive characterization.

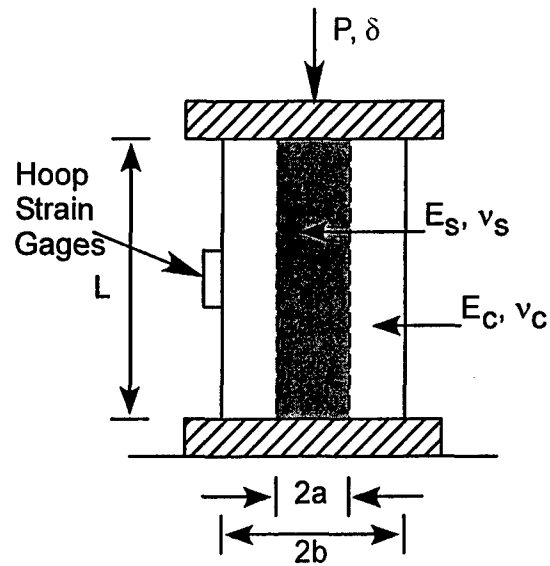


Figure 2. Composite compression configuration for multiaxial constitutive characterization.

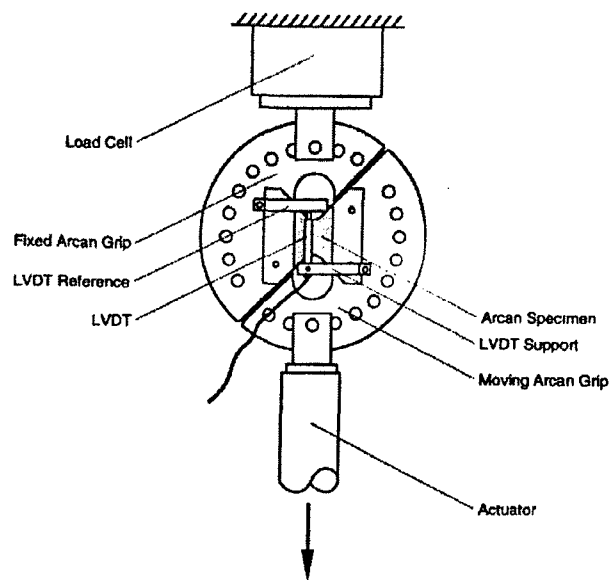


Figure 3. The Arcan specimen configuration for determination of shear response.

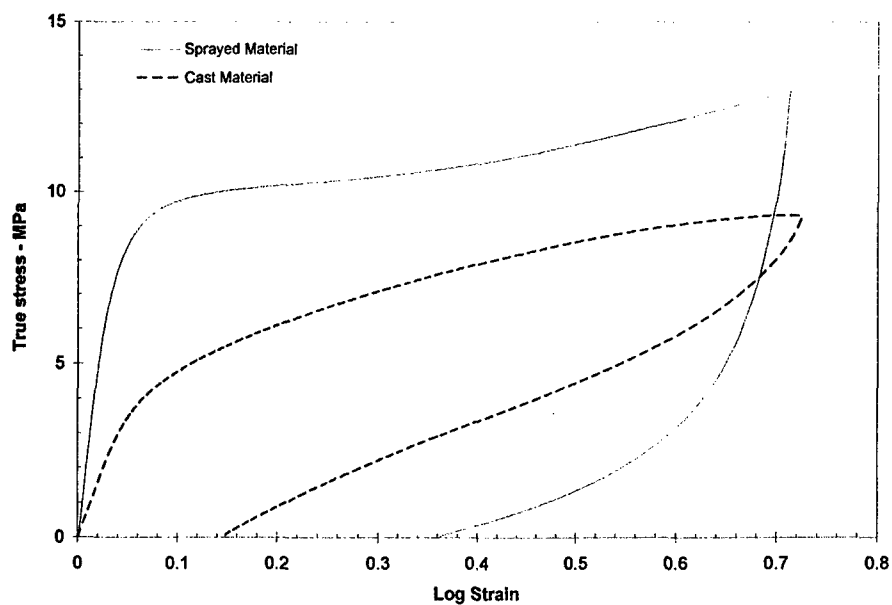


Figure 4. Uniaxial stress-strain response of two types of polyurea.

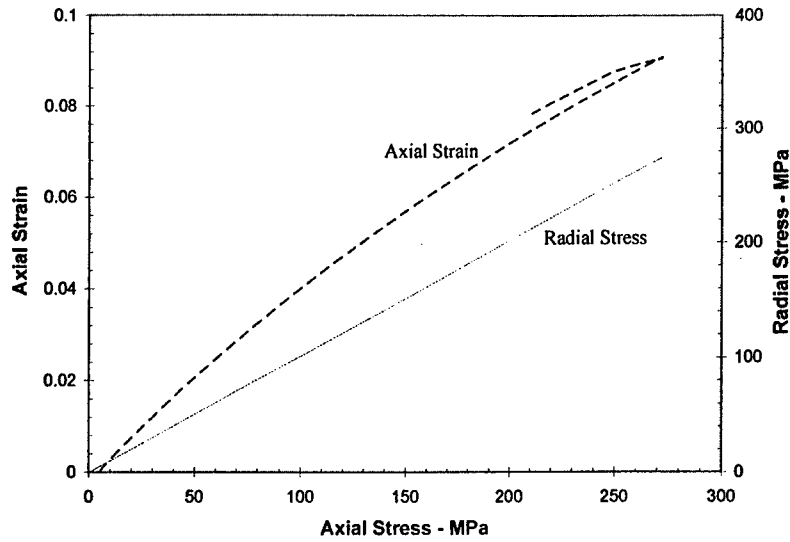


Figure 5. Variation of the axial stress with axial strain for the cast polyurea in the confined compression apparatus.

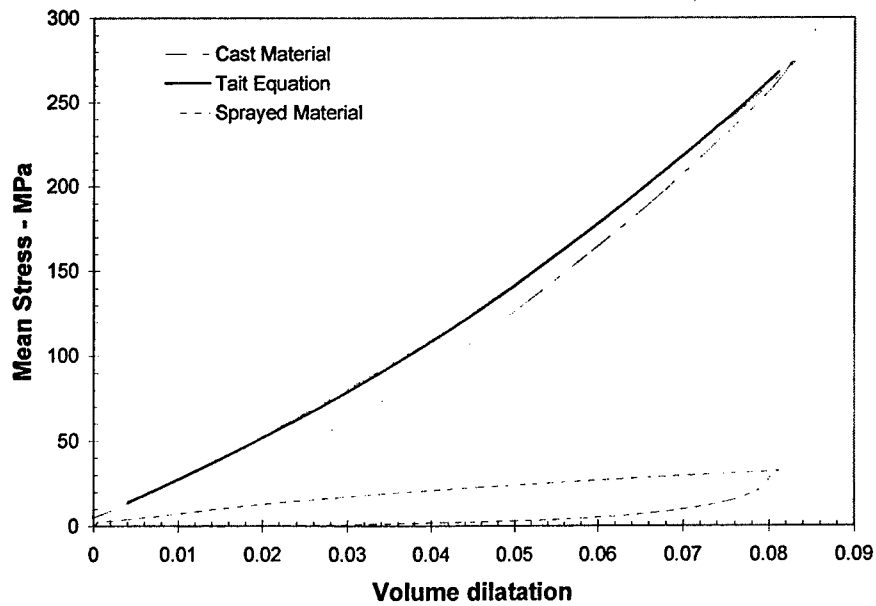


Figure 6. Variation of the mean stress with volume dilatation for polyurea.

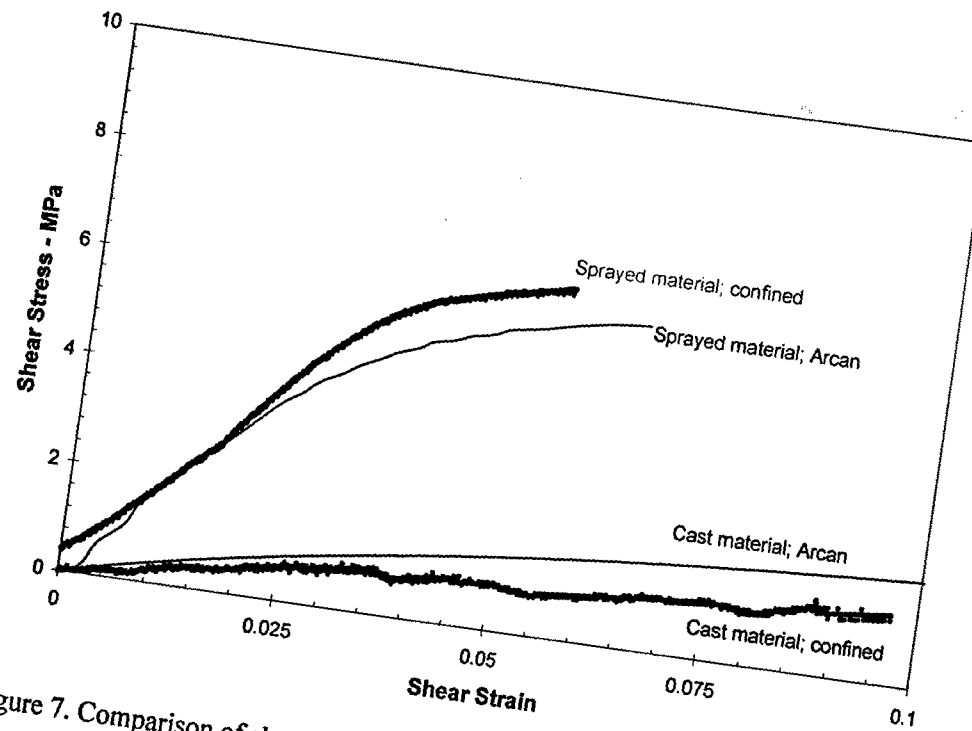


Figure 7. Comparison of shear response of cast and sprayed polyurea in the Arcan test configuration and the confined compression configuration.

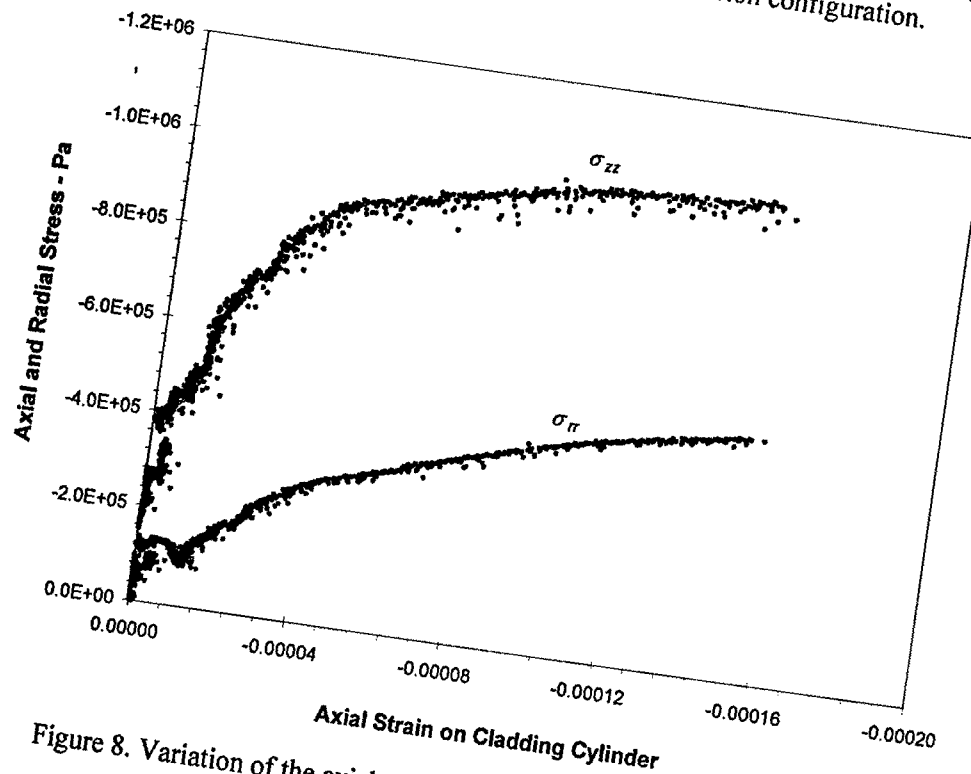


Figure 8. Variation of the axial and radial stress in the cast polyurea with axial loading.

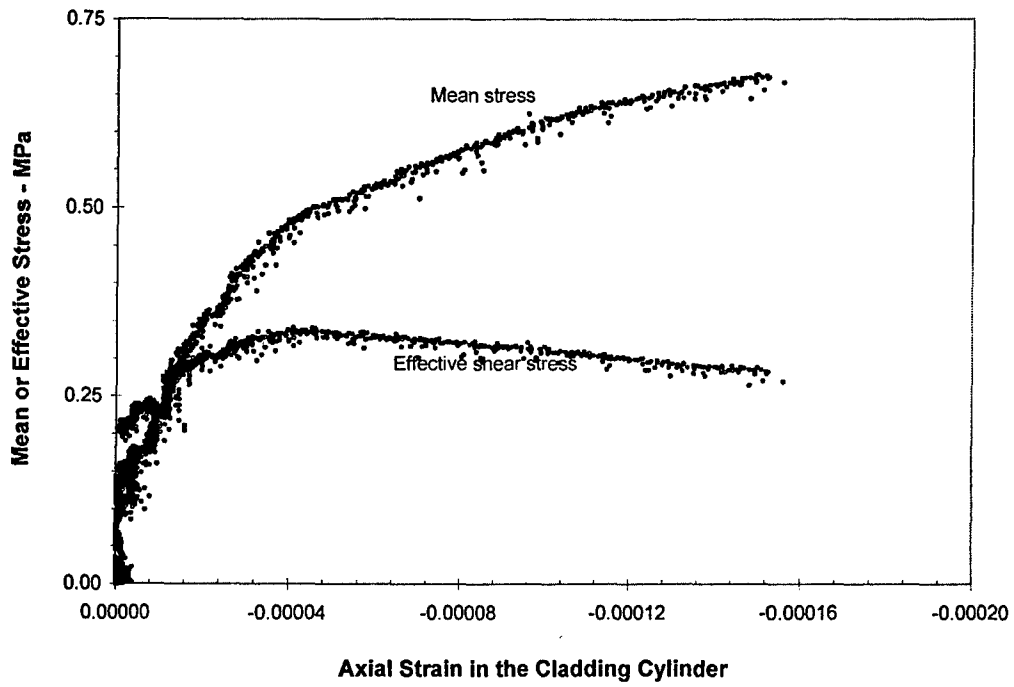


Figure 9. Bulk and shear response of the cast polyurea in the composite cylinder configuration.



## APPENDIX 2: Manuscript on Expanding Ring Experiments

### On the dynamics of necking and fragmentation – I. Real-time and post-mortem observations in Al 6061-O

H. Zhang and K. Ravi-Chandar

*Center for Mechanics of Solids, Structures and Materials  
Department of Aerospace Engineering and Engineering Mechanics  
The University of Texas at Austin, Austin, TX 78712-0235, USA*

#### Abstract

In this series of papers, we investigate the mechanics and physics of necking and fragmentation in ductile materials. The behavior of ductile metals at strain rates of about 10000 per second is considered. The expanding ring experiment is used as the vehicle for examining the material behavior in this range of strain rates. In the present paper, the details of the experiment and the experimental observations on Al 6061-O are reported. Specifically, the design of the expanding ring experiment is evaluated through an analysis of the electromagnetic and mechanical aspects of the problem. Then, through an innovative use of high-speed, high-spatial resolution imaging we determine the sequence of deformation and failure in the expanding ring. In particular, the high speed photographs reveal that multiple necks nucleate along the circumference of the ring near a critical strain level; this is followed by a sequence of fractures, and eventually the fragments are unloaded and move as a rigid body. The strain at the onset of localized deformation, the time of fracture initiation, and the sequence of fragmentation are all quantified in these experiments. These experimental results facilitate detailed comparison to analytical and numerical models of the fragmentation process. Following this, quantitative interpretation of the experimental observations is pursued. First, the uniform expansion of the ring is considered; the observed radial expansion is shown to agree well with an analytical solution of the problem based on a strain-rate-independent plasticity model. The evolution of the strain in the specimen and the onset of necking are evaluated quantitatively and shown to exhibit no dependence on the applied strain rate for this material; the strain at final fracture, averaged over the entire ring, is shown to be an inadequate measure of the ductility of the material. The fragmentation process is modeled with finite element analysis, incorporating the concept of the Mott release waves; this simulation provides a detailed numerical characterization of the experimental observations. Finally, the statistics of the necking and fragmentation are evaluated; these are interpreted both with the predictions of the linear perturbation analysis and a Weibull/Mott model of necking and fragmentation. In the sequel, we will explore the effect of material ductility, strain rate dependence, the effect of geometry and constraint, and finally the effect of a compliant cladding or coating on the development of necking and fragmentation.

Key words: expanding ring experiment, release waves, ductility,

#### 1. Introduction

Understanding the physics of fragmentation is important in a wide range of industrial, medical, military and geophysical applications. Commminution, shell case bursts, armor penetration, and meteoric cratering are instances where larger pieces of materials are fragmented into smaller pieces under strain rates of about  $10^4 \text{ s}^{-1}$ . Depending on the material and the strain rates, such fragmentation may be preceded by large plastic deformation or appear directly through brittle fracture; our interest in the present paper is focused on the former. Fragmentation of solids under such high strain rates has been a topic of intense research over the past five decades. Early investigation in this area was motivated by the work of Mott on the fragmentation of pipe bombs during World War II. Mott's insightful observations are documented in a paper written after the war (Mott, 1947). In the final analysis, Mott attributed the distribution of fragment sizes to the statistical variability in the strain to failure of the material and obtained this distribution through

an estimate of the propagation of the unloading or release waves from each fracture event (presumed independent). Since these early observations and estimates on fragmentation, a number of experimental, analytical and numerical investigations have been performed over the past five decades in a wide range of materials; the literature on the topic is quite large and we provide a concise summary of the approaches adopted in these investigations in order to place the present work in the proper context.

The experimental determination of the tensile strength of materials under high strain rate loading is a subject with a rich history. The most famous early results are from the experiments of the Hopkinsons (1872, 1910) who used impact loading on long wires to evaluate its strength and the pioneering experiments of von Karman and Duwez (1950) who impacted a wire with a projectile to generate higher strain rates and followed the plastic wave propagation in the wire to determine the strength. Kolsky's extensions to the split-Hopkinson apparatus and its variations have spawned significant efforts into the high strain rate characterization of tensile stress-strain response. Experimental investigation of tensile fracture and fragmentation response at high strain rates was pioneered by Niordson (1965), who designed an electromagnetic loading scheme to drive the expanding ring arrangement; while he demonstrated the capability of this scheme to enable high strain rate tensile experiments, only preliminary observations were reported in his paper. In particular, he showed a beautiful image obtained with illumination from the sparks that appeared at the fracture points due to the induced currents circulating in the specimen ring. Since about nine sparks were recorded along the ring, he suggested that the fractures must have occurred almost simultaneously. He also showed that the fracture occurred after shear localization at an angle to the direction of tension. Niordson suggested that strain measurements could be obtained with strain gages, although electromagnetic interference and dielectric shielding effects appear to be significant problems that may not be easily overcome. The capability of the expanding ring method was fully exploited by Grady and Benson (1983) who performed numerous experiments on OFHC copper and 1100-O aluminum; their measurements appear to be the most extensive data set to-date, that most analysts use these results for comparison with prediction. Grady and Benson used a streak camera to capture the time history of motion of a single point in the ring and thus were able to correlate the measured strain evolution in the expanding ring with lengths of the fragments collected after the test. The radial expansion speed of the ring was in the range of 18 to 220 m/s for the aluminum rings and 6 to 138 m/s for the copper rings; the corresponding strain rates were in the range of  $10^2$  to  $10^4$  s<sup>-1</sup>. Two sets of experimental observations were gathered from their expanding ring tests and a number of conclusions were drawn from these results. First, Grady and Benson (1983) noted that the recovered fragments contained remnant necks that had not completely fractured. Therefore, they tabulated the number of arrested necks and successful fractures that were recovered; the number of fragments increased almost linearly with expansion velocity. Second, they plotted the mass distribution of the fragments and compared it with the analysis of Mott; this suggested that while the release wave idea was in reasonable agreement with the experimental observations, there were a significant number of fragments outside the Mott estimate. Finally, Grady and Benson used the total length of all the collected fragments to obtain a measure of the strain at fracture, after cautiously warning the reader that any such definition "of a dynamic fracture strain is somewhat nebulous." Thus, their *ad hoc* dynamic fracture strain increased as a function of the expansion speed of the ring – from 0.222 to 0.45 for aluminum and 0.47 to 0.65 for copper; in contrast, the quasi-static strain to failure (unspecified gage length) was 0.075 and 0.40 for the aluminum and copper respectively. Unfortunately, many later studies have quoted this result as implying that there is an increase in material ductility with increasing strain rate. As we will show in this paper, this measure of "strain-at-fracture" has nothing to do with the ductility of the material.

Gourdin (1989) extended the applicability of the expanding ring experiment further by (i) incorporating a VISAR (Velocity Interferometer System for Any Reflector) to measure the

expansion speed accurately at high temporal resolution and (ii) suggesting clever methods for using conducting materials as pushers for testing nonconducting materials as specimens. He also worked out a complete electromagnetic model for the interaction between the current in the driving coil and the induced current in the expanding ring. Precise measurements of the radial expansion coupled with the theoretical model for the driving force allows for the stress-strain behavior to be determined at the high strain rates that are generated in the expanding ring test; however, there appears to be little quantitative data published in the literature on stress strain curves (see Satapathy and Landen, 2005, for a recent application). Altynova et al. (1996) followed the experimental arrangement of Gourdin, but without the VISAR and investigated the failure strain and fragmentation statistics; they "confirmed" the increase in ductility of OFHC copper and Al 6061.

The summary presented above is about the total extent (save a few variants that describe tests on different materials) of experimental results available in the literature on the expanding ring experiment. In contrast, there is a vast literature on analytical and numerical simulations, most attempting to explain the occurrence of multiple necking and fragmentation. The original analysis of Mott (1947), based on two simple postulates, merits summary at this stage since it is our opinion that Mott captured the essence of the phenomenon of fragmentation accurately. Mott first postulated that, unlike the strength of brittle materials that is dominated by the presence of Griffith flaws, necking and fracture in ductile materials would be governed by the dispersion in the fracture strain in a material at the limit of its ductility; there is then a probability density function,  $p(\epsilon_f)$ , associated with the failure strain that is usually not well characterized in experiments. In this model, each material point in the ring continues to accumulate plastic strain until it reaches its failure strain unless it is unloaded. This brings up the second postulate: once a fracture appears at the weakest link, this generates a release wave that travels down the ring unloading regions encompassed by the release waves; since prior to fracture all material points in the ring possessed only a radial velocity, the release wave has to provide the tangential velocity for material points that are within the released region. This requirement slows down the progress of the release wave quickly. Mott estimated the speed of this wave assuming that the material was perfectly plastic and that the released region moved as a rigid body. The region that is unloaded by the release wave cannot sustain further strain or fracture while other regions continue to experience radial expansion and hence are susceptible to fracture. This competition between the propagation of the release wave and the continued straining over the range of the failure strain distribution dictates the length of the fragments in the Mott theory. Kipp and Grady (1985) and Grady and Olsen (2003) have pursued the statistical theory of Mott further with appropriate accounting for the time scale associated with the fracture process.

In addition to this line of models based on the statistical distribution of the failure strain, there have been numerous analyses based on perturbation models (Fyfe and Rajendran, 1980, Fressengeas and Molinari, 1994, Shenoy and Freund, 1999, Guduru and Freund, 2002, Mercier and Molinari, 2003, Triantafyllidis and Waldenmayer, 2004, and Zhou et al. 2006). The idea behind these perturbation analyses is the following: first, the continuity and momentum balance equations governing the uniform extension of a specimen are written down; these have to be completed with the appropriate constitutive description incorporating strain hardening, strain rate dependence, thermal softening etc. Clearly, uniform radial expansion of the ring specimen (or an equivalent deformation projected on to a straight rod) can be written down as the homogeneous solution to this problem. Second, a small periodic perturbation in the uniformity is superposed on the homogeneous solution; the governing equations are then linearized about the homogeneous state to obtain the equations governing the evolution of the perturbations. Imposing the requirement of nontrivial, nondecaying perturbations yields the conditions for growth of the perturbations as a function of the wavelength as well as the growth rates. The dominant perturbation is then selected as the one with the fastest growth rate. From all of these perturbation

analyses, a common feature emerges that long wavelengths and short wavelengths are both filtered out – by inertia or viscosity – and some intermediate wavelengths dominate; this wavelength is taken to dictate the size scale of the necks and fragments. Interestingly, almost all of the perturbation analyses appear to mimic reasonably well the dependence of the number of fragments on the expansion velocity that was measured by Grady and Benson (1983). In other words, one is unable to discriminate the effect of strain hardening, strain-rate hardening and thermal softening on fragmentation in the absence of more detailed comparison with experimental results.

Direct numerical simulations have also been performed to examine the expanding ring experiment. Han and Tvergaard (1994) performed a finite element analysis of the ring expansion experiment with a piecewise power law function describing the material model for strain hardening plasticity. Multiple neck generation was demonstrated successfully in these simulations; small initial imperfections were found to grow into necks. Furthermore, the imperfections introduced in the simulations had a significant influence on the number and position where the necks occurred. Pandolfi et al. (1999) performed a similar numerical simulation, but with strain hardening, strain-rate dependence, and thermal softening modeled completely; in addition, fracture was simulated with a cohesive surface model. They show a comparison of the predicted number of necks and fragments with the observations of Grady and Benson (1983) and the results appear to be in good correlation. Even more recently, Guduru and Freund (2002) performed a full numerical simulation of a strain hardening material, with a modified Gurson model for capturing void formation and eventual fracture. Becker (2002) also simulated fragmentation in a U-6%Nb alloy with a Gurson type model and obtained good prediction of the number of fragments. These simulations overestimated the actual number of necks, but predicted the number of fragments reasonably well.

In summary, the two different approaches to the analysis of the necking and fragmentation problem – the statistical theory and the perturbation theory – end up with similar predictions. While the scatter in the observed results of Grady and Benson (1983) is easily handled within the Mott postulate of statistical variation in the failure strain of the material, the mean value of the observed fragment number is compared with the prediction of the perturbation analyses. Which theory is appropriate for determination of the fragmentation behavior of the material? Our aim in this paper is to provide significant additional experimental observations that will clearly identify the time sequence of the onset and growth of necks and fragments and thereby provide the appropriate physical underpinnings for modeling necking and fragmentation.

In Section 2, the experimental arrangement of the expanding ring experiment is described, along with a summary of the appropriate electromagnetic analysis of the force generation. Experimental observations of the time evolution of homogeneous expansion, neck generation, and fracture of the ring at different expanding speeds are described in Section 3. These real-time observations provide direct experimental confirmation of the sequence of events postulated by Mott with regard to the fragmentation of shell cases. Analytical, numerical and statistical evaluation of these and other experimental observations on Al 6061-O are presented in Section 4. The major conclusions of the present study are summarized in Section 5.

## **2. Experimental Arrangement**

The details of the experimental investigation are provided here. The present investigation represents the first implementation of this arrangement where high-resolution, high-speed images have been acquired indicating the development of necking and fragmentation. We describe the experiment in great detail so that the results could be interpreted easily and the arrangement may be duplicated by other investigators.

### **2.1. The Expanding Ring Experiment**

The principle of electromagnetic loading for the expanding ring experiment is quite simple. The specimen is in the form of a thin circular ring of radius  $r_0$  and cross sectional dimensions  $t$  and  $h$ , both typically significantly small in comparison to  $r_0$ . This ring is inserted over a solenoid of  $n$  turns wound without pitch on a mandrel. A schematic diagram of such an apparatus is shown in Fig 1. A close-up photograph of the experimental arrangement is shown in Fig. 2; details of construction of the solenoid are described later in this section. When a current,  $I_1$ , flows through the coil, an induced current,  $I_2$  develops in the specimen, the interaction between these generates a repulsive force between the solenoid and the ring specimen. As a result, the ring is accelerated to expand radially to speeds in the range of 80 to 200 m/s. The current in the coil is generated by discharging a 20 kV, 25  $\mu$ F capacitor. Switching of the high current is accomplished by firing a thyatron-ignitron circuit that also allows for easy synchronization of the loading with recording systems. The current in the solenoid and the ring specimen are measured with two Rogowski coils as suggested by Gourdin (1989); one Rogowski coil loops around the line that connects to the solenoid while the other Rogowski coil loops around all turns of the solenoid and the specimen ring as indicated in the schematic diagram in Fig. 1. Thus the first Rogowski coil measures the current  $I_1$ , while the second Rogowski coil measures the sum of the current in the specimen ring and the  $n$  turns of the solenoid:  $I_1 + nI_2$ . The Rogowski coil probes were fabricated in-house and calibrated by discharging a known voltage from a single capacitor-inductor circuit.

The solenoid-ring system can be considered as two equivalent  $RLC$  circuits: a second-order main circuit that contains the capacitor and the solenoid, and a simple circuit that contains the expanding ring specimen. For the main circuit, Kirchhoff's voltage law yields

$$\begin{aligned} C \frac{dV}{dt} &= I_1 \\ V + R_1 I_1 + L_{11} \frac{dI_1}{dt} + \frac{d(L_{12} I_2)}{dt} &= 0 \end{aligned} \quad (1)$$

where  $C$  is the capacitance,  $R_1$  is the resistance of the solenoid circuit,  $L_{11}$  is the self-inductance of the solenoid,  $L_{12}$  is the mutual inductance between the solenoid and the ring specimen,  $V$  is the applied voltage and  $I_1$  and  $I_2$  are the currents in the solenoid and ring respectively. For the expanding ring specimen we have

$$R_2 I_2 + \frac{d(L_{22} I_2)}{dt} + \frac{d(L_{12} I_1)}{dt} = 0 \quad (2)$$

where  $R_2$  is the resistance of the ring, and  $L_{22}$  is the self-inductance of the ring. Expanding Eqs. (1) and (2) and introducing the fact that the  $L_{12}$  and  $L_{22}$  are functions of the instantaneous radius of the expanding ring  $r(t)$ , we get

$$\ddot{I}_1 = -\frac{R_1}{L_{11}} \dot{I}_1 - \frac{L_{12}}{L_{11}} \ddot{I}_2 - \frac{2\dot{I}_2 \dot{r} + I_2 \ddot{r}}{L_{11}} \frac{dL_{12}}{dr} - \frac{I_2 \dot{r}^2}{L_{11}} \frac{d^2 L_{12}}{dr^2} - \frac{I_1}{L_{11} C} \quad (3)$$

and

$$\dot{I}_2 = -\frac{R_2}{L_{22}} I_2 - \frac{L_{12}}{L_{22}} \dot{I}_1 - \frac{I_1 \dot{r}}{L_{22}} \frac{dL_{12}}{dr} - \frac{I_2 \dot{r}}{L_{22}} \frac{dL_{22}}{dr} \quad (4)$$

The self-inductance of the ring specimen is (AIP, 1972)

$$L_{22} \approx 4\pi r \left[ \left( 1 + \frac{r_w^2}{8r^2} \right) \ln \frac{8r}{r_w} + \frac{r_w^2}{24r^2} - \frac{7}{4} \right] \times 10^{-7} \approx 4\pi r \left[ \ln \frac{8r}{r_w} - \frac{7}{4} \right] \times 10^{-7} \quad (5)$$

where,  $r_w = \sqrt{A/\pi}$  is the area-equivalent cross-section radius of the ring. In the expanding ring test, since  $r_w/r < 10$ , the second order terms of  $r_w/r$  can be ignored in the above equation, resulting in the approximation indicated.

The mutual inductance of the solenoid and the specimen can be calculated from (Jackson, 1975)

$$L_{12} = 2\mu_0 \sum_{i=1}^N \frac{\sqrt{r_i r}}{k} \left[ \left( 1 - \frac{k^2}{2} \right) K(k) - E(k) \right] \quad (6)$$

where  $k = \sqrt{\frac{4r_i r}{(r_i + r)^2 + z_i^2}}$ ,  $K(k) = \int_0^{\pi/2} \frac{d\theta}{\sqrt{1 - k^2 \sin^2 \theta}}$ ,  $E(k) = \int_0^{\pi/2} \sqrt{1 - k^2 \sin^2 \theta} d\theta$ ,  $r_i$  is

the radius of the coil loop  $i$  and  $z_i$  is the spatial distance between the coil plane and the ring plane. The mutual interaction between the currents in the solenoid and the ring results in the ring expanding radially; the equation of motion for the ring can be obtained from energy considerations. The total energy of the system is:

$$W = \frac{1}{2} CV^2 + \int_0^t (R_1 I_1^2 + R_2 I_2^2) dt + \frac{1}{2} \sum_{i=1}^2 \sum_{j=1}^2 L_{ij} I_i I_j + \frac{1}{2} M \dot{r}^2 + \int_0^t 2\pi A \dot{r} \sigma(\epsilon) dt \quad (7)$$

where the first term is the energy stored in the capacitor, the second term represents the dissipation in the resistors, the third term is the inertia of the inductors ( $i, j$  refer to the two equivalent circuits), the fourth term is the kinetic energy of the expanding ring (assuming the solenoid is rigid) and the last term is the mechanical work done on the specimen.  $M$  is the mass of the ring specimen,  $A$  and  $r$  are the cross-section area and the mean radius of the ring,  $\rho$  is the mass density of the specimen, and  $\sigma(\epsilon)$  is the constitutive law for the material of the ring. Balancing the rates of exchange of these energies (setting  $dW = 0$ ), and introducing Eqs. (3) and (4), the acceleration of the expanding ring can be obtained as:

$$\ddot{r} = \frac{I_1 I_2}{2\pi A \rho} \frac{dL_{12}}{dr} + \frac{I_2^2}{4\pi A \rho} \frac{dL_{22}}{dr} - \frac{\sigma}{\rho r} \quad (8)$$

For a given constitutive model, Eqs.(3 to 6) and Eq.(8) must be solved simultaneously to determine the ring expansion. While  $dL_{22}/dt$  can be calculated easily from Eq. (5), calculation of  $dL_{12}/dt$  from Eq.(6) is more difficult. This latter calculation is simplified by considering the

magnetic induction  $b(r)$  produced by the solenoid where  $2\pi r b(r) = dL_{12}/dt$ . Consider the solenoid as a stack of circular rings with identical radius and in planes parallel to the specimen ring; the magnetic field at position  $r$  can be calculated by the Biot-Savart law. The axial and radial components of the field produced by the coil loop  $i$  are found to be (Jackson, 1975):

$$b_i^z(r) = \frac{\mu_0}{2\pi} \int_0^\pi \frac{r_i^2 - r_i r \cos \theta}{(r^2 - 2rr_i \cos \theta + r_i^2 + z_i^2)^{3/2}} d\theta \quad (9)$$

$$b_i^r(r) = \frac{\mu_0}{2\pi} r z_i \int_0^\pi \frac{1}{(r^2 - 2rr_i \cos \theta + r_i^2 + z_i^2)^{3/2}} d\theta \quad (10)$$

where  $r_i$  and  $z_i$  as defined earlier. It is easy to show that the resulting axial component of the magnetic field  $b^r(r) = 0$  for all loops due to symmetry when the specimen is placed in the middle plane of the solenoid. The resulting radial component of the magnetic field is

$$\frac{1}{2\pi r} \frac{dL_{12}}{dr} = b(r) = \sum_{\text{Loop } i} b_i^z(r) = \frac{\mu_0}{2\pi} \sum_{\text{Loop } i} \int_0^\pi \frac{r_i^2 - r_i r \cos \theta}{(r^2 - 2rr_i \cos \theta + r_i^2 + z_i^2)^{3/2}} d\theta \quad (11)$$

The above expression is used in Eq.(8) to calculate the  $dL_{12}/dt$ . If Joule heating and plastic work effects are significant, the temperature of the specimen can change significantly and hence the heat balance equation may need to be incorporated into the formulation as well. Since the whole process of the ring expansion until failure typically occurs within several tens of microseconds, an adiabatic condition can be assumed. Then, the rate of temperature change is

$$\dot{T}_s = \frac{R_2 I_2^2}{2\pi A C_p \rho} + \frac{\sigma \dot{\epsilon}_p}{C_p \rho} \quad (12)$$

where  $C_p$  is the specimen specific heat, and  $\dot{\epsilon}_p$  is the plastic strain rate in the specimen. Since the specimen strains to about 25 to 45% in these experiments, we may neglect the elastic strains and approximate the plastic strain rate as  $\dot{\epsilon}_p = \dot{r}/r$ . In our initial simulations we have taken the constitutive response of the specimen to be independent of strain-rate and temperature. The system of equations (3) to (6), (8), (11) and (12) can now be solved numerically to calculate the ring expansion history for a given constitutive model. Such solutions may be used to optimize the design of the expanding ring experiment and to interpret the experimental measurements. In the following, we discuss the effect of the number of windings and the symmetry of the windings on the forces generated on the specimen.

Niordson (1965), Gourdin (1989), and Altynova et al (1995) used different number of windings in the solenoids to drive the expanding rings. Here we discuss the effect of the winding numbers on the magnetic field and also the symmetry and stability of the expanding ring, and provide a rational basis for the selection of the driving solenoid. First, for an efficient expanding

ring set up, the magnetic field produced by the solenoid needs to be maximized for a given input current. Consider the  $z$  variation of the magnetic field of an individual coil with a fixed ratio of  $r/r_i = 1.158$  (close to our experimental setup). The resulting magnetic field  $b^z$  and  $b^r$  are plotted in Fig. 3. It is found that a sign change of  $b^z$  exists when  $z$  increases monotonically from 0 where the planes of the specimen and the coil overlap. In this calculation,  $b^z$  with a negative sign (corresponding to  $z/r_i < 0.37$ ) tends to expand the ring specimen when current is induced in the specimen; in contrast,  $b^z$  with a positive sign (corresponding to  $z/r_i > 0.37$ ) tends to shrink the ring specimen. Note that after the sign change, the magnitude of  $b^z$  is small, approaching zero with increase of  $z$ . This means that the effect of coils at planes farther than  $0.37 r_i$  from the specimen plane is small and only slightly decreases the effective magnetic field intensity that expands the ring specimen. Therefore, a coil with an aspect ratio ( $h/2r_i$ ) around 0.37 is best for maximizing the magnetic field for the specific  $r/r_i$  ratio considered. In this study, since a 16-gauge square cross-section magnet copper wire was used for winding solenoid with turn radius of 13.38 mm and turn spacing of 2.54 mm, the optimum aspect ratio of 0.37 results in a width of 10 mm of the solenoid turns which corresponds to approximately 5 turns.

The magnetic field coefficients,  $b^z$  and  $b^r$ , around the solenoid are plotted as a function of position  $z$  at different radius  $r$  (see Fig. 4 for a six turn coil).  $b^z$  exhibits a larger value at the middle of the solenoid with a superposed oscillating variation. The oscillations are more apparent when  $r$  is small, i.e., when the ring specimen does not expand significantly. Repeating these calculations with seven and eight turn coils, we found that the middle plane of an odd-turn solenoid corresponds to a peak of  $b^z$ , while the middle plane of an even-turn solenoid corresponds to a valley of  $b^z$ . On the other hand,  $b^r$  increases monotonically with position  $z$ , with a superposed oscillatory variation; the sign changes in the middle plane of the solenoid. As a result, initially, when  $r$  is small, the middle plane of an odd-turn solenoid corresponds to a linearly increasing portion of  $b^r$ , while the middle plane of an even-turn solenoid corresponds to a flat portion of  $b^r$  (see Fig. 4 inset for an enlarged view of the region near the middle plane). Thus, an even number of turns is advantageous since for any misalignment in either the radial or axial directions, the magnetic fields force the specimen towards the location of symmetry thus ensuring uniform ring expansion.

Finally, it worth to point out that the mutual inductance between the solenoid coils and the ring specimen also affects the efficiency of the solenoid-ring system. According to Eq. (12), a larger winding number of the solenoid gives a greater mutual inductance, and thus a higher induced current and expansion radial force in the ring specimen. This effect dominates the expanding speed of the ring but is compromised by the negative driving force generated by turns farther away from the ring plane. It is found through calculations, that the expanding speed of the ring saturates for more than 8 windings. In our experimental setup, 6-turns solenoid was used for achieving a reasonably high driving efficiency.

## 2.2. High Speed Photography

The expansion of the ring was photographed with a high-speed camera that has a combined framing and streak imaging capability that was quite useful in the present investigation. Since both features of the camera were essential in interpreting the images obtained, we describe the working principle of the camera in some detail. The rotating-mirror, stationary film type high speed camera was designed and built in our laboratory. A cavity-dumped Argon ion laser was used in a pulsed mode to illuminate the expanding ring in a shadow mode, with the coil and the ring blocking the light path as indicated in Fig. 5. This light beam is collected by a system of



lenses and directed towards a mirror, oriented at  $45^\circ$  with respect to the optical axis and mounted on an air-turbine capable of rotating at about 40,000 rpm. The mirror deflects the image into a direction perpendicular to the optical axis and an image of the object plane is generated on a film track mounted on a cylindrical drum coaxial with the optical axis. The film itself is held stationary in this drum. As the turbine rotates, the image streaks along the film plane continuously; discrete images are formed on the film only when the laser is pulsed to give a burst of light with a 15 ns duration. The duration of the flash is short enough to freeze all motion and provide a high-resolution image that corresponds to the light pulse. These 15 ns burst of light pulses are provided every 11  $\mu\text{s}$  apart, sufficient time for the image to move to a fresh spot on the film, adjacent to the previously captured image. Laser light pulses are terminated after one complete revolution of the turbine to prevent multiple exposures on the film. A total of 120 pulses are sent to the laser, acquiring 120 images of the event of interest. The laser pulses are triggered first, and after about 60  $\mu\text{s}$ , the trigger signal to start the expanding ring loading is provided, thus ensuring the capture of the complete ring expansion, necking and fragmentation. In this arrangement, a capping shutter is opened prior to supplying the first laser pulse and closed after the last laser pulse; there is no shuttering between images leaving the film plane wide open during one revolution of the turbine. This results in the possible formation of an interesting streak image as we discovered during this investigation. In the absence of any light, no images are formed on the film (the room is darkened to minimize ambient light effects); however, if there is a light spark at a point in the specimen – as happens during an expanding ring experiment when an arc discharges across a fragment – then the light from this spark will be deposited on the film. Since the image moves continuously on the film plane, the image of the spark will appear as a streak on the film plane for as long as the spark exists; furthermore, if we consider the spark to begin as a point light source and then grow spherically, the trace of this growth will be recorded by the streak! Thus, while Niordson (1965) was able to obtain one still image with all sparks superposed, we are able to get time resolution of the different sparks that occur during fragmentation, providing the sequencing of the fragmentation events.

### 3. Experimental Observations on Dynamic Necking and Fragmentation

We describe four experiments in Al 6060-O specimens in detail in order to facilitate interpretation of the results and the subsequent modeling; a listing of all nine experiments performed in this study is given in Table 1. The dimensions of rings are as follows: 15.5 mm mean radius, 0.5 mm thick and 1 mm long. The time variation of the current supplied to the coil and the induced current in the specimens, both measured with Rogowski coils, are shown for Specimens A, B, C, and D in Fig. 6. The current supplied to the solenoid oscillates sinusoidally with an exponential decay; however, the expanding ring breaks up within the first period of this oscillation. The peak magnitude of the current is on the order 20 kA. The current induced in the expanding ring also reaches about 20 kA in about 10  $\mu\text{s}$ , thus driving the ring to expand rapidly. An abrupt change of slope in the specimen current is observed at some time between 40 and 60  $\mu\text{s}$ ; we identify from high speed images that this corresponds to the first fracture in the ring. We note that a variable phase difference develops between the currents in the solenoid and the expanding ring with the current reversing beyond about 20  $\mu\text{s}$ ; this response is different from that observed by Gourdin (1989) and may be of potential interest in generating a soft recovery or tailoring the expansion speed profile.

High speed images were obtained at 11  $\mu\text{s}$  intervals, with the precise times identified by the trigger signals sent to the solenoid as well as the pulsed laser that creates the images. The sequence of images from one experiment (Specimen D; charge voltage 8 kV) is shown in Fig. 7; the entire segment of the filmstrip corresponding to the time from the beginning of the current to the next 110  $\mu\text{s}$  was digitized continuously to display the discrete frames as well as the streak image. Movies of this experiment and other similar experiments are available at the website:

<http://www.abc.def>. The central dark circle which is the shadow of the coil used to drive the expanding ring and the current lead feeding this coil are identified in the first frame in the figure. The ring is initially at the periphery of this dark circle; upon discharge of the current pulse through the coil, the ring expands and this expansion can be seen in the subsequent images. It is to be noted that even though the electromagnetic field has a slight break in the symmetry due to the jog in the windings, the expansion over the first 40  $\mu\text{s}$  is axisymmetric. Beyond 40  $\mu\text{s}$ , the appearance of the fractures, the development of fragments, and the rigid motion of the fragments can be seen in Fig. 7. It is clear that the statistics of fragmentation can be determined from these images.

The first fracture occurs while a high current is still circulating in the specimen ring and as a result, an arc discharge occurs at the break point. This arc begins as a point source, grows with time and leaves a streak on the film plane, as described earlier. Therefore, even though the fracture may have occurred in between two discrete frames captured by the high speed camera, the spark and its trail clearly mark the time of the fracture event<sup>3</sup>. The second and third fractures also occur while the current persists in the ring through the plasma of the first arc and hence these also leave a streak on the film plane. These arcing points are identified in the filmstrip as occurring between the 4<sup>th</sup> and 5<sup>th</sup> images in Fig. 7. Since the translation speed of the image on the film plane is known, the precise timing of the three breaks relative to the beginning of loading is easily worked out. The arc discharges also induce a shock wave in air and these can be seen to expand out from the fracture points in the discrete frames in Fig. 7. These also aid in identifying the sequence of the first three fracture points. By the time the remaining fractures occur, the circulating current drops off to lower levels that no further discharges are seen, even though the plasma generated at the first three breaks appears to persist for about 10  $\mu\text{s}$  (estimated from the length of the light streaks). All but the last of the fractures had occurred by the 6<sup>th</sup> frame in the sequence shown in Fig. 7, revealing that the total time for the fragmentation process was less than about 20  $\mu\text{s}$ . Similar images were obtained from 9 specimens of Al 6061-O by repeating these experiments at the same expansion rate and for different expansion rates for enabling statistical analysis of fragmentation.

The radius of the ring as a function of time was measured from the high speed images for all tests; the variation of the radius as a function of time for Specimens A-D is shown in Fig. 8. The expanding velocity, obtained by differentiating the position data, is also shown in this figure. It is evident that the ring accelerates rapidly to speeds in the range of 100 to 250 m/s and then decreases gradually as the current dwindles and the ring gets away from the coil, dissipating its energy through plastic straining of the specimen; the strain rate  $\dot{\epsilon} = \dot{r}/r$  is then estimated to be in the range of  $5 \times 10^3 \text{ s}^{-1}$  to  $1.3 \times 10^4 \text{ s}^{-1}$ .

The most important results of this particular series of experiments are contained in the information that the high speed photographs reveal at high magnifications – complete spatio-temporal details about the onset of necking and fragmentation are obtained by carefully examining the images in frames 4 through 6. An image of segments of the ring taken from the 5<sup>th</sup> frame of Fig. 7 is shown in Fig. 9 at high magnification. In addition to the first three breaks that were identified by the spark streaks (and which are clearly visible in the low magnification image in Fig. 7), 32 necks and 3 additional fractures in various stages of development are visible in the mosaic in Fig. 9. These evolve further and eventually a total of 14 fragments and 38 necks were observed in the images. All neck positions are identified in the figure; in addition, necks that grew into fractures are identified by circles around the numbers.

The time evolution of the necks and fractures can be visualized more clearly by generating a composite image from the high speed sequence. From each image, all parts of the image except

---

<sup>3</sup> The streak from the arc discharge can be analyzed using the similarity rule established by Taylor for expansion of a blast waves from an explosion; this is discussed in the Appendix.

that occupied by the ring is removed, and the  $i^{\text{th}}$  image is stored as  $I_i(x, y)$ . Then the composite image is constructed by taking the sum of all such images:  $\sum I_i(x, y)$ ; since the ring expands at

high speeds, the ring does not occupy the same positions  $(x, y)$  in the different images, and hence we observe a spatially separated image of the expanding ring. We note that the arc-discharges and shock wave images will be eliminated in these composite images, but such data were used in identifying the sequence of events during fragmentation of the specimens. Figures 10-13 show composite images from three different tests on Al 6061-O performed with different imposed current levels (Specimens A, B, C, and D); the time variation of the currents in these specimens are shown in Figs. 6. The variation of the ring radius and expansion velocity is shown in Figs. 8. It is noted that the nominal expanding velocities in the three cases are about 80 m/s, 120 m/s, 150 m/s, and 200 m/s respectively. These data provide a simple way of identifying the deformation and fracture events and a number of important observations can be made from the composite images.

- Fig. 10 corresponds to 5 kV charge (Specimen A). The composite image is made by selecting specific frames (numbers identified in the figure) so as to spatially separate the ring images. The ring accelerates quickly to speed of  $\sim 80$  m/s and expands uniformly until  $\sim 40 \mu\text{s}$ .
- Following the uniform expansion, a number of necks develop at different locations. The nominal strain at this time is about 25 percent. At later times, nucleation of additional necks and subsequent growth of the necks into fractures at different locations are observed. The positions of all of the necks are identified in Fig. 10 by numbering them in spatial order, beginning at the location of the current lead and going counterclockwise.
- Quantitative data on the coordinates of the neck and the time range over which they appear are given in Table 2. Since multiple necks form in the time interval between two images, we are unable to identify the precise time sequence of the formation of each neck, but can clearly identify the time range over which all such necks form. Therefore, from the high speed images we can identify the strain range over which necks are nucleated in all the tests and will discuss this quantitatively in the next section.
- The first few fractures always result in arc discharges and the attendant shock waves; these features were used to identify the time of onset of the first few fractures. For the later fractures, we follow the tangential separation of the fracture points as the ring expands, and extrapolate to the time at which the fracture must have occurred. This turns out to be a conservative estimate as we explain later and the fracture actually occurs earlier than the time identified by this technique. With this technique, we estimate that the time of onset of fracture for each fracture point in all experiments. The locations of the fractures are identified in the Fig. 10 in the exact order of appearance and the time and order of fractures are listed in Table 2.
- The necks can be used as markers of position in the specimen during further expansion. If the positions of the necks in subsequent images are connected as shown by the dotted white lines in Figs. 10-13, we see the trace of the movement of these points. From such traces, we can estimate the tangential component of particle velocity and therefore examine the progression of the release wave from either the necking process itself or the neighboring fractures.
- All fractures are complete in less than  $20 \mu\text{s}$ . Beyond this time, the fragments move almost as a rigid body (except for small deformations associated with residual strain energy in the fragments) and are deposited on a soft clay layer. The fragments were recovered for later analysis.
- Specimens B, C, and D exhibited a similar sequence of events, with the only difference being in the expansion speed, and hence in the number of necks and fragments. The exact sequence

of the fragmentation is indicated in Figs. 11, 12, and 13; the position and time corresponding to the nucleation of necks and fractures are listed in Tables 3, 4, and 5.

- While the overall deformation appears to be quite symmetric in the early stages when the necks and fractures first develop, for the experiments with the lower expansion speeds, we observe in Figs. 10 and 11, flexural deformations that develop at later times. Corresponding to these, additional fractures that appear at much later times that do not correspond to the uniform expansion (for example, neck 15 of Specimen A in Fig. 10 developed to fracture in later frames which are not showing in this figure)
- Tumbling of the fragments is seen (marked in Fig. 11) indicating that the neck growth process has introduced torsional moments on the ring fragments.
- The size distribution of the fragments may be analyzed in a couple of different ways; first, the high speed photographs can be analyzed quantitatively to determine the lengths of the fragments. Alternatively, one could simply weigh the recovered fragments as in the work of Grady and Benson (1983). Statistical analysis based on the lengths of the fragments determined from these and other tests on Al 6061-O is discussed in the next section.
- Finally, some of the very short fragments correspond to adjacent fracture events that occurred at extremely close time intervals (such as fragment VIII of specimen C in Fig. 12) and hence independently of each other.

#### 4. Interpretation of Dynamic Necking and Fragmentation

We now turn to analysis and interpretation of the experimental results in terms of the electromagnetic loading described in Section 2 and the kinematic observations in Section 3. First, we restrict attention to the early part of the experiment, prior to the onset of necking; in this range, the experiment may be analyzed with a model of strain hardening plasticity, with the possible inclusion of thermal softening. Next, we examine the experimental results in light of the perturbation analyses reported in the literature and extract some conclusions on the onset of the necking instability. This is followed by a simple statistical interpretation of the fragmentation process, along with a comparison with the Mott theory of fragmentation. This process of fragmentation is evaluated through a numerical simulation of the unloading that results from fracture; the diffusion of radial momentum to tangential momentum suggested by Mott (1947) is shown to capture the essence of the fragmentation behavior. Finally, we explore the strain at the onset of necking in the different experiments and the strain at final failure; the issue of enhanced ductility under high strain rates is addressed.

##### 4.1. Uniform Expansion of the Ring

The quasi-static material response of the Al 6061-O was characterized in a tensile test in order to provide base-line material properties. Standard dog-bone shaped tensile test specimens (in compliance with ASTM standards E8M-04) were machined from the same tubes from which the expanding ring specimens were cut. The curved surfaces were then machined to yield a rectangular cross section with an aspect ratio of 2, matching that of the expanding ring specimen. The tests were performed in an Instron test machine, with an extensometer rated to 50% strain over a 1 inch gage length. The true-stress vs logarithmic strain variation is shown in Fig. 14. With the constitutive response of the Al 6061-O taken to be a power law of the form

$$\sigma = \sigma_y (1 + \beta \epsilon_p)^n \quad (13)$$

the material parameters were obtained by fitting to the experimental response:  $\beta = 14165$ ,  $n = 0.22$ , and  $\sigma_y = 25$  MPa. Localization in the form of a neck was observed in these uniaxial

tests at the load maximum. The strain at the onset of localization was found by averaging two tests to be:  $\epsilon_N^{qs} = 0.22$ .

Prior to the onset of the first neck, the expanding ring experiment can be analyzed quite easily because the strains develop uniformly in the ring. The differential equations governing the electromagnetic loading, the ring acceleration, and the thermal history are given in Eqs. (3) to (6), (8), and (11-13). Rather than calculating the current,  $I_1$ , in the primary solenoid circuit, the current measured with the Rogowski coil is used as input and the time variation of the current induced in the specimen,  $I_2$ , the ring radius,  $r(t)$ , and temperature,  $T(t)$ , are then estimated by solving the governing equations with a fourth-order Runge-Kutta integrator. All material properties used in obtaining solutions to the above equations are given in Table 6. The current,  $I_2$ , calculated from this scheme is compared with the current measured with the Rogowski coil in Fig. 6 for Specimens *A* to *D*. The calculated current matches the experimental measurement quite well for about the first 20  $\mu$ s, but shows a small deviation at later times. The reason for this departure is not evident at this stage, but we will discuss this issue later. The calculated time variation of the radius of the ring is compared to the experimental measurement in Fig. 8; very good agreement can be observed. The calculated temperature increase for all four specimens is shown in Fig. 15; the temperature increases to the range of 300 to 400 °C in about 40  $\mu$ s. Thus, while thermal softening may be ignored in the first 20  $\mu$ s, it may play a role for longer times. In order to estimate this, a modified form of the Johnson-Cook model was used instead of Eq. (13):

$$\sigma = \sigma_y (1 + \beta \epsilon_p)^n \left[ 1 - \left( \frac{T - T_0}{T_m - T_0} \right)^m \right] \quad (14)$$

$m = 1.34$ ,  $T_0$  is the room temperature and  $T_m$  is the melting temperature for the specimen. We note that the material model used here does not impose strain rate effects. The estimated current was not affected significantly as to be visible in the trace shown in Fig. 6 and the ring position estimate was influenced by a small amount for Specimen *D* as shown in Fig. 8. Strain rate effects may be important, although we do not pursue this quantitatively at this stage due to lack of a proper constitutive model appropriate to the nearly-adiabatic conditions that the specimen encounters in the expanding ring test. Satapathy and Landen (2006) have recently pursued the idea of using this uniform expansion stage of the ring expansion experiment for constitutive characterization under adiabatic loading conditions. Thus, if the objective is to determine the constitutive properties of the material, analysis of the ring expansion experiment indicated in Section 2, with suitable accounting for the thermal softening and possible strain-rate effects in the material should suffice. This scheme is quite simple and can be accomplished in most laboratories since all that is required is a high-voltage capacitor-inductor circuitry and high-current high-speed switches to perform the loading and high-speed oscilloscopes to acquire the data; the total cost would be significantly lower than standard universal testing machines and the strain rates achieved can be as high as  $10^4 \text{ s}^{-1}$ .

The duration of uniform straining is followed by the development of necks. The statistics of neck development is examined in the next section.

#### 4.2. Onset of Necking Localization

We now examine the onset of necking localization from the collection of data in nine expanding ring experiments performed at different strain rates (see Tables 1 to 5). Typically the theoretical predictions based on linear stability analyses have been compared to the experimental results of Grady and Benson (1983) only through a counting of the total number of necks and/or fragments

and the estimated total fracture strain. However, we believe that this comparison is inappropriate since the spacing between necks varies over quite a large range. In the present experiments, we are able to generate much more detailed quantitative data thus facilitating comparison with analysis: specifically, we examine the distribution of lengths between necks in this section. From the positions of the necks indicated in Tables 2 to 5 and from similar measurements in the other experiments, the distance between necks was calculated. Thus, the  $n^{\text{th}}$  segment is of length  $l_{neck}^n = r_N (\theta^{n+1} - \theta^n)$ , where  $r_N$  is the radius of the ring at appearance of the necks; we note that this is the distance in the current configuration. Figure 16 shows the distribution of  $l_{neck}$  for necks observed in all of the tests, grouped by the ring expansion rate. Interpretation of this distribution can be attempted in a couple of different ways, based either on the predictions of the perturbation analysis or correlations based on the statistics of nucleation and the evolution of the loading. Both interpretations are pursued below.

As discussed briefly in the introduction, in the linear stability analyses, an initial homogeneous state is perturbed with a sinusoidal necked shape of different wavelengths and the growth rate of the neck is estimated by solving the equations of motion linearized about the initial state. Guduru and Freund (2002) considered an axisymmetric rod of length  $2L$  and radius  $r_w$ . Homogeneous deformation at a constant strain rate  $\dot{\epsilon} = \pi v_0 / L$  was imposed over the entire rod. The material was modeled as a hypoelastic material derived from Storen and Rice (1975). Perturbations in the axial and radial deformations of the rod, consistent with the incompressibility of the material, were imposed. The equations of motion linearized about the homogeneous state were examined to determine conditions under which these perturbations would continue to grow. Their results predict that corresponding to any particular strain level, there is a critical wavelength of the perturbation that exhibits maximum growth rate. However, there exists no criterion to select the strain level. Thus, they left the growth rate as a free parameter and determined the wavelength of the perturbation that maximized the growth rate corresponding to a specific strain or stress level. This wavelength may be taken as an estimate of the distance between necks. A simple manipulation of the results of Guduru and Freund (2002) yields the distance between necks at any velocity as:

$$\frac{l_{p1}}{r_0} = \frac{4\pi e^{\epsilon_1}}{\left(\frac{N_c \rho}{k}\right)^{1/4} \left[\frac{\pi v_0 L}{r_w}\right]^{1/2} - 1} \quad (15)$$

where  $v_0$  is the expanding ring speed,  $\rho$  is the density of the specimen,  $k$  is a constitutive parameter ( $\sigma = k\epsilon^n$ ),  $\epsilon_1$  is the strain at the onset of necking,  $r_w$  is the equivalent radius of the cross-section and  $N_c$  is the critical growth rate that is taken as a free parameter (in the range of 100 to 200 according to the estimates of Guduru and Freund, 2002). This estimate was evaluated quantitatively with the following parameters:  $N_c = 200$ ,  $k = 205$  MPa,  $r_0 = 15.5$  mm,  $r_w = 0.4$  mm,  $L = 2\pi r_0$ ,  $\rho = 2700$  kg/m<sup>3</sup> and for appropriate expanding speeds of the ring  $v_0$ .

In a more recent contribution, Zhou et al. (2006) addressed the same problem in a slightly different setting: these authors assumed a visco-plastic constitutive model and approximated the equations of motion assuming uniaxial conditions. Once again, the stability of perturbations from a homogeneous state corresponding to uniaxial extension with a strain  $\epsilon_1$  was considered. Using

the results of this analysis, and assuming a strain-rate independent power-law hardening material, we estimate the distance between the necks to be

$$\frac{l_{p2}}{r_0} = \frac{(r_w/r_0)e^{-1.5\varepsilon_1}}{2\sqrt{1-n/\varepsilon_1}} \quad (16)$$

Two interesting observations are made on the above estimate; first, it is clear that the Considère condition  $\varepsilon_1 \geq n$  must be satisfied in order to generate necks, but otherwise  $\varepsilon_1$  is not constrained by the analysis. Second, the distance between necks is independent of the strain rate; this is a result of ignoring radial inertia in the one-dimensional model. The predicted range of  $l_{p2}$  is very sensitive to the value of  $\varepsilon_1$ , particularly in the neighborhood of  $\varepsilon_1 \sim n$  and hence is not easily compared with the measured values of neck lengths.

It must be noted that these estimates of the distance between necks depend on the strain at which the necks appear. In comparing these to the experimental observations, we used the average strain level at which necks appeared in the quasi-static tests:  $\varepsilon_N^{qs}$ <sup>4</sup>. In order to compare the neck lengths from experiments at different expanding speeds, the observed lengths are normalized by  $l_{p1}$ . The distribution of the experimentally observed neck lengths  $l_{neck}/l_{p1}$  is shown in Fig. 17. These results indicate that the distance between necks is mostly in the interval  $0.2 \leq l_{neck}/l_{p1} \leq 2.6$  suggesting a very large deviation in neck lengths from the predictions of the perturbation analyses. Varying the free parameter  $N_c$  in the range 50 to 1000 did not affect the predicted values of  $l_{p1}$  significantly. It is clear that the wavelength identified by the perturbation analysis is quite far from the experimental measurement. However, it must be noted that the analysis merely indicates the possibility for necking deformations and cannot predict the correct wavelength of necking if significant changes in the loading occurred beyond the onset of necking. In fact, the largest unnecked segments are created in regions where the earliest fractures occurred. In these segments, the release wave from early fractures may have inhibited the development of further necks in this region; such unloading is not captured in the perturbation models. Therefore, instead of the perturbation based wavelengths, if we consider the characteristic unloading lengths, one may be able to collapse the observed distributions of neck lengths in the different experiments by normalizing with a modified Mott release wave estimate:

$$\frac{l_{MOTT}}{r_0} \propto \frac{\sqrt{k/\rho}}{v_0} e^{\varepsilon_1} \quad (17)$$

We will discuss this scaling after examining the statistics of necking.

Alternatively, we may analyze the onset and growth of necking through a combination of statistical and mechanical aspects. If we assume that the onset of necking is governed simply by the Considère criterion, then necks will appear beyond a critical strain level  $\varepsilon_N^{qs}$ , with the locations dictated by statistical variations in the critical strain at different points in the specimen. This variation may not be governed by geometrical imperfections since any initial geometric variations would have been eliminated as the ring expanded through to  $\varepsilon_N^{qs}$ , but by material variations at the microstructural level. Necks that nucleate at a lower strain level inhibit

<sup>4</sup> This assumption will be justified by the results discussed in Section 4.5.

nucleation of additional necks in a certain neighborhood dictated by the release wave speed, amplitude and the rate of strain in the neighborhood; hence we may expect  $l_{neck}$  to be governed by the statistics of distribution of necking strain *and* the release process. A general Weibull probability density function of the form

$$f_W(l_{neck}) = \frac{\kappa}{\lambda} \left( \frac{l_{neck} - l_0}{\lambda} \right)^{\kappa-1} \exp \left\{ - \left( \frac{l_{neck} - l_0}{\lambda} \right)^{\kappa} \right\} \quad (18)$$

was fitted to the measured lengths between necks  $l_{neck}$ . This distribution is plotted for each strain rate in Fig. 16. Two main trends are clear: first, the Weibull distribution fits the measured lengths rather well. Second, the Weibull fitting parameters indicate trends that can be interpreted in terms of the evolution of necking. For  $v \sim 80$  m/s we obtain  $l_0 = 1.5$  mm,  $\kappa = 1.9$ , and  $\lambda = 5.75$  and for  $v \sim 200$  m/s the corresponding values are  $l_0 = 0$ ,  $\kappa = 2.02$ , and  $\lambda = 3.95$ . The shape parameter remains nearly constant, at a value that corresponds approximately to the Rayleigh distribution, while the scale parameter decreases systematically. There is a clear tendency for  $l_{neck}$  to shift to smaller lengths as the ring expansion rate increases. We attribute this to the competition between continued straining from the loading and the propagation of unloading wave from necks formed earlier, rather than to intrinsic strain-rate dependence of the material. In the lower expansion rates, the release wave from necking unloads a larger segment while at higher expansion rate, unloading is minimal and more necks are nucleated closer together. A simple estimate of this may be obtained by doing a Mott scaling analysis: the maximum released length should scale as  $l_{max} \propto \sqrt{2\sigma_0 \Delta \epsilon / \rho \dot{\epsilon}^2}$ , where  $\Delta \epsilon$  is the range of strains over which necking appears. The distance between necks should then be about  $2l_{max}$ . If we take  $\sigma_0 = 150$  MPa,  $\rho = 2700$  kg/m<sup>3</sup>, and consider the variation in the strain at the onset of necking to be about  $\pm 2\%$  then we get the spacing between necks to be between 17 mm and 7 mm at the low and high strain rates; these estimates are within range of the measured distances between necks.

The two interpretations provided above are in fact somewhat complementary. The first interpretation based on linear stability analysis points to the existence of a critical strain at the onset of necking, and is therefore an extension of the Consid re criterion to the dynamic problems. However, the spacing between necks is influenced more by the statistical variations in the material properties – the necks occur at local weak points (with a distribution of the necking strain) that are randomly distributed along the circumference of the ring – and by the propagation of release waves than by the growth of the unstable wavelengths.

#### 4.3. Statistics of Fragmentation

Next, we turn to the distribution of fragment lengths. The length of each fragment is easily calculated from composite images of the type shown in Fig. 10; since the arc discharge erodes a small amount of the material, lengths of the segments immediately on either side of the first two or three fracture points would be underestimated. Furthermore, in segments that contain a large number of arrested necks, the fragment length is slightly larger than the equivalent homogeneously deformed segment. Nevertheless, we anticipate that this measure of the length of the fragments can be used as the basis for statistical evaluation of fragmentation. Alternatively, the mass of the fragments recovered may be used as an indicator of the fragmentation. Since we have direct access to the fragment length, our statistical analysis will be based on this measurement. Figure 18 shows the fragment length distribution from all nine of the tests



performed on Al 6061-O. In order to compare the fragment lengths from different expansion speeds, we normalize the fragment length with respect to a characteristic unloading length from the Mott release wave estimate:  $l_{MOTT} = \sqrt{2k/(\rho\gamma)}(r_0/v_0)e^{\epsilon_1}$ . The parameter  $\gamma$  in this expression is a measure of the dispersion in the failure strain assumed by Mott. Here, we simply take it as a fitting parameter to obtain the best fit to the distribution (evaluated to be  $\gamma = 107$ ). The data exhibited in Fig. 18 contains the lengths of about 132 fragments from expansion speeds in the range of 80 m/s to 200 m/s. A general Weibull probability density function was fitted to this data as indicated in Fig. 18. Perhaps a larger data set is needed to confirm the trends shown here; but the data set indicates that if the length of the fragment is normalized by the characteristic release length based on the Mott release wave propagation a Weibull distribution of the fragments can be a suitable representation. This suggests that a random distribution of weak points along the circumference of the ring, each breaking independently of the other, and that the release wave mechanism sets the scale for fragmentation.

#### 4.4. Fragmentation and Unloading Waves

The process of necking and fragmentation that we observe in the high speed images is exactly in accord with that outlined by Mott (1947). We now turn to a numerical simulation that can capture the essence of the fragmentation process – the “Mott release wave” – and provide a quantitative basis for the interpretation of the sequence of necks and fragments that were observed in the experiments. As the ring expands uniformly, the driving electromagnetic force provides all material points with a radial velocity; thus, at the instant of the first fracture (and nucleation of a neck), no material point has any tangential velocity component. However, after necking or fracture, the release of load at that point must travel along the expanding ring and provide a tangential velocity to the unloaded points. While the release wave, with initial amplitude equal to the yield stress of the material in the case of a fracture, propagates with the elastic wave speed, it is quickly robbed of its energy by conversion to tangential momentum. This conversion process changes the release event from wave propagation to one of momentum diffusion; Mott (1947) made a simple estimate for the propagation of the release wave by assuming that the material was rigid-plastic; this is equivalent to assuming that the fracture will send an unloading wave with an initial amplitude  $\sigma_0$  and the unloaded region will move as a rigid body. Mott found that the momentum diffusion is given by the expression  $x^2/t = 2\sigma_0 r / \rho \dot{r}$ , where  $x$  is the position at time  $t$  of the release wave relative to the fracture point,  $\sigma_0$  is the yield stress, and  $\rho$  is the mass density; Mott also assumed the strain rate  $\dot{\epsilon} = \dot{r}/r$  to be constant. Here, we examine the Mott wave generated by the unloading through a finite element simulation of the fragmentation process.

The geometry considered in the simulation is an axisymmetric rod; in the first loading step, one end of the rod is held fixed at  $x_2 = 0$  and extended with a speed that varies spatially as  $v(x_2, t) = \pi v_0 x_2$ ; this results in constant strain rate expansion of the rod that corresponds to a ring expanding radially at a speed  $v_0$ . When the strain in the bar reaches  $\epsilon_N^{qs}$ , the fixed end constraint is released for the second step in the simulation. Now, particle velocities are no longer imposed externally, but are determined by the kinetic energy at the break point and the continued plastic straining. This is very close to the experimental situation where the occurrence of the fracture terminates the current in the specimen and hence there is no further loading imposed on the specimen. The release of the constraint mimics the necking and fragmentation in the expanding ring and hence a “Mott release wave” travels down the length of the rod. The load steps are shown schematically in Fig. 19. In order to simulate possible time scales associated with the necking and fracture process, the end constraint was relaxed linearly over time  $\tau$  as indicated

in Fig. 19. The results of this simulation provide the time scale for the diffusion of momentum. The rod is taken to be elastic-plastic with the constitutive model described in Eq. (13); the finite element simulation was performed in ABAQUS Explicit Version 6.4; axisymmetric elements of type CAX4 were used. The length to diameter ratio of the simulation was 200 mm and the diameter was taken to be 0.5 mm.

The results of simulating the necking and fragmentation process are useful in interpreting the experimental observations. The time evolution of the normal stress component  $\sigma_{22}$  is shown in Fig. 20 for the second step of the loading indicated above. The high frequency disturbances seen in these simulations are the Pochhammer-Chree oscillations from the radial contractions. The bar, initially stressed to the yield stress is unloaded abruptly only at the ends; the release is clearly seen to diffuse through the bar at subsequent times. For example, 10  $\mu\text{s}$  after the beginning of the release, the unloading wave has fully unloaded only about 2 mm of the bar and the leading edge of the release wave has propagated about 10 mm. However, the elastic wave front has propagated about 50 mm in the same time (at a speed of  $\sqrt{E/\rho} \sim 5 \text{ mm}/\mu\text{s}$ ). Clearly, the elastic wave front does not unload the specimen, and the Mott release wave is quite slow in its progression. From the simulation, the position of the Mott release wave is determined as a function of time in Fig. 21 for the four different release processes. For comparison, Mott's rigid-plastic estimate is also shown in the figure; while quantitative differences appear at later times, qualitatively, the Mott estimate of the release wave diffusion appears to be quite reasonable.

Progression of unloading of the specimen is even more apparent if we look at the time history at a fixed point. In Fig. 22, the time variation of the stress and strain components  $\sigma_{22}$  and  $\epsilon_{22}$  at a point 10 mm from the release position are shown. The elastic wave arrives at this position at about 2  $\mu\text{s}$ , but is hardly noticeable in the stress or strain variation; the slower guided waves arrive at around 4  $\mu\text{s}$  and cause a small amplitude fluctuation of the stress, but with negligible impact on the continued straining of this point. One could guess that if these guided waves were to interact with necks formed earlier, it could result in growth and fracture of the neck; while this aspect has not yet been explored quantitatively in the simulations, experimental observations suggest that the necks neighboring a fracture point quickly get unloaded. At about 7  $\mu\text{s}$ , the Mott release wave arrives the material point and immediately begins to decrease the stress, but more importantly, drops the strain rate to almost zero. No further plastic straining is developed at this point. The displacement of the released point,  $u_2(x_2 = 0)$ , is plotted as a function of time for the different release profiles in Fig. 23. This point experiences a slow acceleration initially and builds up speed until it moves at about 100 m/s; the release time scale appears to have a very small influence on the motion of this point. This motion of the released point is to be compared with the separation between fragments in the expanding ring images shown in Figs. 10 to 13. As we pointed out in Section 3, by following the position of the fractured ends, we identified the time of onset of the fracture. From the slow acceleration indicated in the simulations, we can now substantiate the earlier claim that our estimate of the fracture initiation time was a conservative estimate; clearly the fracture must have occurred earlier than our estimates.

The above estimate of the Mott release wave can be used to interpret the experimental observations. The spatio-temporal trajectory of the Mott release wave from the first three fractures is identified in Figs. 10 to 13 by the color coded lines (red, green, and yellow line segments respectively). When the ring expansion speed is slow, the release waves from these breaks unload a large segment of the ring before the ring accumulates additional strain at other necks and in between necks. In contrast, in Figs. 12 and 13, segments of the ring away from the break points continue to strain at high rates and reach the local failure conditions before the slow release wave reaches these points. We can confirm that within the release zones, no further fractures are seen, and that the necks developed earlier get unloaded as the release wave arrives at these positions. Thus, the experimental results, together with the simulation of the release

phenomenon point strongly to a statistical picture of the fragmentation process: necks nucleate independently at different locations at a critical strain level given by the Considère criterion and continue to grow under continued expansion of the ring. Statistical variability in the local material/geometrical properties of the specimen results in a distribution of the location at which such necks nucleate. As these necks grow, final fracture occurs, once again independently at the different necks, but this time, the release of stress unloads certain segments in the neighborhood. This brings about a length scale that depends on the range of failure strains, the strain rate imposed on the specimen and the speed of the release wave. Using the Mott approximation, we find that the maximum released length should be  $l_{\max} \propto \sqrt{2\sigma_0 \Delta\epsilon / \rho \dot{\epsilon}^2}$ , where  $\Delta\epsilon = \epsilon_f^{\max} - \epsilon_f^{\min}$  is the range of failure strains in the material. The maximum fragment size should then be about  $2l_{\max}$ . If we take  $\sigma_0 = 150$  MPa,  $\rho = 2700$  kg/m<sup>3</sup>, and  $\Delta\epsilon \sim 0.1$ , then we get  $2l_{\max} = 40$  mm for  $\dot{\epsilon} = 5 \times 10^3$  s<sup>-1</sup> and  $2l_{\max} = 20$  mm for  $\dot{\epsilon} = 10^4$  s<sup>-1</sup>; these compare quite well with the observed fragmentation size discussed above.

#### 4.5. Ductility and Strain to Fracture

As we pointed out in the introductory discussion, observations reported in the literature are based on assembly of recovered fragments and indicate that the total strain in the dynamically expanded ring is about 40%, while in contrast, quasi-statically the material strains only to about 25% until a single neck forms at a point of stress concentration. Such observations have been used to suggest that the ductility of a material increases with the strain rate (Altynova et al., 1993). While this statement has been repeated by numerous investigators, there is nothing in the deformation kinetics of the materials that can support such a dependence on strain rate. Our experimental observations show clearly that necking in the dynamically expanding ring occurs nearly simultaneously; so whence the increase in ductility? We now address this issue from the experimental measurements.

Since high speed images were obtained at 11  $\mu$ s time intervals, we identified the strain at appearance of necks through a bounding process; the strain at the last frame where uniform deformation is visible and the first frame where the neck is clearly visible can taken as the lower bound,  $\epsilon_N^{LB}$ , and upper bound,  $\epsilon_N^{UB}$ , respectively for the onset of necking; the nucleation of the neck is certainly between these strain levels. However, the time resolution of the images does not allow us to bound the necking strain more closely; this is particularly true in the high expansion speed experiments where the strains develop much more rapidly. The final strain at failure  $\epsilon_f$  was determined by direct measurement of the fragment lengths on the high speed images.  $\epsilon_N^{LB}$ ,  $\epsilon_N^{UB}$  and  $\epsilon_f$  are plotted as a function of the ring expansion speed in Fig. 24, with a line between  $\epsilon_N^{LB}$  and  $\epsilon_N^{UB}$  indicating that necking occurred within this strain range. The quasi-static strain at which necking is observed in this material  $\epsilon_N^{qs}$  is also indicated in this figure by the horizontal line. It is clear that the bounds based on present resolution of the high speed camera do not allow us to determine the strain at onset of necking more tightly. In contrast,  $\epsilon_f$  appears to indicate a strong dependence on the strain rate and is significantly larger at higher strain rates; however, this correlation between  $\epsilon_f$  and the strain rate does not necessarily imply that the ductility of the material increases with strain rate. We note that the strain in the fragments is nonuniform (as a result of the large number of arrested necks) and therefore the average value of  $\epsilon_f$  is not likely to be a very useful measure of the strain in the ring. We need to examine this more closely at the deformation of the ring in order to understand the apparent increase in ductility observed in the

dynamic experiments. This is accomplished through post-mortem measurements on the fragments.

We look into the recovered fragments and attempt to construct the strain experienced by each fragment. A composite micrograph of fragment VII of Specimen *D* (see Fig. 10) is shown in Fig. 25; arrested necks are readily identified. Quantitative measurement of the residual strain variation along the length of the specimen can be obtained by threshold filtering this image and identifying the variation of the width of the specimen along the length of the fragment. The variation of the width,  $w(x)$ , along the length of the fragment is shown in Fig. 26 for four fragments from different specimens. A similar variation in the width was observed in all other fragments. Some important observations arise from this result:

- First, necks are easily identified as the regions with larger lateral contraction in the specimen. Three arrested necks are observed between the ends of the fragment, spaced nonuniformly along the fragment shown in Fig. 25. In fact, this method allowed us to identify arrested necks along the fragments that were not easily visible in the high speed photographs.
- Second, the neck occurs over a length of about one cross-sectional dimension (between 1 to 2 mm long) and appears to vary even within the same specimen.
- Third, given that the initial nominal width of the specimen was  $w_0 = 1$  mm, and assuming incompressibility of the material, the width measurement allows the determination of the local longitudinal stretch along the fragment. Clearly, a longitudinal stretch between 2 and 3 is observed at the center of the neck, without any indication of failure, for the fragment of specimen with 8 kV charging voltage; this stretch at neck decreases with expanding velocity such that it is only 1.5 for the specimen with a 5 kV charging voltage.
- Lastly, in the portions of the fragment that did not experience neck formation, the residual strain, denoted by  $\epsilon_u^R$  and obtained from the width measurements, is uniform at a level of about 0.21 to 0.24; the error in these measurements is estimated to be about 2.5%. This uniform strain level is indicated by the dotted line in Fig. 26, corresponding to  $\epsilon_u^R = 0.22$ . This strain level appears not to be influenced either by the location in the ring or the ring expansion rate. The values of  $\epsilon_u^R$  measured on rings expanding at different speeds is plotted in Fig. 27 and is roughly equal to  $\epsilon_N^{qs}$ . *Thus, the regions outside the neck zone never experienced a strain larger than the Considère strain!* Therefore, estimated average expansion of the ring beyond this strain level must be simply due to accumulation of strain within the necks.

The last observation suggests that the high value of  $\epsilon_f$  measured in the recovered fragments is really due to averaging the nonuniform strain variation over the nominal length of the fragment and that the high strains are really accumulated in the neck zones. The specimen width measurement shown in Fig. 26 can be used to construct an accurate estimate for the average strain in the fragment. Ignoring elastic deformations, and imposing incompressibility of plastic deformation, the axial stretch can be obtained in terms of the transverse stretch:

$$\lambda(x) = \frac{1}{\lambda_t^2} = \left( \frac{w_0}{w(x)} \right)^2 \quad (19)$$

In order to estimate the average strain in the fragment, we need the initial length that gave rise to this fragment; this is estimated easily by integrating the stretch:

$$l_0 = \int_0^{l_f} \frac{dx}{\lambda(x)} \quad (20)$$

where  $l_f$  is the final length of the fragment; the average strain in the fragment can then be calculated as  $\bar{\epsilon}_f = \ln(l_f/l_0)$ . For the fragment shown in Fig. 25,  $\epsilon_u^R = 0.24$ , while  $\bar{\epsilon}_f = 0.43$ , showing the influence of the large strains within the necks. The final average strain determined in a number of fragments at different expanding speeds is shown in Fig. 27; this average strain exhibits a significant increase with expanding speed and matches the strains estimated from length measurements on the high speed images. This demonstrates conclusively that the apparent increase in the final strain in the fragments is really due to the accumulation of large strains within the necks and that unnecked regions do not strain above the Consid re strain.

The differences between the quasi-static and dynamic responses can be understood in terms of the nature of the applied loading and the progression of the unloading resulting from the onset of necking. In the quasi-static test, when a neck forms at the point of the highest stress concentration or the most significant defect in the specimen, it effectively unloads *all* the remaining portions of the specimen and the rest of the specimen *never* experiences a strain beyond  $\epsilon_N^{qs}$ ; thus, the point in the specimen with the lowest necking strain or the location of the largest stress concentration determines this strain level. Furthermore, if the failure strain is defined as the strain over the gage length of the specimen, then,  $\epsilon_f \rightarrow \epsilon_N^{qs}$  for very long specimens. On the other hand, in the dynamic situation encountered in the expanding ring tests, necking is possible as long as  $\epsilon \geq \epsilon_N^{qs} \sim n$ ; these necks appear at random locations, dictated by local variations in the material and geometry. The nucleation of a neck at one location in the ring, unlike in the quasi-static case, sends a release wave of small amplitude and unloads only a small neighborhood in its vicinity; the extent of this unloaded zone depends on the strain rate since the speed of the release wave from necking is expected to be similar to the Mott release wave resulting from fracture. The strain in the unloaded zone will then not be able to increase above  $\epsilon_N^{qs}$  and further strain in the specimen is only through strains that develop within the neck zone; this is clearly observed in the fragments. Other necks are able to nucleate outside of the unloading zone from each neck since every point in the specimen is near the Consid re strain; this accounts for the multiple nucleation of necks and their statistical distribution.

## 5. Conclusion

We have examined the classical problem of fragmentation in ring specimens. Al 6061-O specimens were expanded at speeds in the range of 80 m/s to about 200 m/s; this corresponds to strain rates in the range of 4000 to 10000 per second. While expanding ring experiments of this kind have been performed previously, in the present experiments, in addition to the usual instrumentation for measuring the current flow in the system, we incorporated a high-magnification, high-speed camera to capture the sequence of events that precede fragmentation of the ring. These high speed images reveal that the picture of fragmentation presented in the early work of Mott is substantially accurate when augmented with the mechanics associated with necking localization. Additional insight into the onset and growth of necking in the specimen is obtained from these experiments. The results present a clear physical picture of ductile failure at high strain rates. The experiments were performed in Al 6061-O, but we expect the behavior of other ductile materials to be substantially similar as long as strain rate hardening effects are small. Specifically, we observe that

- Uniform strains of up to 25% can be generated in the ring specimen at strain rates of about  $10^4 \text{ s}^{-1}$ . In this regime, strain hardening plastic behavior is shown to be sufficient to capture the deformation of the expanding ring. Surprisingly, strain rate effects do not appear to be important for the aluminum alloy Al 6061-O.
- Necks nucleate along the ring at numerous locations. The number of necks nucleated increases rapidly with expanding speed of the ring and the necks appear to be distributed over a wide range of lengths, dictated by statistical material property and geometric variations.
- The strain at nucleation of the necks is shown to be governed by the Considère criterion and exhibits no strain-rate dependence for this material.
- The distance between necks appears to follow a Weibull distribution. Such a distribution suggests formulating the problem through statistical variation in mechanical properties with accounting for the unloading waves that propagate from the localization event.
- Fragments appear quite independently of each other, once again with their nucleation governed by statistical variations in the failure strain. Unloading or release waves in the sense of Mott are shown to diffuse from the fractures and prevent subsequent fractures.
- Details of the sequence and location of the appearance of necks and fragments have been captured in these experiments and they enable formulation of appropriate models to capture the physics of fragmentation.
- The apparent increase in ductility that is often quoted in the literature is shown to be based on an erroneous interpretation of the experiments. A large number of necks that are nucleated in the high strain rate experiments; such nucleation is facilitated by the slow propagation of unloading waves from individual necks and fractures. The measured "average" strain to failure is really made up of unnecked regions with a strain level equal to the Considère strain and necked regions with much larger strains.

Three important final comments are in order. First, in the numerical simulations of the expanding ring experiment, such as those of Pandolfi et al (1999), Guduru and Freund (2002) and Zhou et al. (2006), the essential ingredients of the necking and fragmentation process have been included: exhaustion of strain hardening that results in necking localization and inertia that limits the extent of unloading resulting from the localization. Therefore, their simulations should capture both the onset of multiple necking (either at an imposed wavelength of the perturbation or at random from numerical round-off effects) and the inertially limited unloading of the neighborhood of each neck. In fact, both Guduru and Freund (2002) and Zhou et al. (2006) observe that necks nucleate nearly simultaneously and that further straining occurs within the necked region. Second, the observation that  $\epsilon_u^R \sim \epsilon_N^{qs}$  suggests that the limit to uniform deformations is not significantly different from the quasi-static limits; this contradicts the observations of Altynova et al (1996) and needs to be examined further for different materials and different geometrical constraints. Lastly, stretches in the range of 2 to 3 are observed within the necks, indicating that the true strain in the material at failure,  $\epsilon_f^{TRUE}$ , is possibly higher. Therefore, with suitable geometrical constraints and/or limits to the straining within the necks, it may be possible to generate larger strains in high speed forming operations.

#### Acknowledgement

This work was performed under a program entitled "Experimental Characterization of Nonlinear Viscoelastic and Adhesive Properties of Elastomers" sponsored by the Office of Naval Research (ONR Grant Number N00014-05-1-0400, Program Manager: Dr. Roshdy Barsoum); this support is gratefully acknowledged. It is a pleasure to acknowledge discussions with Professor Ken Liechti during the course of this investigation.

## References

- AIP, American Institute of Physics Handbook, 3<sup>rd</sup> ed., 1972, New York
- M. Altynova, X. Hu and G.S. Daehn, 1996, Increased ductility in high velocity electromagnetic ring expansion, *Metallurgical and Materials Transactions A*, **27A**, 1837-1844.
- R. Becker, 2002, Ring fragmentation predictions using the Gurson model with material stability conditions as failure criteria, *International Journal of Solids and Structures*, **39**, 3555-3580.
- C. Frassengeas and A. Molinari, 1994, Fragmentation of rapidly stretching sheets, *European Journal of Mechanics – A-Solid*, **13**, 251-268.
- I.M. Fyfe and A.M. Rajendran, 1980, Dynamic pre-strain and inertia effects on the fracture of metals, *Journal of the Mechanics and Physics of Solids*, **28**, 17-26.
- W.H. Gourdin, 1989, Analysis and assessment of electromagnetic ring expansion as a high-strain-rate test, *Journal of Applied Physics*, **65**, 411-422.
- D.E. Grady and D.A. Benson, 1983, Fragmentation of metal rings by electromagnetic loading, *Experimental Mechanics*, **12**, 393-400.
- D.E. Grady and M. Olsen, 2003, A statistics and energy based theory of dynamic fragmentation, *International Journal of Impact Engineering*, **29**, 293-306.
- P.R. Gududru and L.B. Freund, 2002, The dynamics of multiple neck formation and fragmentation in high rate extension of ductile materials, *International Journal of Solids and Structures*, **39**, 5615-5632.
- J.B. Han and V. Tvergaard, 1995, Effect of inertia on the necking behavior of ring specimens under rapid radial expansion, *European Journal of Mechanics – A-Solid*, **14**, 287-307.
- B. Hopkinson, 1910, **Collected Scientific Papers**, Cambridge University Press.
- J. Hopkinson, 1872, **Collected Scientific Papers**, Cambridge University Press.
- J.D. Jackson, 1975, **Classical Electrodynamics**, 2<sup>nd</sup> ed., Wiley Eastern, 1978.
- M.E. Kipp and D.E. Grady, 1985, Dynamic fracture growth and interaction in one dimension, *Journal of the Mechanics and Physics of Solids*, **33**, 399-415.
- S. Mercier and A. Molinari, 2003, Predictions of bifurcation and instabilities during dynamic extension, *International Journal of Solids and Structures*, **40**, 1995-2016.
- N.F. Mott, 1947, Fragmentation of shell cases, *Proceedings of the Royal Society of London, Series A*, **189**, 300-308.
- F.I. Niordson, 1965, A unit for testing materials at high strain rates, *Experimental Mechanics*, **5**, 23-32.

- A. Pandolfi, P. Krysl and M. Ortiz, 1999, Finite element simulation of ring expansion and fragmentation: The capturing of length and time scales through cohesive models of fracture, *International Journal of Fracture*, **95**, 279-297.
- S. Satapathy and D. Landen, 2006, Expanding ring experiments to measure high-temperature adiabatic properties, *International Journal of Impact Engineering*, in press.
- V. Shenoy and L.B. Freund, 1999, Necking bifurcations during high strain rate extension, *Journal of the Mechanics and Physics of Solids*, **47**, 2209-2233.
- N. Triantafyllidis and J. R. Waldenmyer, Onset of necking in electromagnetically formed rings, *Journal of the Mechanics and Physics of Solids*, **52**, 2127-2148.
- T. von Karman, and P. Duwez, 1950, The propagation of plastic deformation in solids, *Journal of Applied Physics*, **21**, 987-994.
- F. Zhou, J.F. Molinari and K.R. Ramesh, 2006, An elasto-visco-plastic analysis of ductile expanding ring, *International Journal of Impact Engineering*, in press.



Table 1. High speed expanding ring test on Al 60610-O.

Charging Voltage (kV)	Test No.	Velocity (m/s)	Necking Number	Fracture Number	$\epsilon_N^{LR}$	$\epsilon_N^{UB}$	$\epsilon_u^R$	$\epsilon_f$	$\bar{\epsilon}_f$
5	A	80	20	4	0.11100	0.28880	0.2413	0.2829	0.2351
	A-1	79	15	3	0.18500	0.27670	0.2268	0.2555	0.3259
	A-2	80	17	3	0.099400	0.25140	0.2156	0.2429	0.3005
6	B	120	20	8	0.14790	0.34660	0.1831	0.3424	0.3360
	B-1	121	21	6	0.17480	0.36910	0.2156	0.3184	0.3456
7	C	154	35	10	0.053400	0.34470	0.2045	0.3641	0.3869
	C-1	143	23	10	0.18980	0.36110	0.2380	0.3609	0.4123
8	D	200	30	14	0.12710	0.45660	0.2414	0.4281	0.4330
	D-1	192	27	11	0.21460	0.42550	0.2156	0.3931	0.4312

Table 2. Quantitative data of test A: expanding velocity: ~80 m/s

Neck	Location		$T_n$ ( $\mu$ s)	$T_b$ ( $\mu$ s)	Fracture Order
	$\theta$ (deg)	$r$			
1	36.216	$[r_5, r_6]$	< 63.72	—	—
2	43.889	$[r_5, r_6]$	< 63.72	—	—
3	98.631	$[r_4, r_5]$	< 52.72	57.07	1
4	112.07	$[r_4, r_5]$	< 52.72	—	—
5	125	$[r_4, r_5]$	< 52.72	—	—
6	142.23	$[r_5, r_6]$	< 63.72	—	—
7	161.49	$[r_5, r_6]$	< 63.72	—	—
8	177.6	$[r_4, r_5]$	< 52.72	—	—
9	197.53	$[r_5, r_6]$	< 63.72	—	—
10	214.07	$[r_5, r_6]$	< 63.72	75.82	3
11	231.07	$[r_5, r_6]$	< 63.72	—	—
12	239.14	$[r_5, r_6]$	< 63.72	—	—
13	252.16	$[r_5, r_6]$	< 63.72	—	—
14	260.89	$[r_5, r_6]$	< 63.72	—	—
15	278.57	$[r_5, r_6]$	< 63.72	—	—
16	299.18	$[r_5, r_6]$	< 63.72	—	—
17	314.7	$[r_5, r_6]$	< 63.72	—	—
18	331.37	$[r_5, r_6]$	< 63.72	—	—
19	338.12	$[r_5, r_6]$	< 63.72	—	—
20	355.51	$[r_5, r_6]$	< 63.72	74.53	2

$r_4 = 18.65$  mm,  $r_5 = 19.69$  mm,  $r_6 = 20.44$  mm.

Table 3. Quantitative data of test B: expanding velocity: ~120 m/s

Neck	Location		$T_n$ ( $\mu s$ )	$T_b$ ( $\mu s$ )	Fracture Order
	$\theta$ (deg)	$r$			
1	4.07	$[r_4, r_5]$	< 47.4	51.26	2
2	21.047	$[r_4, r_5]$	< 47.4	—	—
3	49.951	$[r_4, r_5]$	< 47.4	—	—
4	69.026	$[r_4, r_5]$	< 47.4	58.12	4
5	79.144	$[r_3, r_4]$	< 36.4	—	—
6	85.113	$[r_3, r_4]$	< 36.4	—	—
7	109.87	$[r_4, r_5]$	< 47.4	—	—
8	128.97	$[r_4, r_5]$	< 47.4	47.99	1
9	152.01	$[r_4, r_5]$	< 47.4	—	—
10	156.33	$[r_5, r_6]$	< 58.4	—	—
11	171.23	$[r_6, r_7]$	< 69.4	—	—
12	189.45	$[r_5, r_6]$	< 58.4	72.14	8
13	206.98	$[r_5, r_6]$	< 58.4	—	—
14	212.75	$[r_5, r_6]$	< 58.4	61.68	5
15	224.58	$[r_6, r_7]$	< 79.4	—	—
16	230.85	$[r_5, r_6]$	< 58.4	70.03	7
17	255.77	$[r_5, r_6]$	< 58.4	64.07	6
18	276.42	$[r_4, r_5]$	< 47.4	—	—
19	286.40	$[r_4, r_5]$	< 47.4	—	—
20	298.92	$[r_4, r_5]$	< 47.4	53.90	3
21	334.78	$[r_4, r_5]$	< 47.4	—	—

$r_3 = 17.97$  mm,  $r_4 = 19.33$  mm,  $r_5 = 20.64$  mm,  $r_6 = 21.92$  mm.

Table 4. Quantitative data of test C: expanding velocity: ~150 m/s

Neck	Location		$T_n$ ( $\mu$ s)	$T_b$ ( $\mu$ s)	Fracture Order
	$\theta$ (deg)	$r$			
1	8.8690	$[r_3, r_4]$	< 36.0	—	—
2	17.041	$[r_4, r_5]$	< 47.0	—	—
3	30.426	$[r_4, r_5]$	< 47.0	—	—
4	45.816	$[r_4, r_5]$	< 47.0	—	—
5	50.463	$[r_4, r_5]$	< 47.0	51.67	5
6	63.020	$[r_4, r_5]$	< 47.0	—	—
7	70.059	$[r_4, r_5]$	< 47.0	—	—
8	79.427	$[r_4, r_5]$	< 47.0	—	—
9	86.430	$[r_4, r_5]$	< 47.0	58.0	9
10	96.755	$[r_4, r_5]$	< 47.0	—	—
11	115.38	$[r_4, r_5]$	< 47.0	52.0	6
12	131.66	$[r_4, r_5]$	< 47.0	55.43	8
13	145.88	$[r_4, r_5]$	< 47.0	—	—
14	150.05	$[r_4, r_5]$	< 47.0	—	—
15	153.20	$[r_4, r_5]$	< 47.0	—	—
16	158.29	$[r_4, r_5]$	< 47.0	—	—
17	162.78	$[r_4, r_5]$	< 47.0	—	—
18	172.51	$[r_4, r_5]$	< 47.0	—	—
19	177.40	$[r_4, r_5]$	< 47.0	52.5	7
20	204.92	$[r_3, r_4]$	< 36.0	45.5	4
21	217.30	$[r_3, r_4]$	< 36.0	—	—
22	233.94	$[r_4, r_5]$	< 47.0	—	—
23	239.59	$[r_4, r_5]$	< 47.0	—	—
24	244.53	$[r_4, r_5]$	< 47.0	—	—
25	248.77	$[r_4, r_5]$	< 47.0	—	—
26	267.71	$[r_3, r_4]$	< 36.0	41.47	2
27	277.29	$[r_3, r_4]$	< 36.0	38.7	1
28	305.81	$[r_4, r_5]$	< 47.0	—	—
29	308.72	$[r_4, r_5]$	< 47.0	—	—
30	328.00	$[r_4, r_5]$	< 47.0	58.0	10
31	338.32	$[r_4, r_5]$	< 47.0	—	—
32	344.10	$[r_4, r_5]$	< 47.0	—	—
33	350.52	$[r_3, r_4]$	< 36.0	—	—
34	357.89	$[r_3, r_4]$	< 36.0	45.0	3

$r_3 = 18.74$  mm,  $r_4 = 20.51$  mm,  $r_5 = 22.24$  mm.

Table 5. Quantitative data of test D: expanding velocity: ~200 m/s

Neck	Location		$T_n$ ( $\mu$ s)	$T_f$ ( $\mu$ s)	Fracture Order
	$\theta$ (deg)	$r$			
2	1.73	$[r_3, r_4]$	< 36.32	—	—
2	19.97	$[r_3, r_4]$	< 36.32	45.84	4
3	39.62	$[r_3, r_4]$	< 36.32	46.19	5
4	47.82	$[r_3, r_4]$	< 36.32	—	—
5	55.23	$[r_3, r_4]$	< 36.32	—	—
6	62.05	$[r_3, r_4]$	< 36.32	—	—
7	69.73	$[r_3, r_4]$	< 36.32	40.55	1
8	87.55	$[r_3, r_4]$	< 36.32	—	—
9	90.25	$[r_3, r_4]$	< 36.32	—	—
10	94.29	$[r_3, r_4]$	< 36.32	—	—
11	97.73	$[r_3, r_4]$	< 36.32	—	—
12	108.10	$[r_3, r_4]$	< 36.32	41.29	2
13	119.74	$[r_3, r_4]$	< 36.32	—	—
14	125.43	$[r_3, r_4]$	< 36.32	—	—
15	131.05	$[r_3, r_4]$	< 36.32	—	—
16	137.39	$[r_4, r_5]$	< 47.32	—	—
17	148.77	$[r_3, r_4]$	< 36.32	49.39	7
18	156.25	$[r_3, r_4]$	< 36.32	—	—
19	164.98	$[r_4, r_5]$	< 58.32	—	—
20	176.10	$[r_4, r_5]$	< 47.32	54.24	11
21	179.43	$[r_4, r_5]$	< 47.32	—	—
22	185.53	$[r_4, r_5]$	< 47.32	—	—
23	191.10	$[r_4, r_5]$	< 47.32	—	—
24	202.60	$[r_4, r_5]$	< 47.32	56.84	12
25	217.47	$[r_3, r_4]$	< 36.32	50.28	9
26	221.50	$[r_4, r_5]$	< 47.32	—	—
27	225.42	$[r_4, r_5]$	< 47.32	—	—
28	237.91	$[r_4, r_5]$	< 47.32	46.54	6
29	249.08	$[r_5, r_6]$	< 58.32	—	—
30	260.87	$[r_4, r_5]$	< 47.32	51.31	10
31	267.89	$[r_4, r_5]$	< 47.32	—	—
32	277.62	$[r_4, r_5]$	< 47.32	50.18	8
33	290.75	$[r_4, r_5]$	< 47.32	63.42	14

34	303.88	$[r_4, r_5]$	$< 47.32$	—	—
35	316.77	$[r_4, r_5]$	$< 47.32$	41.85	3
36	334.55	$[r_4, r_5]$	$< 47.32$	—	—
37	340.47	$[r_4, r_5]$	$< 47.32$	—	—
38	353.24	$[r_5, r_6]$	$< 58.32$	58.19	13

---

$r_3 = 19.21$  mm,  $r_4 = 21.50$  mm,  $r_5 = 23.72$  mm,  $r_6 = 25.84$  mm.

Table 6. Variable definitions and material properties

Variable	Initial value or definition	Description
$C$	25 $\mu\text{F}$	Solenoid circuit capacitance
$N$	6	Winding loop number
$s$	2.54 mm	Winding spacing
$d_w$	1.36 mm	Wire width
$r_s$	12.70 mm	Mean winding radius
$r_0$	15.5 mm	Mean initial ring radius
$A$	0.5 mm <sup>2</sup>	Ring cross-section area
$R_2$	$2\pi r\Omega/A$	Specimen resistance
$\Omega$	$\Omega = \Omega_0 [1 + a_r (T - 25)]$	Temperature-dependant specimen resistivity
$\Omega_0$	$3.66 \times 10^{-8} \text{ } \Omega\text{-m}$	Resistivity at 25 °C
$a_r$	0.0039	Temperature coefficient of resistivity
$C_p$	$C_p = c_0 + c_1 T + c_2 T^2 + c_3 T^3$	Temperature-dependant specific heat
$c_0$	875.6 J/kg·K	Temperature coefficient of specific heat
$c_1$	0.919	
$c_2$	$-2.76 \times 10^{-3}$	
$c_3$	$-4.41 \times 10^{-6}$	
$\rho$	$-2.7 \times 10^3 \text{ kg/m}^3$	Specimen density
$E$	70 GPa	Young's modulus
$\nu$	0.33	Poisson's ratio
$\varepsilon$	$\ln(r/r_0)$	Total strain
$\sigma$	$\sigma = \sigma_y (1 + \beta \varepsilon_p)^n [1 - (T - T_0)/(T_m - T_0)]^m$	Flow stress
$\sigma_y$	25 MPa	Initial yield strength
$\varepsilon_p$	$\varepsilon_p = \varepsilon - \sigma/E$	Plastic strain
$\beta$	14165	Strain hardening coefficient
$n$	0.22	Strain hardening exponent
$m$	1.34	Temperature softening coefficient
$T$	25 °C	Specimen temperature
$T_0$	21.11 °C	Room temperature
$T_m$	652.22 °C	Specimen melting temperature

## Figures

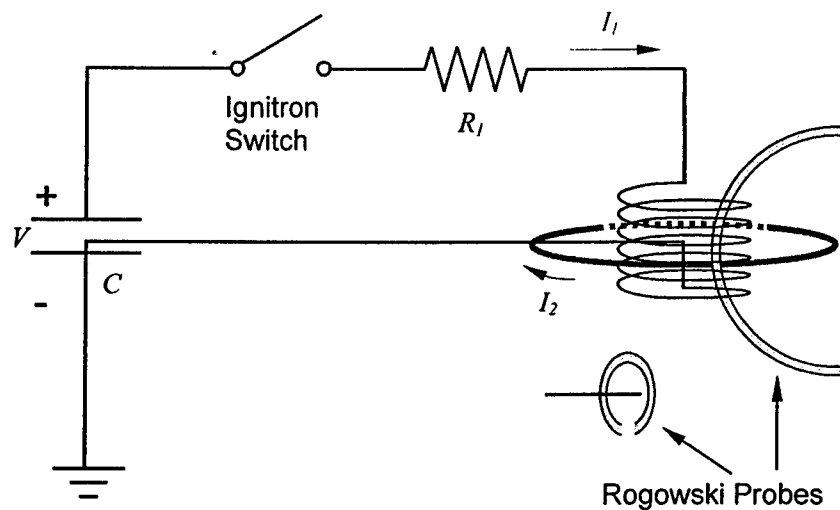


Figure A-1. Schematic diagram of the expanding ring experiment.

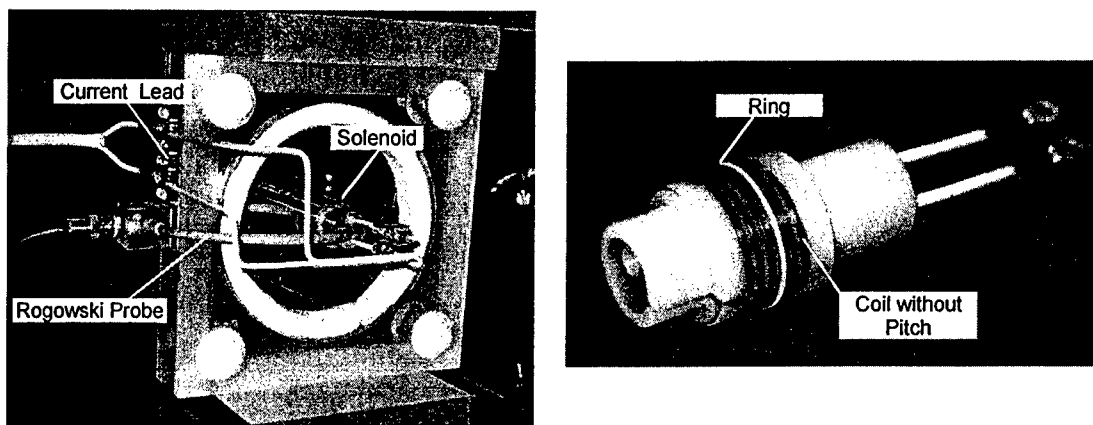


Figure A-2. Photograph of the experimental arrangement of the expanding ring test. The left image shown the complete test cell; the right image shows a detailed view of the solenoid and the specimen



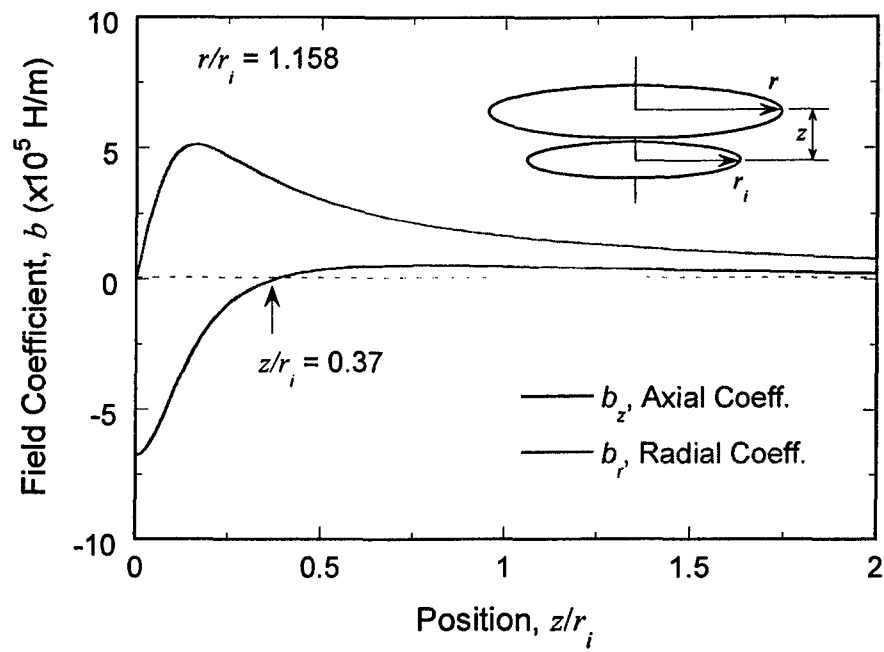
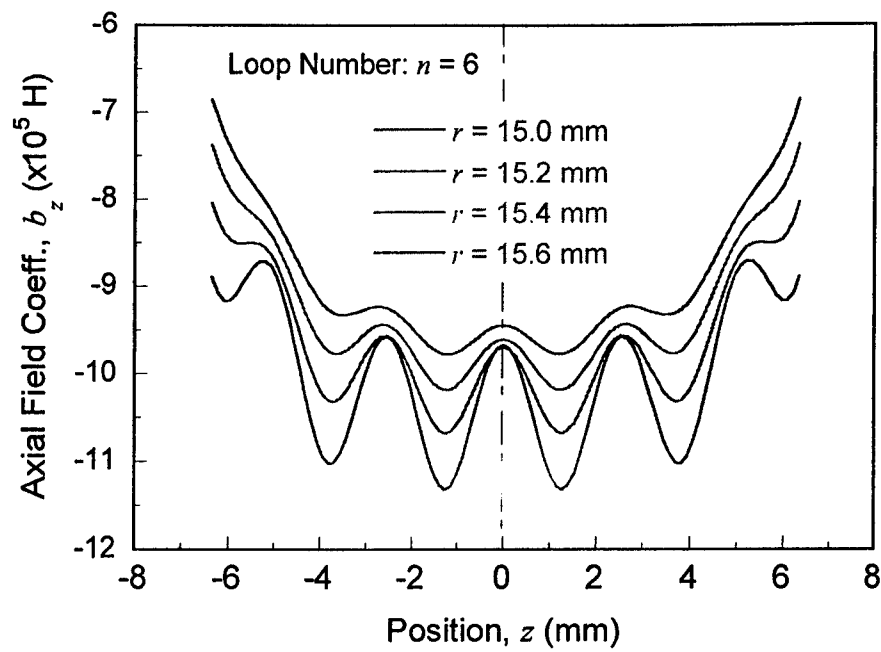
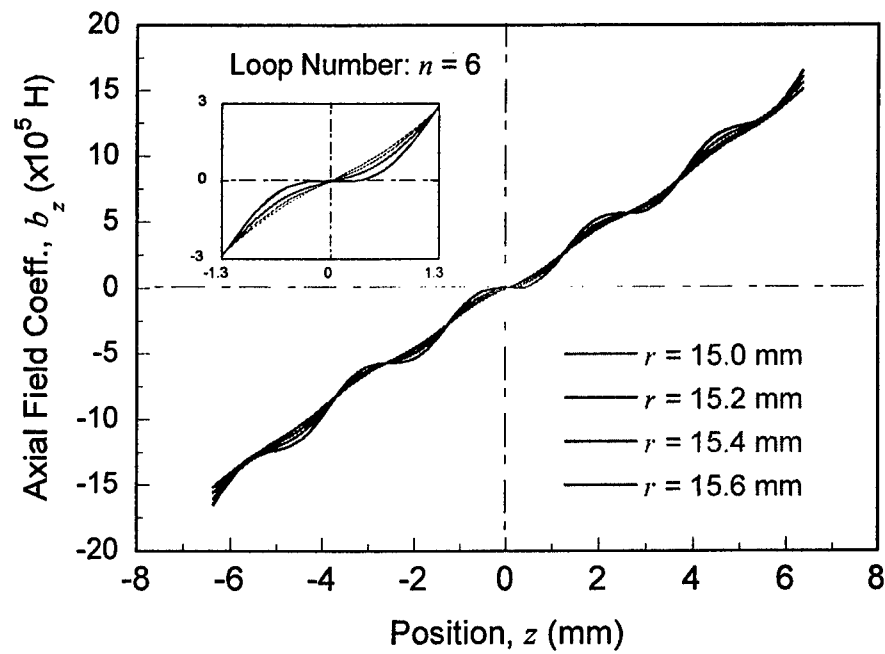


Figure A-3. Magnetic field coefficients  $b^z$  and  $b^r$  of one single coil  $i$  as a function of spatial distance  $z$ .



(a)



(b)

Figure A-4. Magnetic field coefficients (a)  $b^z$  and (b)  $b^r$  of a 6-turn solenoid as a function of spatial distance  $z$ . The inset in (b) shows the detail near  $z = 0$

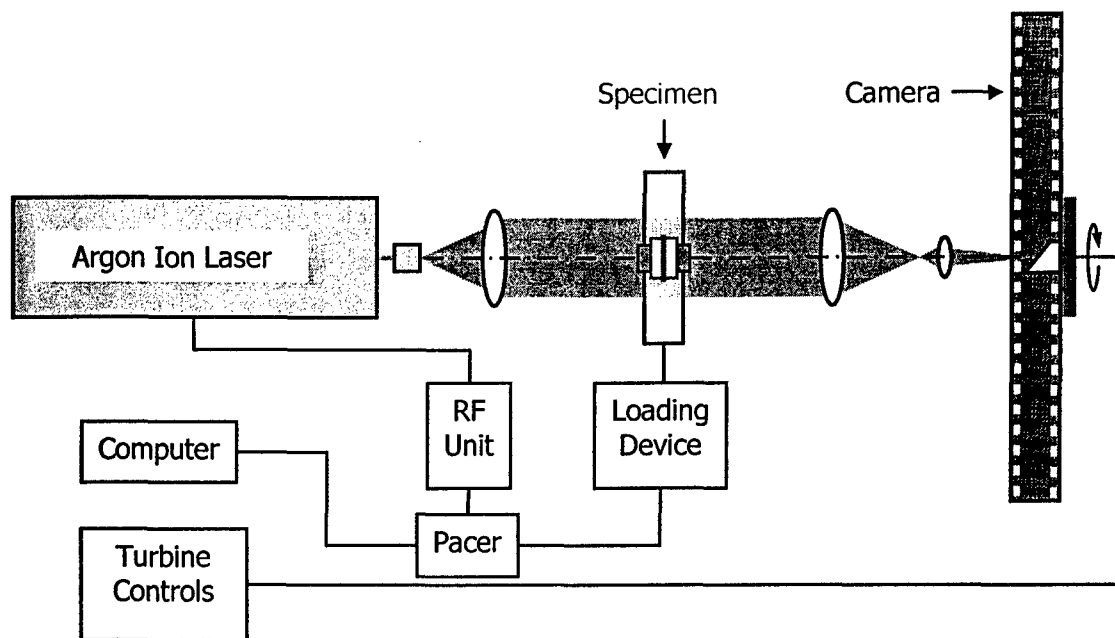


Figure A-5. Schematic diagram of the high speed camera and the optical arrangement.

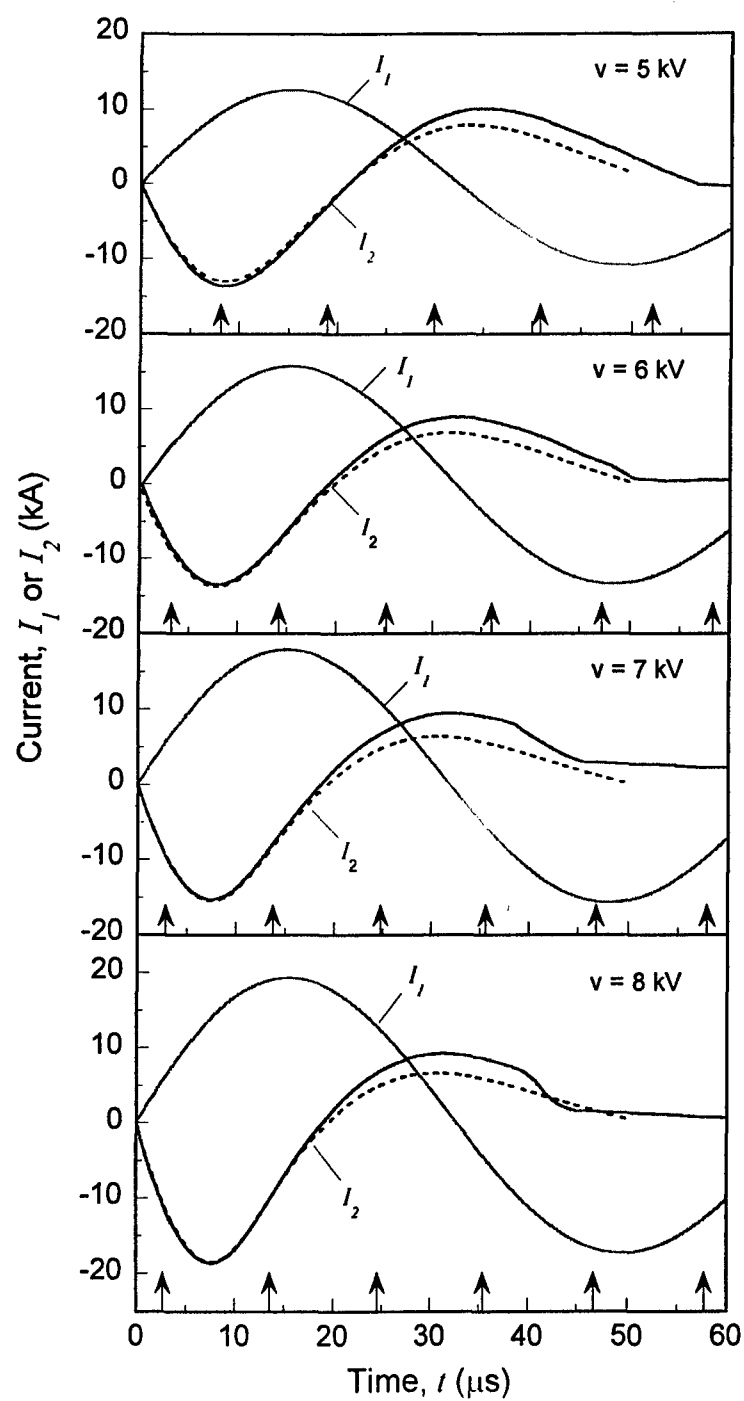


Figure A-6. Measured variation of the current in the primary circuit,  $I_1$ , and the expanding ring,  $I_2$ , for Specimens A, B, C and D. The arrows mark times at which high speed images were obtained.

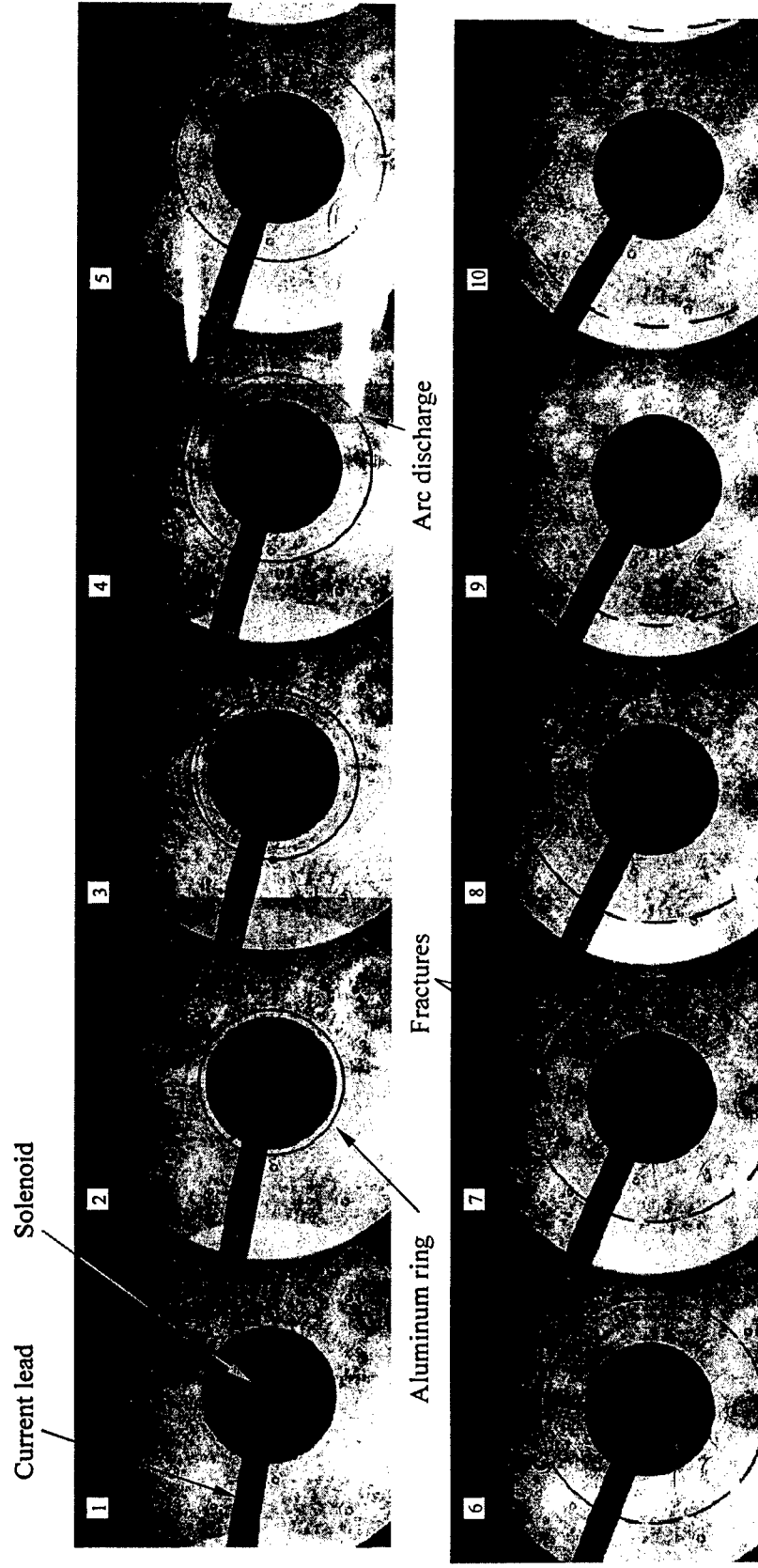


Figure A-7. The sequence of images showing the expansion of an Al 6061-O ring specimen (Specimen C).

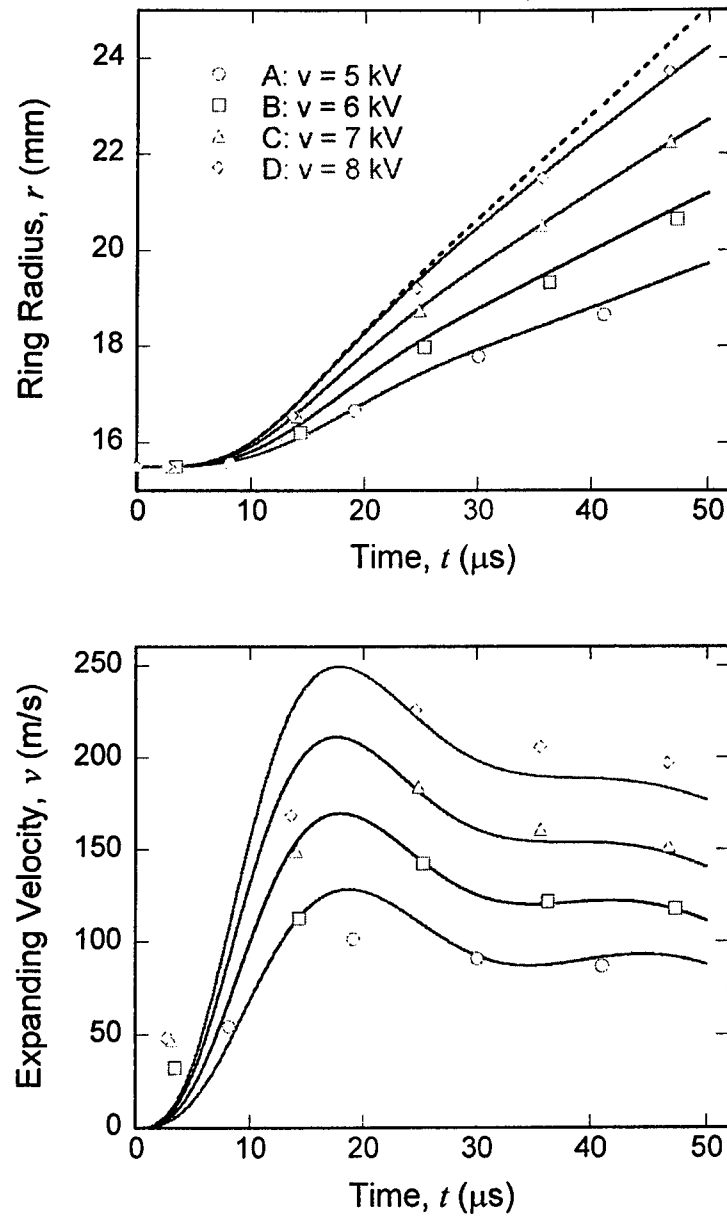


Figure A-8. Time history of (a) the ring radius and (b) the expansion velocity of Al 6061-O Specimens *A*, *B*, *C* and *D*. The dashed curve in (a) is that considers thermal softening effect governed by Eq. (14).

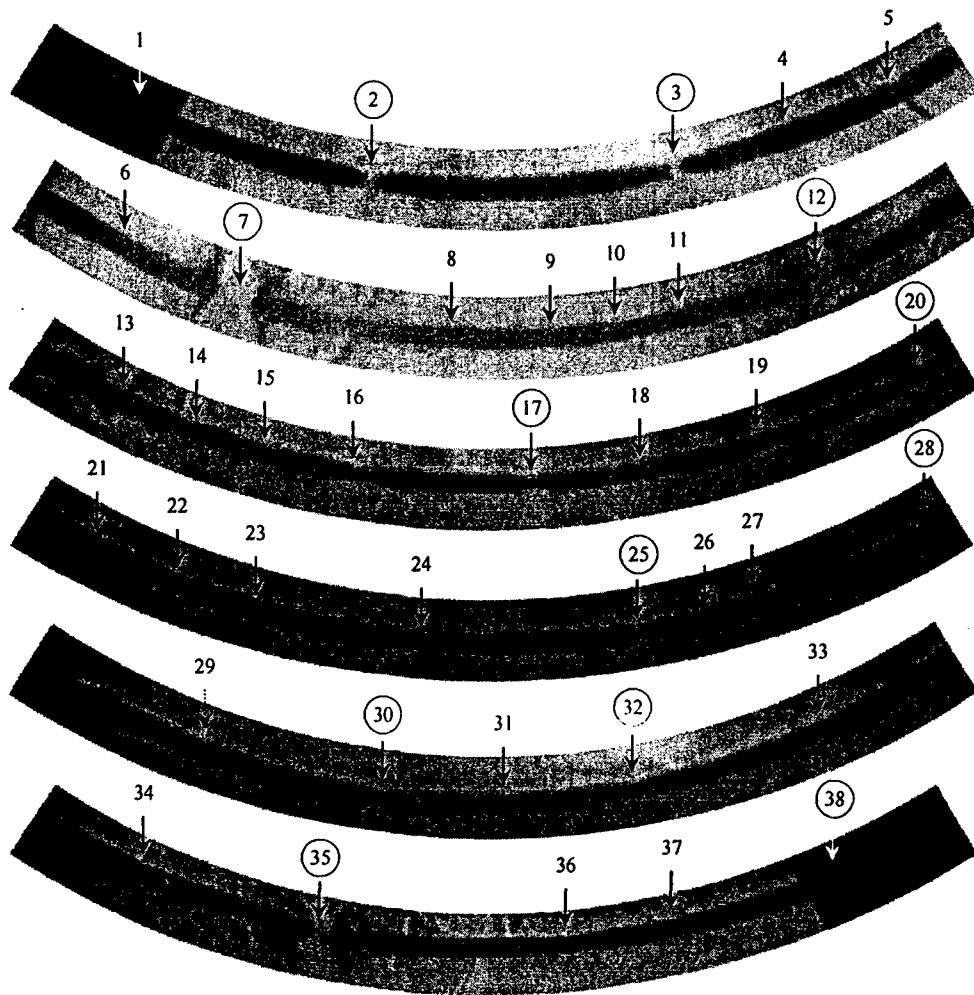


Figure A-9. High magnification images taken from the 5<sup>th</sup> image of Specimen C shown in Fig. 7. The positions of all necks are identified. Necks that grew into fractures are identified with a circle around the label. Neck 21 is developed later and marked with a dot arrow. The position of neck 30 is determined by the post-mortem fragments.

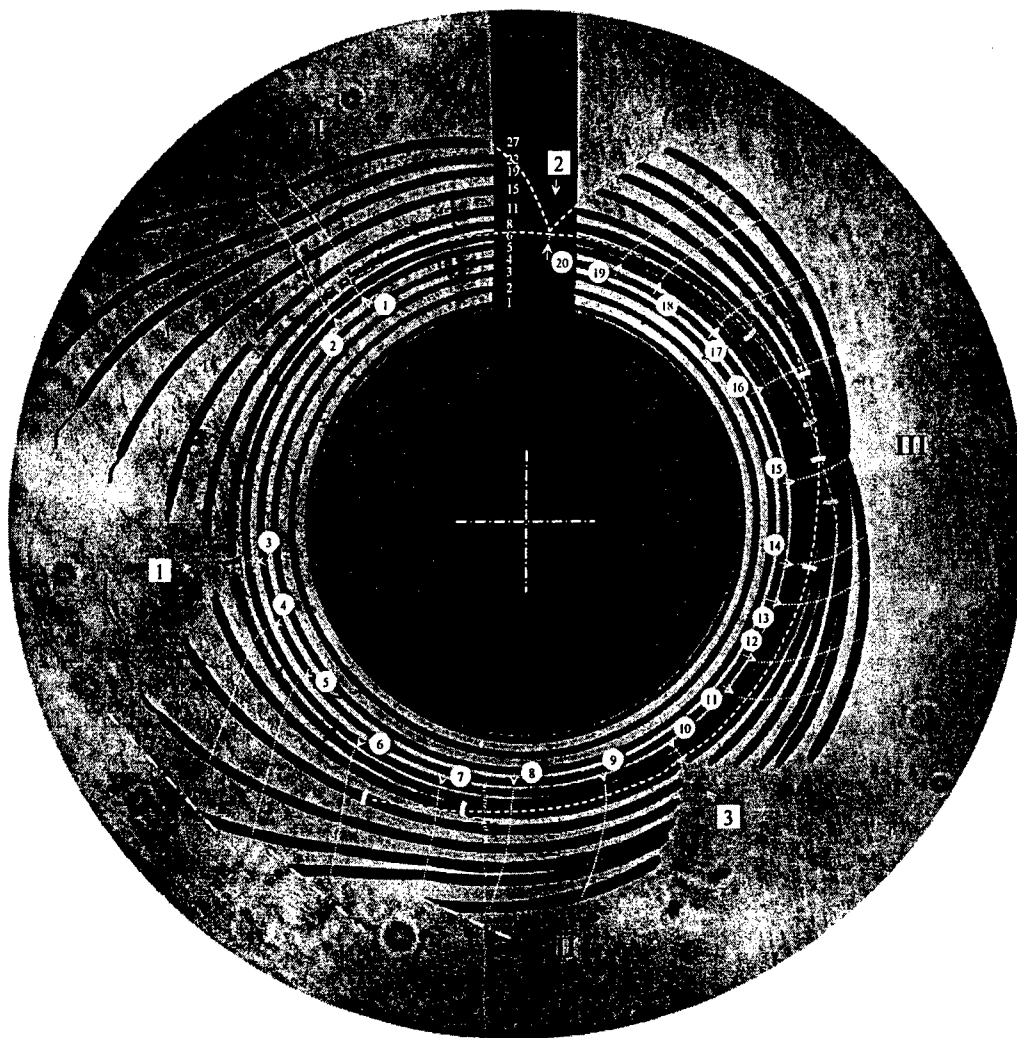


Figure A-10. Composite image for an Al 6061-O ring expanding test (Specimen A). The frame numbers are identified along the current lead on the top. The necks are identified at the location of their appearance by the numbers inside circles, numbering them counterclockwise. The trace of each neck is shown by the dot-lines following the neck appearance. The fracture locations are identified by the numbers inside squares, numbering them in the time sequence of their appearance. The arrivals of the Mott release wave are marked in these images with the red, green, and yellow lines for fractures 1, 2 and 3 respectively, with trace of the wave front marked by colored dash-lines. The dash-dot lines showing along some fragments indicate the cutoff of the figure, not the real geometry of the fragments.



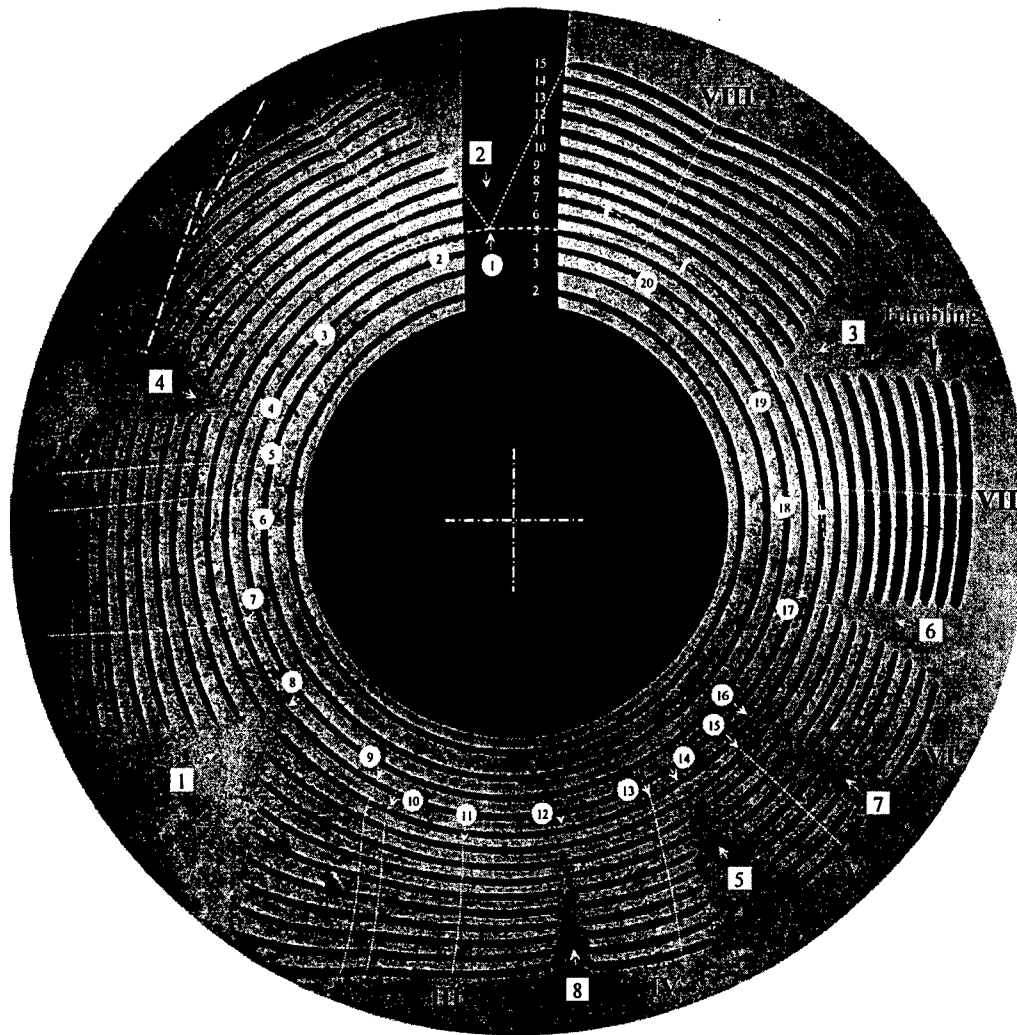


Figure A-11. Composite image for an Al 6061-O ring expanding test (Specimen *B*). The frame numbers are identified along the current lead on the top. The necks are identified at the location of their appearance by the numbers inside circles, numbering them counterclockwise. The fracture locations are identified by the numbers inside squares, numbering them in the time sequence of their appearance. The arrivals of the Mott release wave are marked in these images with the red, green, and yellow lines for fractures 1, 2 and 3 respectively, with trace of the wave front marked by colored dash-lines. The dash-dot lines showing along some fragments indicate the cutoff of the figure, not the real geometry of the fragments.

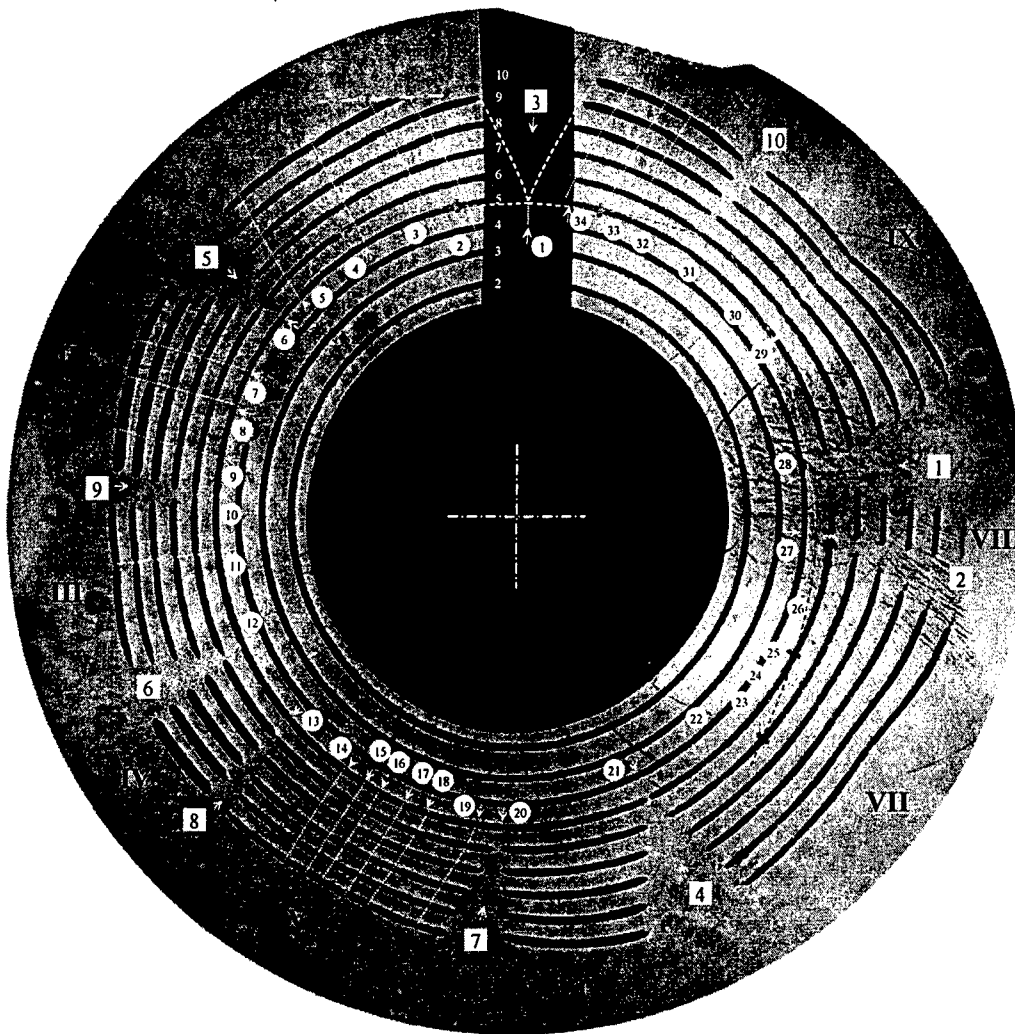


Figure A-12. Composite image for an Al 6061-O ring expanding test (Specimen C). The frame numbers are identified along the current lead on the top. The necks are identified at the location of their appearance by the numbers inside circles, numbering them counterclockwise. The fracture locations are identified by the numbers inside squares, numbering them in the time sequence of their appearance. The arrivals of the Mott release wave are marked in these images with the red, green, and yellow lines for fractures 1, 2 and 3 respectively, with trace of the wave front marked by colored dash-lines. The dash-dot lines showing along some fragments indicate the cutoff of the figure, not the real geometry of the fragments.

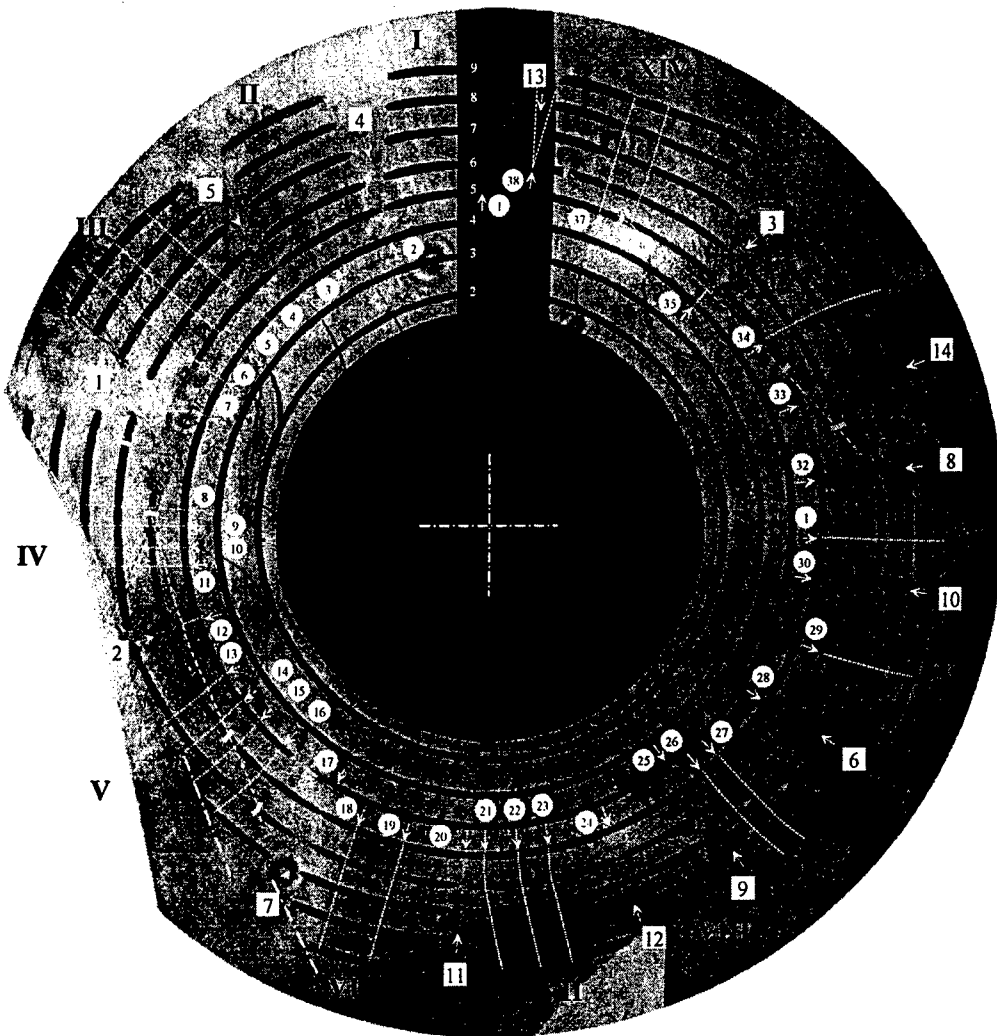


Figure A-13. Composite image for an Al 6061-O ring expanding test (Specimen *D*). The frame numbers are identified along the current lead on the top. The necks are identified at the location of their appearance by the numbers inside circles, numbering them counterclockwise. The fracture locations are identified by the numbers inside squares, numbering them in the time sequence of their appearance. The arrivals of the Mott release wave are marked in these images with the red, green, and yellow lines for fractures 1, 2 and 3 respectively, with trace of the wave front marked by colored dash-lines. The dash-dot lines showing along some fragments indicate the cutoff of the figure, not the real geometry of the fragments.

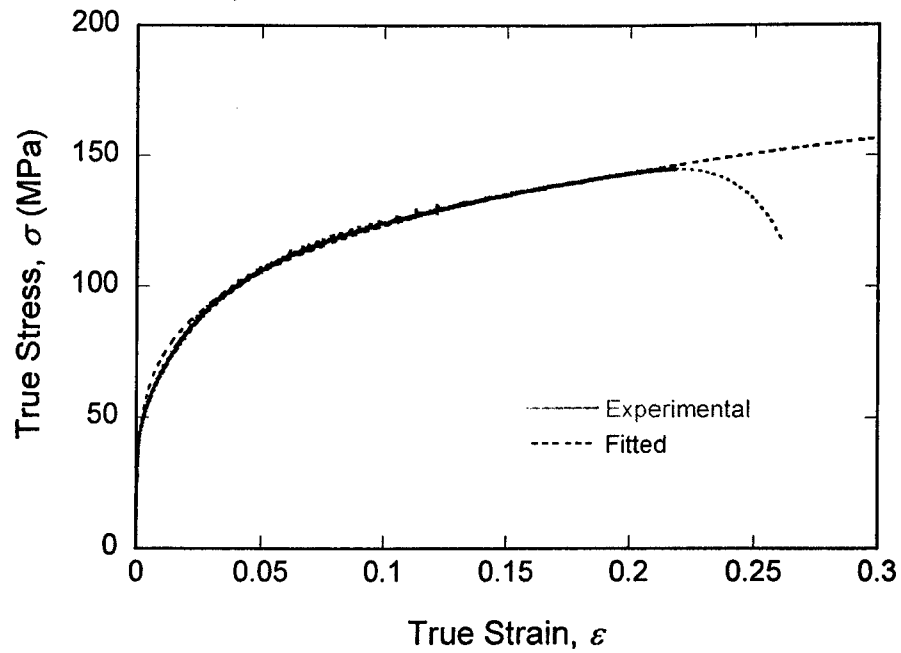


Figure A-14. Quasi-static stress-strain curve for Al 6061-O. The dashed line is fitted by the modified power law equation (13).

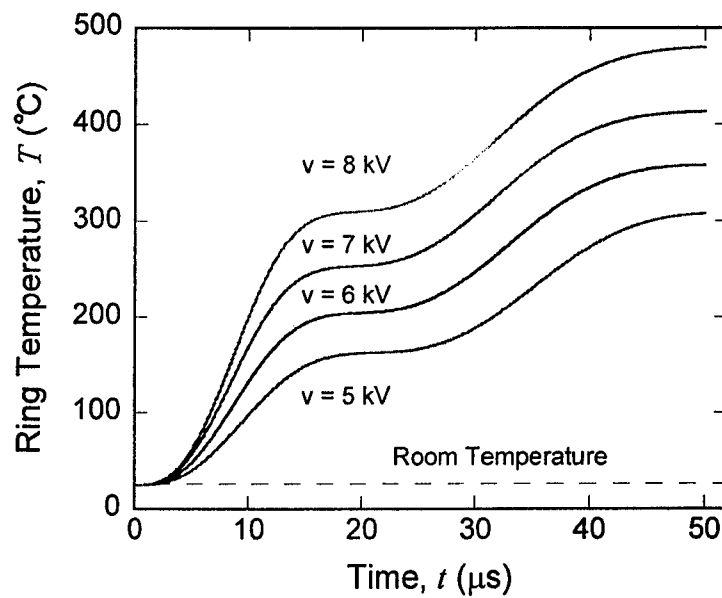


Figure A-15. Temperature estimate for the expanding ring Specimens A-D.

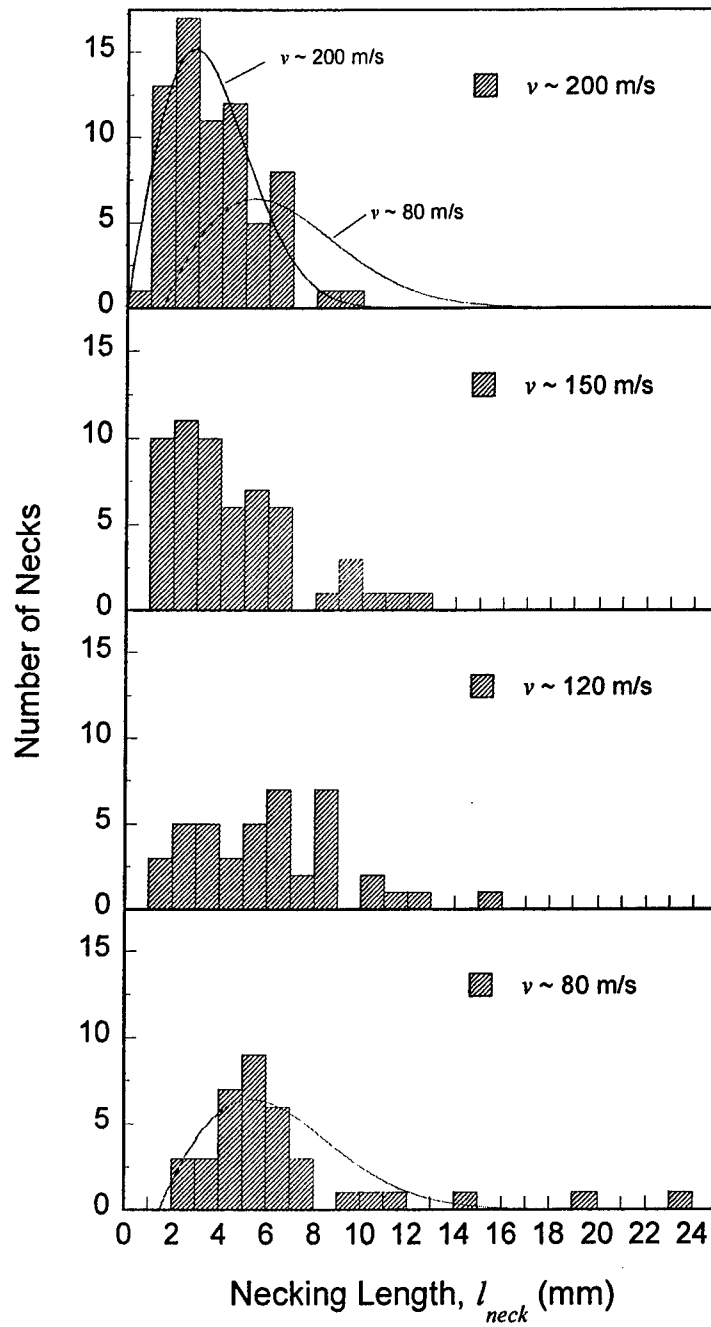


Figure A-16. Distribution in necking length  $l_{neck}$ . The fitting parameters for  $v \sim 80$  m/s are  $l_0 = 1.5$  mm,  $\kappa = 1.9$ , and  $\lambda = 5.75$ ; the fitting parameters for  $v \sim 200$  m/s are  $l_0 = 0$ ,  $\kappa = 2.02$ , and  $\lambda = 3.95$ .

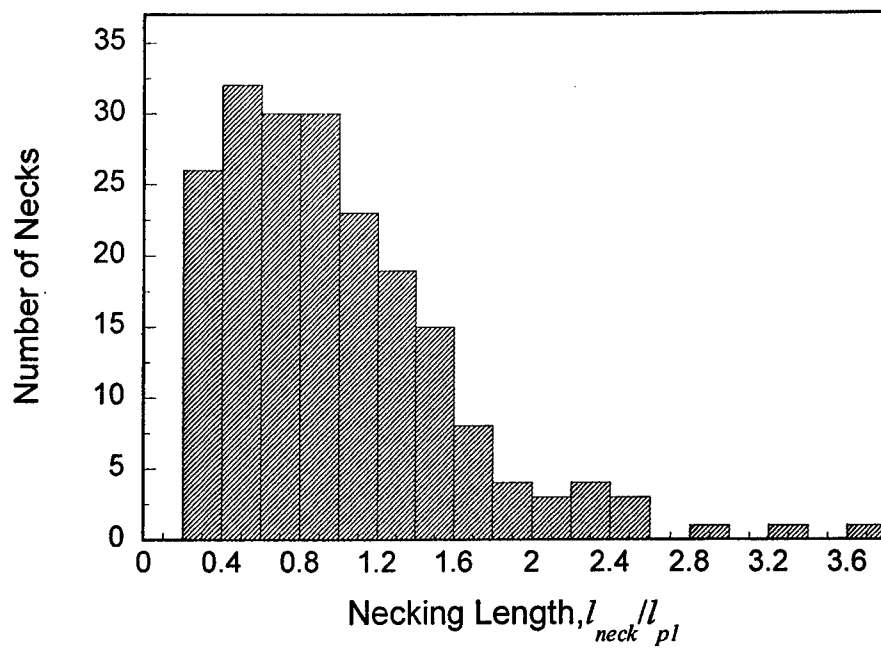


Figure A-17. Distribution in normalized necking length  $l_{neck}/l_{pl}$ .

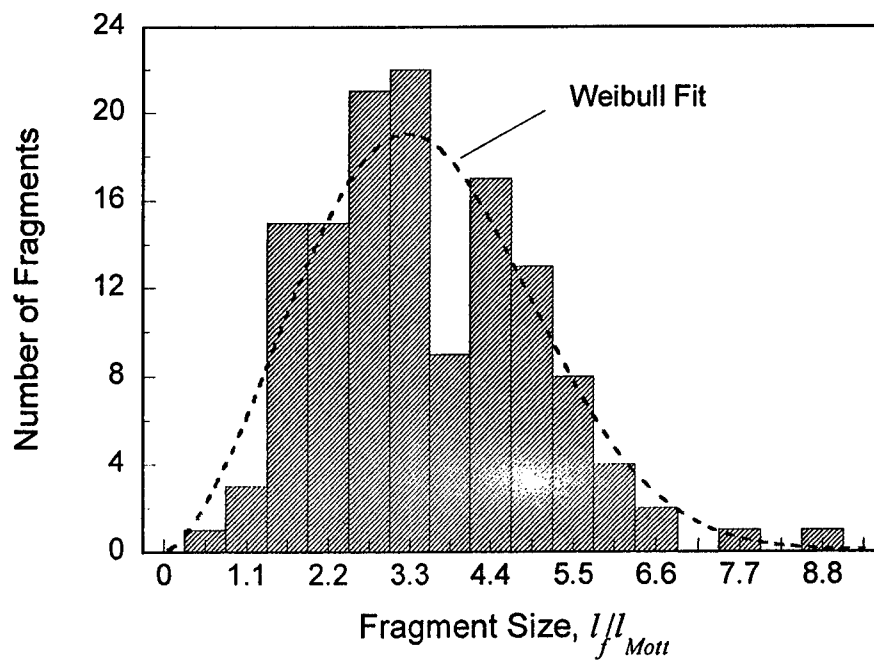


Figure A-18. Distribution in normalized fragment size  $l_f/l_{Mott}$ .

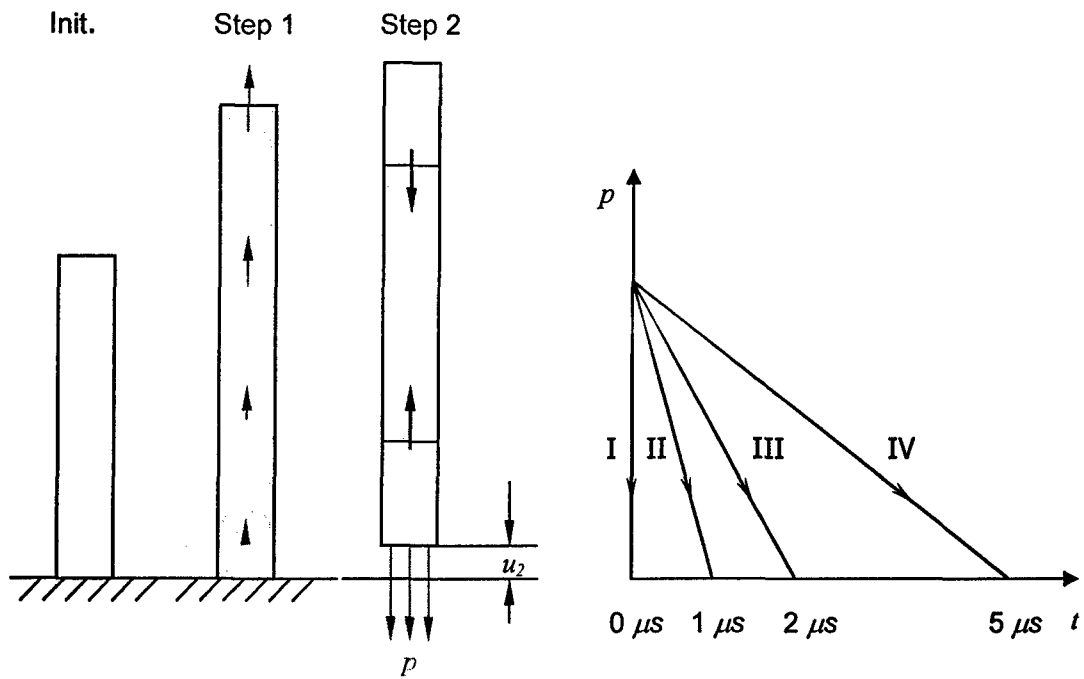


Figure A-19. Schematic diagram of the model used for simulating Mott wave propagation.

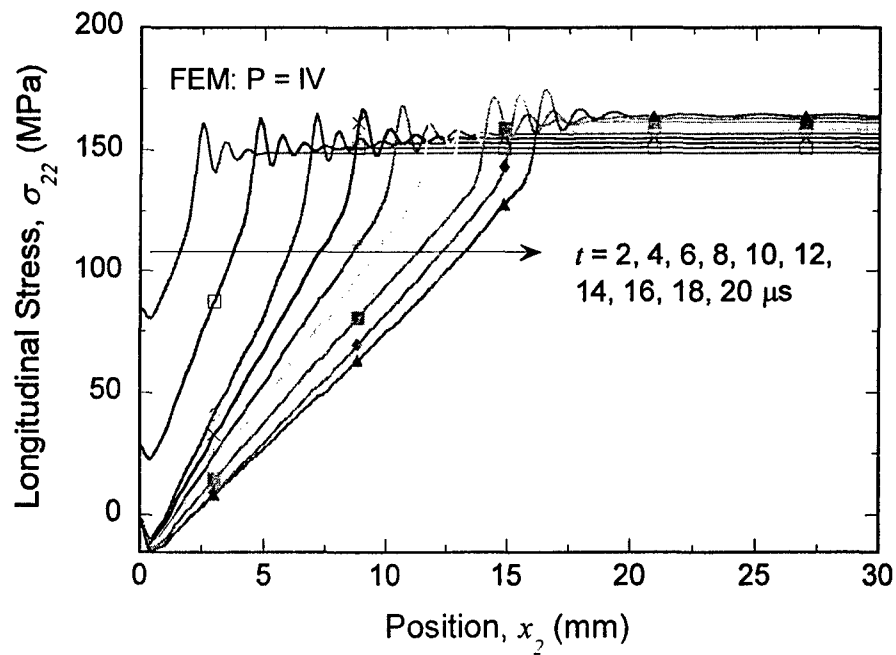


Figure A-20. Time evolution of the normal stress component  $\sigma_{22}$  for release profile IV.

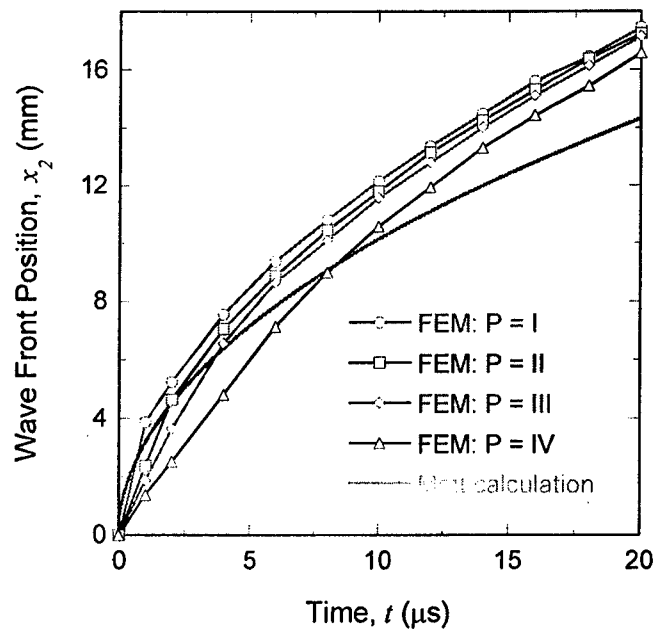


Figure A-21. Time history of the plastic wave front position on rod axis for the different release profiles. A Mott wave trace is plotted for comparison by assuming perfect plasticity with  $\sigma_y = 150$  MPa.

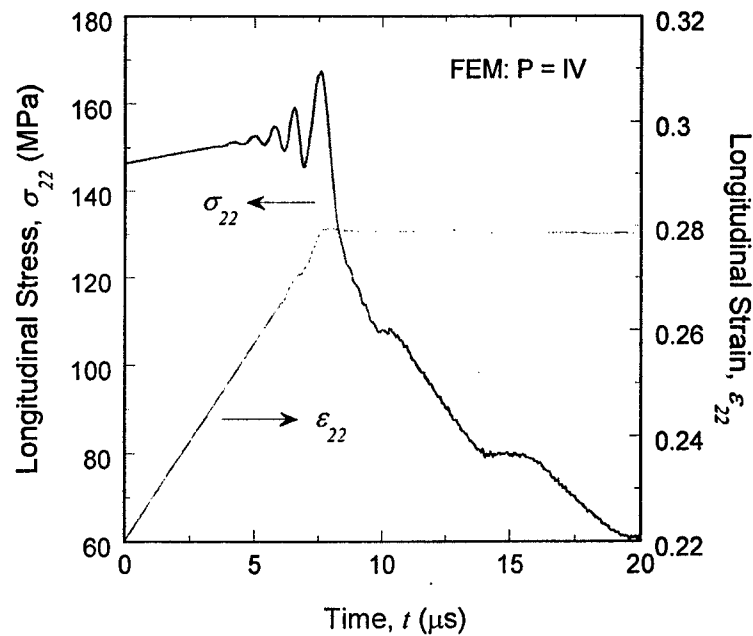


Figure A-22. Time variation of the stress and strain components  $\sigma_{22}$  and  $\epsilon_{22}$  at a point 10 mm from the release position.



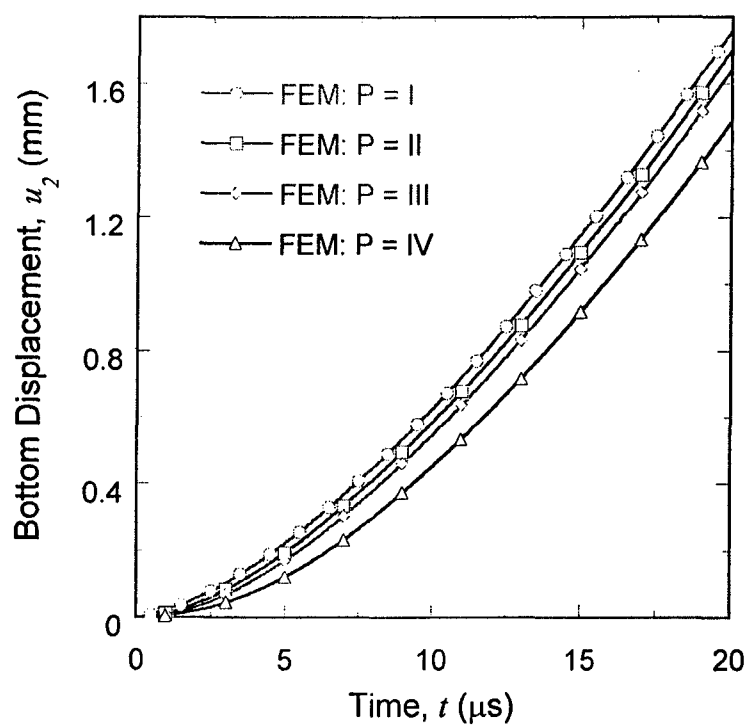


Figure A-23. The displacement of the released point  $u_2(x_2 = 0)$  as a function of time for the different release profiles.

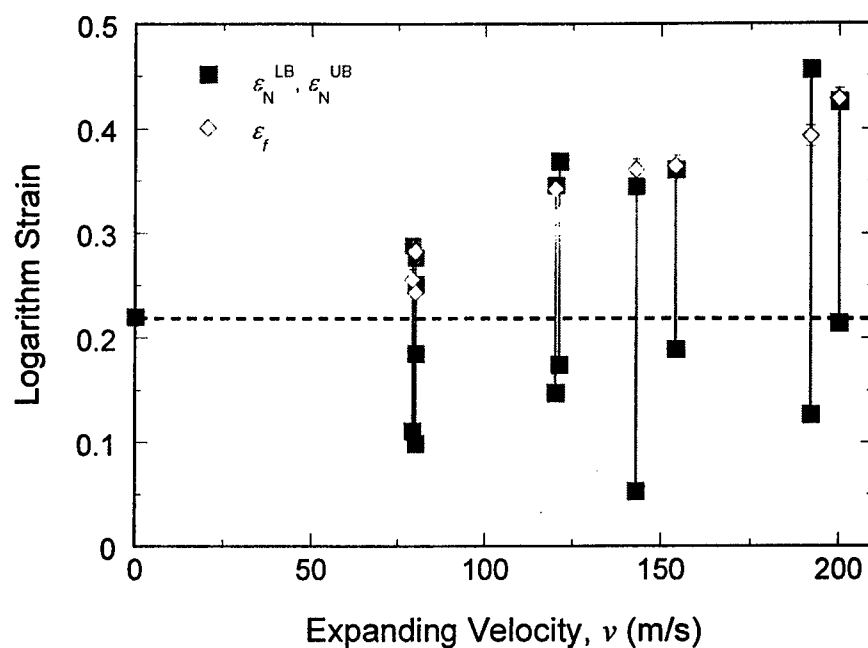


Figure A-24. The strain bounds of necking,  $\epsilon_N^{LB}$  and  $\epsilon_N^{UB}$ , and the final failure strain  $\epsilon_f$ , which are measured from the high speed images, indicate a strong dependence of the ring expanding velocity. The final failure strain tends to be consistent with the upper bound of necking and may not be a proper measure of the material ductility.

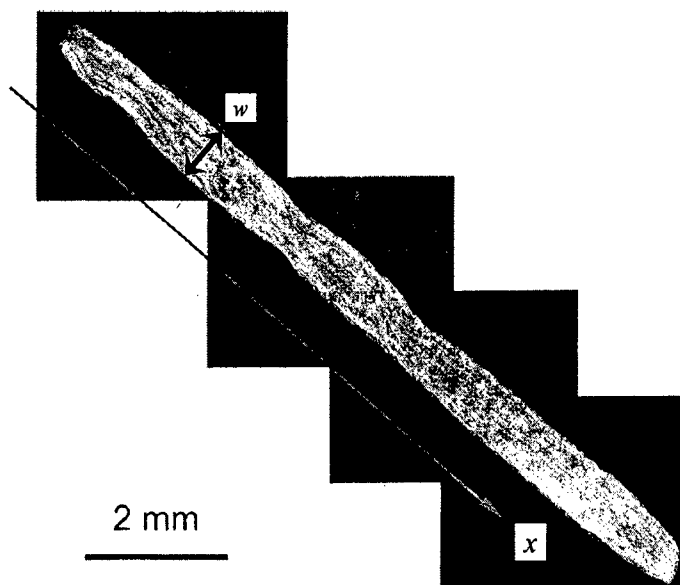


Figure A-25. The composite micrograph of the fragment VII of Specimen D.

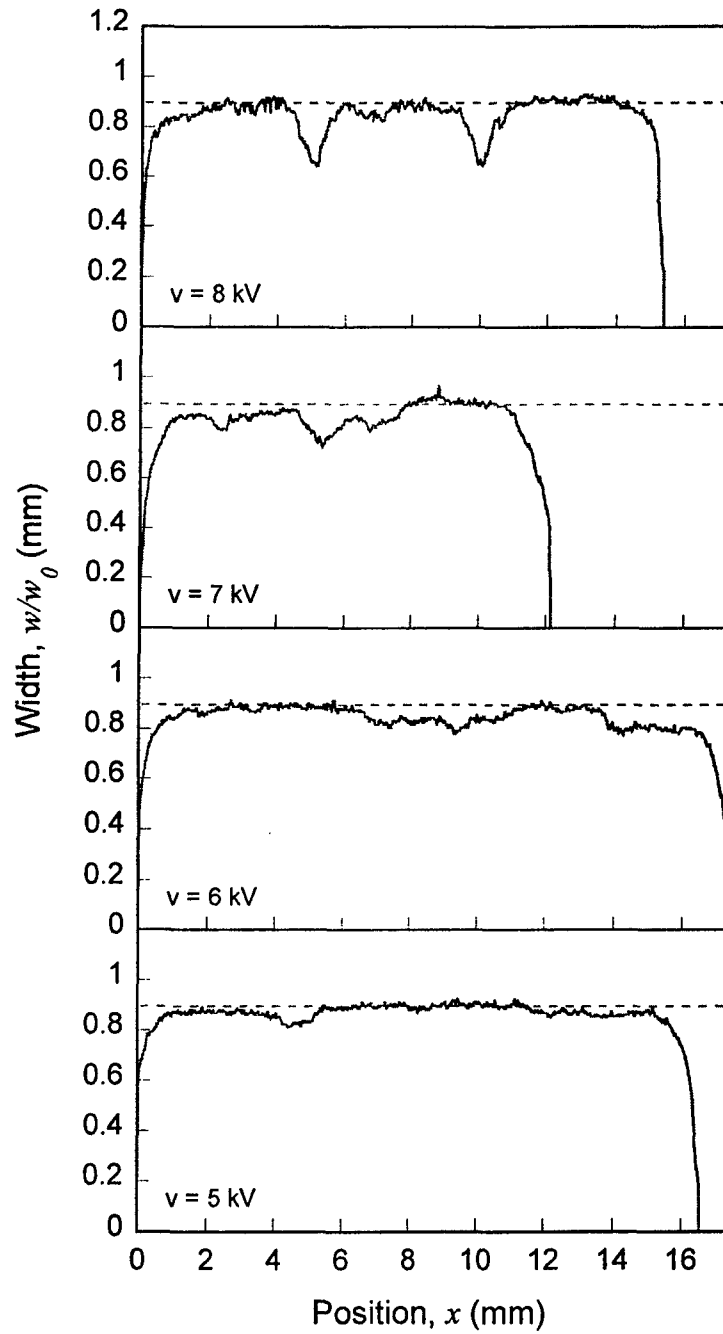


Figure A-26. Typical variation of the width of the fragment along its length. The width marked by the dashed lines corresponds to longitudinal strain of 0.22.

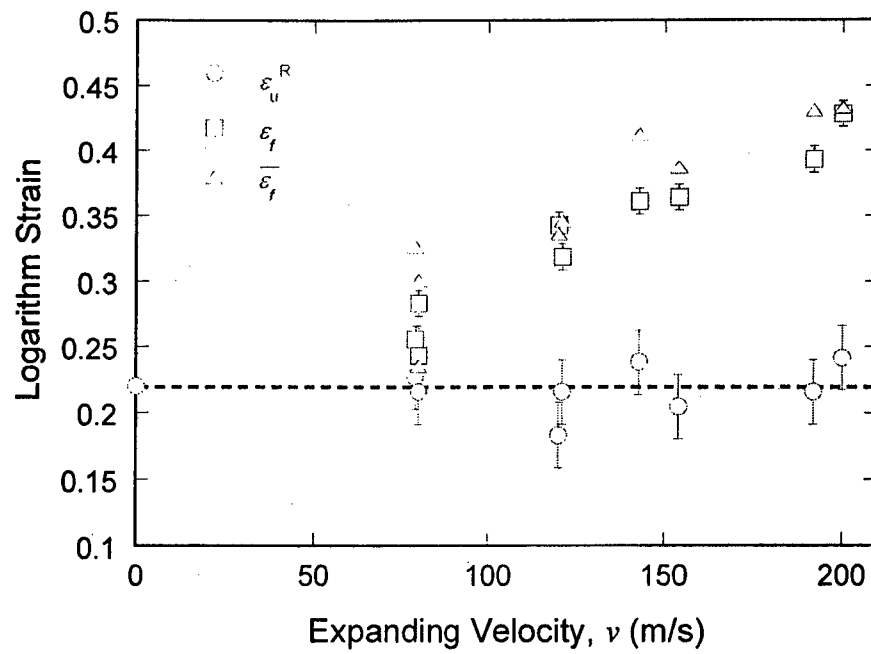


Figure A-27. Measured strains versus ring expansion velocity. The dashed line indicates the necking strain predicted by Considère criterion.

#### APPENDIX: Interpretation of Streak Image from Arc Discharge and Shock Waves

The high-speed image shown in Fig. 7 contains streak images from three arc discharges that resulted from the first three fractures in Specimen D. At the time of the fracture (about 55  $\mu$ s from the beginning of loading), a current of about 5 kA was still circulating in the ring specimen. Fracture interrupts the current flow, but since the separation between the ends of the fragments is initially small, an arc jumps across the now retracting ends of the fragments and sustains the current for a few more microseconds, until the ends move farther apart and arc gets quenched. This arc discharge corresponds to an intense explosion and the ionized plasma from the arc discharge expands spherically symmetrically and leaves a streak trace on the high speed image; an enlargement of this spark discharge streak is shown in Fig. A-1. The plasma expansion speed can be obtained from the streak image and interpreted using the scaling argument of Taylor (1950). Taylor showed that the radius of the blast wave from an intense explosion,  $r_b(t)$ , should be given by the following expression:

$$r_b(t) = \left( \frac{Et^2}{\rho_0} \right)^{1/5} \quad (\text{A-1})$$

where  $E$  is the energy in the explosion,  $\rho_0$  is the density of the air into which the explosion expands and  $t$  is the time; this above scaling was demonstrated by Taylor (1950) for atomic explosions. We show here that this expression can be fit nicely to the expansion of the plasma from the arc discharge (see Fig. A-1). In fact, we are able to extract the energy of the explosion from each spark discharge and show that this decreases with subsequent discharges.

The arc discharge also sets up an acoustic disturbance in the air that grows spherically at the speed of sound; this acoustic disturbance can be seen in the discrete frames obtained as a result of a pseudo-schlieren effect generated by the natural apertures in the high speed camera system. The propagation of the acoustic front can be seen in the enlarged frames 5 and 6 of Fig. 7 that are shown in Fig. A-2. From these images, it was found that this disturbance moves with the speed of sound  $\sim 340$  m/s. Some asymmetries are observed in the propagation of the acoustic disturbance since the ring continues to expand at a speed of about 200 m/s and provides additional constraints on the propagation of the acoustic signal.

Both the streak image of the plasma expansion and the propagation of the acoustic front can be used to identify the exact time of the arc discharge and hence to identify the time at which fracture of the expanding ring specimen occurred.

G.I. Taylor, 1950, The formation of a blast wave by very intense explosions. II. The atomic explosion of 1945, *Proceedings of the Royal Society of London*, **A201**, 175-186.



Figure A-1. Streak image of expansion of plasma generated in the arc discharge compared with the prediction based on Eq. (A-1).

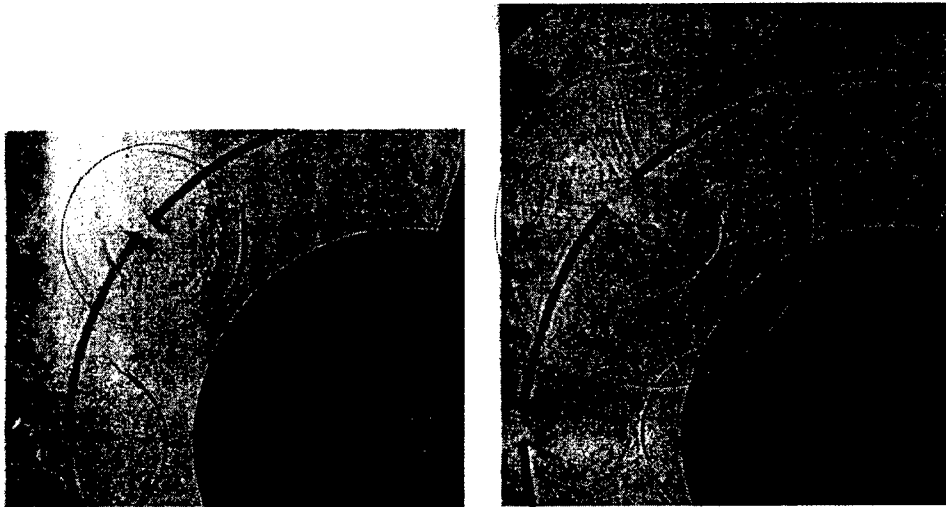


Figure A-2. High magnification sequence of the expansion of the shock wave in air generated by the arc discharge. The images are 11  $\mu$ s apart.